JUSTUS-LIEBIG-
UNIVERSITÄT
GIESSEN

Endocytotic Pathways in Human Adipose Stem Cells and Their Regulation by Intracellular Calcium Oscillations and the Neonatal Fc Receptor

Inaugural dissertation submitted to the Faculty of Medicine in partial fulfillment of the doctoral degree in human biology at Justus-Liebig-Universität Gießen

Submitted by

Morshed, Md Tanvir

from

Dhaka, Bangladesh

Gießen 2025

Examination Board

Supervisor:	**Prof. Dr. Heinrich Sauer**
Examiner:	**PD Dr. Anna Zakrzewicz**
Member:	**Prof. Dr. Timm Bauer**
Chair:	**Prof. Dr. Christos Samakovlis**

Date of the defense: **21 April 2026**

From the Institute of Physiology

Faculty of Medicine, Justus-Liebig-Universität Gieβen

First Supervisor and Committee Member:

Prof. Dr. Heinrich Sauer

And

From the Institute of Internal Medicine, Cardiology Division

Faculty of Medicine, Friedrich Schiller University Jena

Second Supervisor:

Prof. Dr. Maria Wartenberg

Dedication

I would like to dedicate this thesis to my parents Mrs. Sherin Akter & Mr. Md Anowar Hosain, my beloved wife Mrs Nasrin Akter and daughter Maabruka Morshed Aaima.

Md Tanvir Morshed

Gieβen, Germany

Contents

1. Introduction

1.1 Adipose Tissue-derived Stem Cells

Adipose tissue-derived stem cells (ADSCs) isolated by Zuk et al. (2001) from human lipoaspirate are a type of fibroblast-like mesenchymal stem cells (MSC) which have been proposed for diverse applications in stem cell therapeutics (Al-Ghadban & Bunnell, 2020). They offer an autologous source for regenerative medicine and tissue engineering because of their ability to differentiate into various cell types, including retinal cells (Huang et al., 2018; Qin et al., 2023), adipocytes, osteocytes (Chang et al., 2023; Shao et al., 2022), chondrocytes, myocytes (Yogi et al., 2021), and neurons (Masoumi et al., 2023). Moreover, the secretome of ADSCs comprising of extracellular vesicles (EVs) and nanovesicles (NVs) may be used in regenerative medicine (Trzyna & Banas-Zabczyk, 2021).

ADSC-derived exosomes increased the proliferation of retinal ganglion cells, whereas decreased apoptosis was observed through modulation of the expression of lactate

dehydrogenase, apoptosis-related proteins and neurotrophic factors (Zheng et al., 2023). Another study showed that ADSC-derived exosomes inhibit inflammation-induced ferroptosis and exacerbate the expression of NRF2 and nuclear translocation, thereby upregulating the expression of GPX4/SLC7A11 in human brain microvascular endothelial cells, which is clinically important in spinal cord injury (S. Wu et al., 2024). Hisanaga et al. (2023) presented promising immunosuppressive effects of ADSCs upon intravenous administration in xenotransplantation through decreasing immunoglobulin (IgM, IgG) deposition in tissue and increasing vascular endothelial growth factor (VEGF) and IL-10 in serum. ADSCs improved hepatocyte engraftment through the secretion of hepatocyte growth factor (HGF), VEGF, and IL-6 (Yamana et al., 2022). The function and longevity of hepatocyte organoids was enhanced by ADSCs (Ock et al., 2023). ADSCs provide promising therapeutic options for conditions such as proangiogenesis through macrophage polarization (Zhu et al., 2020), osteoarthritis (Bhattacharjee et al., 2022; Biazzo et al., 2020), cardiac ischemia (T. L. Lee et al., 2021; Lee et al., 2025; Liang et al., 2024), wound healing (Ren et al., 2024; Xu et al., 2024; Yang et al., 2024; Zhou et al., 2023; Zhou et al., 2022), sepsis

induced lung injury (He et al., 2024; Shen et al., 2023), hepatic injury (Abdelbaset-Ismail et al., 2022; Yu et al., 2023), inflamed human dermal fibroblasts, and skin inflammation (Yano et al., 2022), bone tissue engineering (Chang et al., 2023; Lau et al., 2024; Li et al., 2024), and sepsis-associated encephalopathy (Zhan et al., 2024).

Since ADSCs are belonging to the microenvironment of tumor cells they may play an important role in cancer biology and have been shown in recent years to exert pro- as well as anticarcinogenic properties. Although molecular karyotyping of ADSCs isolated from cancer patients and comparison with healthy individuals demonstrated no significant differences, genetic screening was recommended prior to every cell therapy (Garcia-Contreras et al., 2014). ADSCs induce breast cancer growth via BRCA1 in tumor cells (Plangger et al., 2021), and the proliferation of cancer cell was accelerated by resistin-treated ADSCs, which secrete C-X-C motif chemokine ligand 5 (CXCL5) and phosphorylated extracellular signal-regulated kinase (ERK) in the tumor microenvironment (Wang et al., 2022). A bioinformatic analysis of differentially expressed pseudogenes, messenger RNAs (mRNAs), long noncoding RNAs (lncRNAs), and micro RNAs (miRNAs) in ADSCs

and breast cancer cells across 33 distinct malignancies identified adenylate kinase 4 (AK4) as a critical marker for cancer prognosis and potential immunotherapy targets (Lu et al., 2024). ADSCs impede anoikis in colorectal cancer cells by secreting transforming growth factor-β1 (TGF-β1) which activates suppressor of mothers against decapentaplegic 3 (SMAD3), thereby facilitating angiopoietin-like 4 (ANGPTL4) expression (Zhu et al., 2024). miR-320a, abundant in metastatic cell-derived vesicles, induced cancer-associated fibroblast (CAF) activation of ADSCs via integrin subunit α7 to enhance ovarian cancer metastasis (Gong et al., 2024; Liu et al., 2024). ADSC transplantation reduced the apoptosis of ovarian granulosa cells and secretion of follicle-stimulating hormone, whereas they increased the number of total follicles, primordial follicles, primary follicles, mature follicles and secretion of the anti-mullerian hormone, estradiol in premature ovarian failure resulting from cyclophosphamide chemotherapy (Ai et al., 2023). The microRNAs hsa-let-7b-5p and hsa-let-7e-5p, which are abundant in small EVs derived from ADSCs, strongly inhibit the proliferation of the ovarian cancer cell lines SKOV3 and OV90 (Suzuki et al., 2023). ADSCs attached to the CD90-maleimide-pluronic F68-chlorin e6 conjugate (CPFC)

resulted in reduced secretion of paracrine factors such as HGF, fibroblast growth factor-2 (FGF-2), VEGF, angiopoietin-2 (Ang-2), tissue inhibitors of metalloproteinases (TIMP-1 and TIMP-2) which in turn employ $CD3^+CD4^+$ helper T cells and $CD3^+CD8^+$ cytotoxic T cells to destroy tumor cells in mice (Park et al., 2023).

1.2 Calcium Signaling

Calcium (Ca^{2+}) entry in non-excitable cells generally involves two channels, namely, store-operated Ca^{2+} entry (SOCE) and receptor-operated Ca^{2+} entry (ROCE) (Rosado, 2016). Ca^{2+} acting as an important intracellular messenger molecule (Sataric et al., 2023) plays crucial role in the regulation of ADSCs, influencing various cellular processes including proliferation, differentiation, and apoptosis. Adipogenic and osteogenic differentiation of ADSCs are associated with time-dependent decrease of Ca^{2+} oscillations (Torre et al., 2021). Ca^{2+} release induced by carbachol increased the expression of neural specific genes and proteins during neuronal differentiation of ADSCs (Masoumi et al., 2023). ADSCs differentiated to biological cardiac pacemaker cells through overexpressing intermediate conductance Ca^{2+}-activated potassium channel

(SK4) (Yang et al., 2019). Targeting Ca^{2+} signaling pathways offers potential therapeutic strategies for diseases such as obesity and related disorders (Xue et al., 2022). For instance, thermogenic protein irisin-induced Ca^{2+} influx in ADSCs activated ERK and AKT signaling pathways resulting in the expression of uncoupling protein 1 in mitochondria and generation of heat. Comprehensive insight of Ca^{2+} signaling in ADSCs can lead to improved methods for enhancing stem cell proliferation, differentiation and programmed cellular pathways for tissue engineering and regenerative medicine.

1.3 Albumin

1.3.1 Structural Features

Albumin, a multifunctional protein primarily produced by the liver and abundant in plasma, plays several roles in the context of therapeutic application of ADSCs, especially as drug transporter in regenerative medicine. Human serum albumin (HSA) is a monomeric heart shaped globular protein comprising three homologous helical domains (DI, DII, DIII) splitted into A and B sub domains. Petitpas et al. (2001) described seven fatty acid (FA1 - FA7) binding sites in HSA

using X-ray crystallograpgy. Binding site FA1 located in DIB and FA2 in the interface between DIA and DIIA, FA3 and FA4 in DIIIA, FA5 in DIIIB, FA6 in the interface between DIIA and DIIB and FA7 in DIIA (**Fig. 1**).

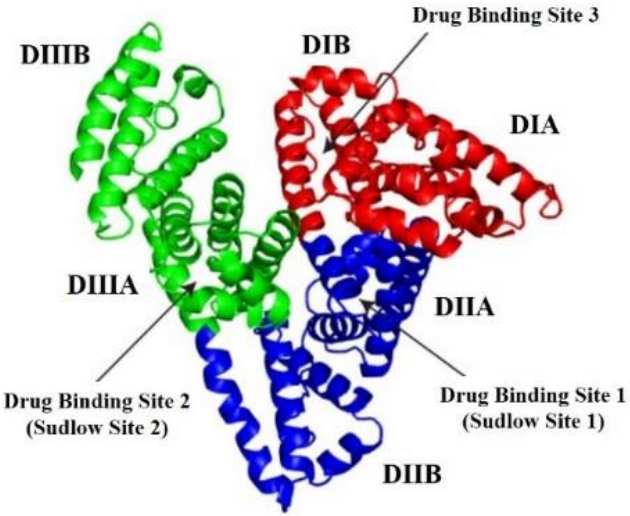

Figure 1. Ribbon Structure Showing Primary Drug Binding Sites on HSA (reprinted with permission from Venianakis et al. (2023)).

1.3.2 Ca^{2+}-mediated Structural Conformation of Albumin

Ca^{2+} as described in the previous section has importance in osteogenesis and exerts immense regulatory effects in

albumin-mediated drug delivery, especially in bone injury or related medication. Patel et al. (2022) described eleven stable Ca^{2+} binding sites out of thirty negatively charged amino acid side chains in BSA and concentration-dependent (0.0 M, 0.02 M, 0.04 M, 0.06 M, 0.08 M and 0.1 M Ca^{2+}) conformational changes, where greater Ca^{2+} concentration resulted in higher distance between N-terminal and C-terminal domains of BSA without affecting secondary structure (**Fig. 2**).

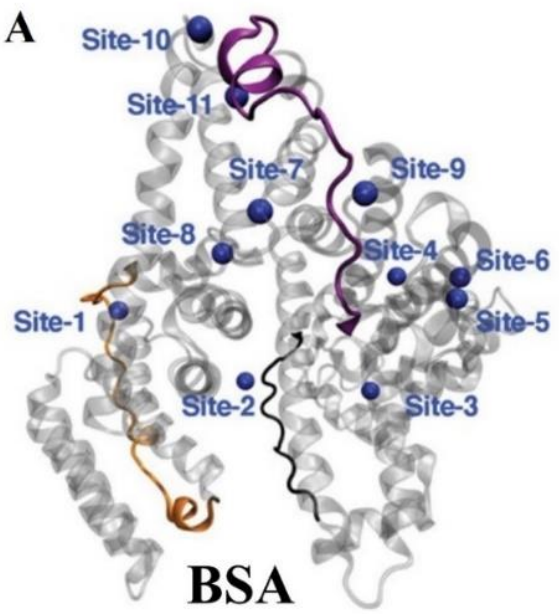

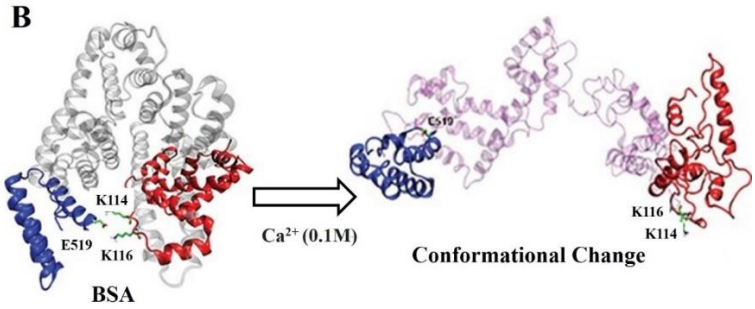

Figure 2. Ca^{2+} binding on BSA triggers conformational change (reprinted with permission from Patel et al. (2022). Copyright 2022 American Chemical Society).

A. Simulation presented eleven Ca^{2+} (shown as blue circles) binding locations on three helices colored gray, violet and orange. Site-7, Site-9 and Site-10 presented with larger spheres denoting the most stable binding site for Ca^{2+}. **B.** Conformational change in BSA structure upon presence of Ca^{2+} (0.1 M) (Patel et al., 2022).

1.3.3 Albumin-associated Therapeutic Promises

Increased chondrogenesis of ADSCs was observed, when low bovine serum albumin (BSA) concentrations were used in cell culture media (Casado-Losada et al., 2024). Albumin-coated polycaprolactone fibers and chondrocyte-derived decellularized extracellular matrix augmented osteoblast proliferation with higher Ca^{2+} deposition, secretion of

collagen, osteopontin, osteocalcin, and bone morphogenetic protein in osteoblast cell cultures (Junka et al., 2022) which could advance the avenue of bone tissue engineering. Albumin magnetic sphere-guided sorting of CD146-positive ADSCs performed as analgesic in osteoarthritis and rectified cartilage damage (Wu et al., 2023). ADSCs are involved in IL-17 secreting T helper (Th17) cell promotion which was enhanced by glycated HSA in the presence of ADSCs derived from lean donors (Pestel et al., 2020). Improved HSA concentration was observed in a clinical trial of autologous ADSC therapy to treat steatohepatitis-related cirrhosis (Sakai et al., 2021). Successful implantation of ADSCs to treat fibrosis and cirrhosis increased serum albumin in a rat model (Nomura et al., 2022). Albumin possesses immense potential in the development of endocytosis-mediated non-viral drug delivery systems to treat brain cancer (Tincu Iurciuc et al., 2023). Miao et al. (2020) identified an albumin-associated lipid-like nanoparticle (NP) uptake pathway in the liver. BSA conjugated with NPs was used to develop targeted drug delivery methods for combination with immunotherapy (Gerke et al., 2022). Higher efficacy was achieved by doxorubicin prodrugs assembled with albumin NPs which

yielded higher drug loading in the acidic tumor environment without digesting the drug (Y. Yang et al., 2023). The exceptional binding capacity of albumin may be used as a dependable drug delivery molecule for the treatment of various life-threatening diseases (Karami et al., 2024).

1.4 Neonatal Fc Receptor

The transmembrane protein FcRn is an important player in transplacental trafficking of IgG (Borghi et al., 2020) which salvages albumin and IgG half-life (Pyzik et al., 2017) in many cell types. FcRn mediates albumin micropinocytosis into primary vascular endothelial cells and transportation towards the plasma membrane (PM) (Pannek et al., 2023). HSA interaction with FcRn is shown in **Fig. 3**.

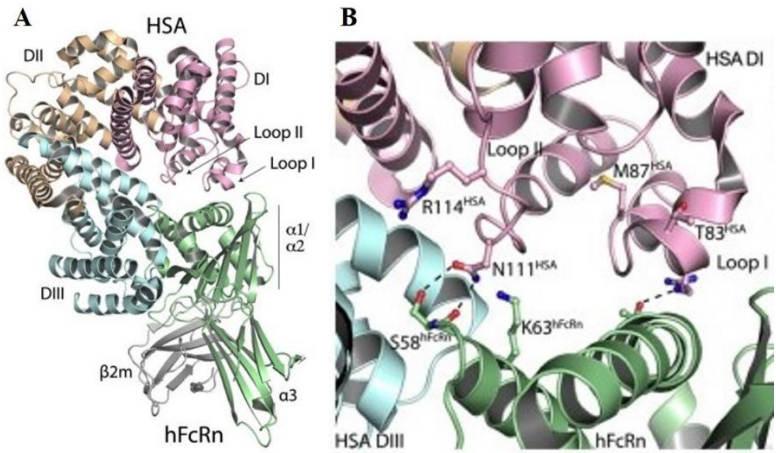

Figure 3. HSA interaction with human FcRn (hFcRn) (reprinted with permission from Nilsen et al. (2018)).

A. Ribbon diagram of HSA-hFcRn complex showing heavy chain α3 of hFcRn in green and light chain β_2m in gray and alpha-helical domains (DI; pink, DII; orange, DIII; cyan) in HSA. **B.** Enlarged view of interacting loop I, loop II in domain DI and domain DIII of HSA with heavy chain α3 in FcRn (from Nilsen et al. (2018)).

Block diagram presentation (**Fig. 4**) of IgG and two albumins engaging with two FcRn anchored by cytoplasmic domain through PM. Domain DI of albumin is interacting with heavy chain α1, α2 of FcRn, whereas domain DIII of albumin is interacting with α3 of FcRn. Heterodimeric FcRn domain β2-microglobulin (β_2m) complexed with constant fragment

(Fc) of monomeric IgG, where antigen-binding fragment (Fab) is in T-conformation juxtaposing PM.

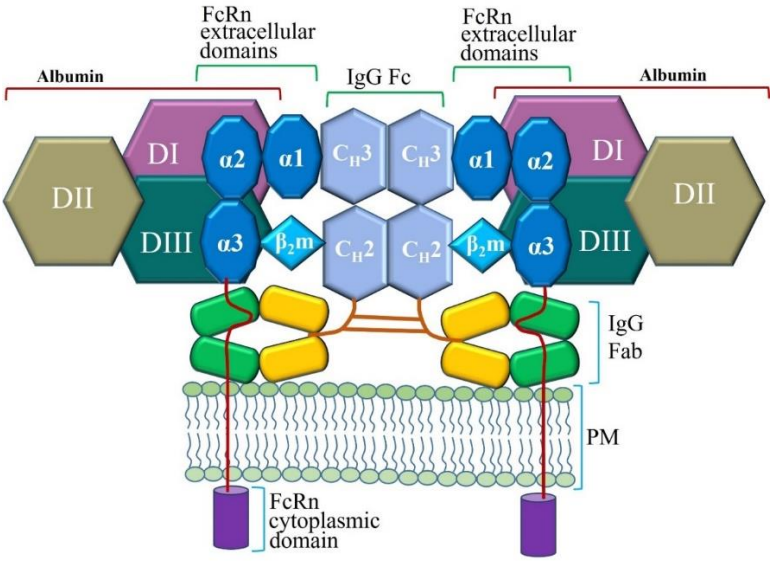

Figure 4. FcRn in complex with IgG and Albumin (modified after: Nilsen et al. (2018), Copyright © 2018, The Author(s) and Pyzik et al. (2023), Copyright © 2023, Springer Nature Limited).

IgG and albumin homeostasis maintenance by FcRn have significant implications for immunotherapeutic development including drug delivery system to treat several autoimmune diseases. FcRn-targeted peptide delivery in human lungs has

important role in enhancing absorption of monoclonal antibodies (Hameedat et al., 2023). Drug delivery to central nervous system through the intranasal pulmonary rout was proposed by exploiting the FcRn-mediated antibody transport mechanism (Herzog et al., 2024). Inhibition of FcRn ameliorates ulcerative colitis by disrupting FcRn mediated recycling of antineutrophil cytoplasm autoantibodies (Wen et al., 2022). Analogs of *Batoclimab* (a.k.a. *IMVT-1401*) and *Nipocalimab* (a.k.a. *M281*) blockade of FcRn significantly reduced recycling of IgG and albumin by downregulating FcRn expression in human embryonic kidney (HEK) cells (Ma et al., 2024). Efgartigimod-mediated FcRn antagonism reduced serum IgG and some protective antibodies in patients with generalised myasthenia gravis, gMG (Guptill et al., 2022) and improved symptoms in gMG and stiff-person syndrome, an autoimmune neurological disorder (Di Stefano et al., 2024; Frangiamore et al., 2024; Fuchs et al., 2024).

1.5 Cellular Uptake Mechanisms

Cellular uptake mechanisms are the processes by which cells internalize various molecules, particles, and other substances from the surrounding environment. These mechanisms are

crucial for maintaining cellular function, responding to environmental changes, and interacting with other cells. Primary pathways through which cells take up materials can be discussed from different points of views such as involvement of pathways with distinct proteins and functions. Therapeutic drug delivery and efficacy largely depends on precision manipulation of specific cellular transporter mechanisms (Grixti et al., 2021).

Diffusion (simple or facilitated) or active transport (primary, symport, antiport) mediated by membrane bound transport proteins are involved in internalization of small molecules such as oxygen, carbon dioxide, glucose, ions etc. (Hartenstein & Martinez, 2019). Larger molecules such as peptides or proteins are transported by endocytosis which involves diverse mechanisms primarily phagocytosis and macro-/micro-pinocytosis (**Fig. 5**).

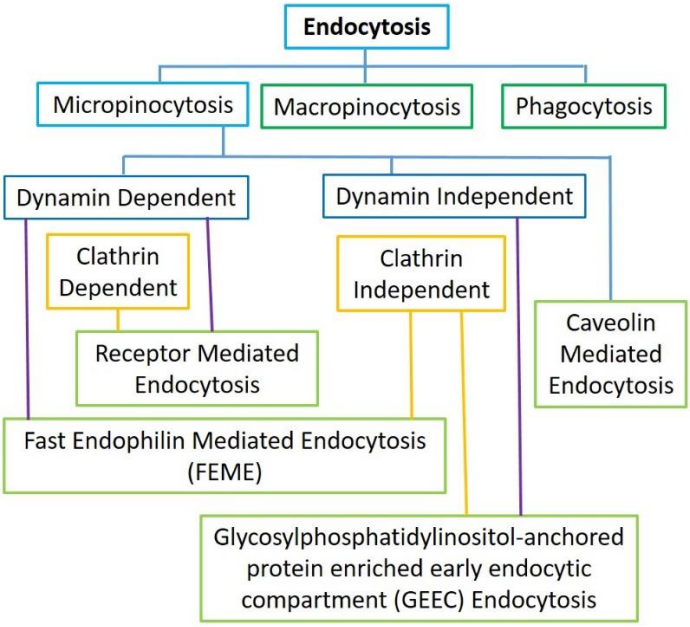

Figure 5. Summarized Overview on Different Endocytosis Pathways (flowchart created based on Rennick et al. (2021).

1.5.1 Phagocytosis

Phagocytosis is the engulfing process for large materials like pathogens (bacteria, viruses), and/or dead cell debris usually employed by the system as an immune defence mechanism. Phagocytic cells present antigens that recognise foreign particles (i.e. pathogens) depending on pattern recognition receptors (PRRs) and detect pathogen-associated molecular patterns (PAMPs). Cells project PM protrusions around the

target to form pseudopodia that fuse together and enclose to form phagosome which later fuse with lysosomes to digest the content. Phagocytosis is initiated by the activation of GTPase dynamin-2 upon the second messenger nicotinic acid adenine dinucleotide phosphate (NAADP)-mediated opening of Ca^{2+} -permeable two-pore channels (TPCs) that upregulates Ca^{2+} -mediated calcineurin activation (Davis et al., 2020). Impaired phagocytosis checkpoints (CD47, CD24, MHC-1, PD-L1, STC-1 and GD2) are crucial for cancer immunotherapy (Liu et al., 2023) (**Fig. 6**).

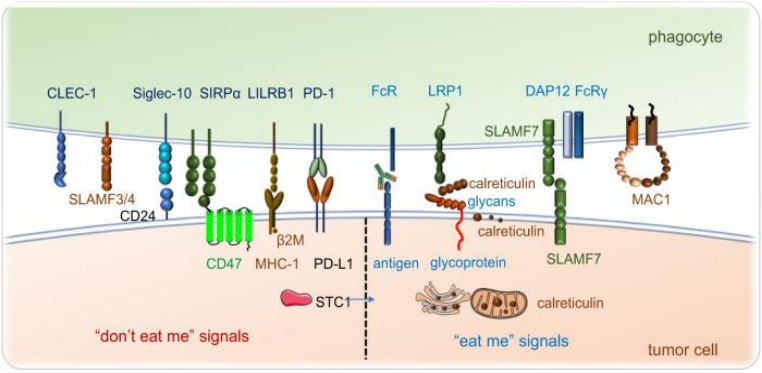

Figure 6. Phagocytosis checkpoints in tumor cells. Overexpression of CD47, CD24, MHC-1, PD-L1, STC-1 and GD2 transmits "don't eat me" signal to escape phagocytosis. Image was obtained from Liu et al. (2023) with permission.

1.5.2 Macropinocytosis

Y. Wu et al. (2024) described initiation of macropinocytosis (stage 1 in **Fig. 7**) activated by numerous intracellular signals like stress such as hypoxia, lack of nutrients and extracellular signals, e.g. growth factors, which in turn activate PI3K/RAS/RAC1 signaling to form macropinosomes (MPS). MPS are formed by PM ruffling and actin cytoskeleton remodelling involving multiple RAB proteins, and ARF protein (stage 2). The maturation of early MPS (stage 3) and volume adjustment is orchestrated by ion channels, such as cation selective TPC (Na^+ channel), chloride channel (ClC-5, $2Cl^-/H^+$ exchanger), and transmembrane protein 206 (TMEM206, Cl^- channel). The late MPS are recycled by EHBP1L1 and ARF6 or are targeted to lysosomes for degradation in stage 4.

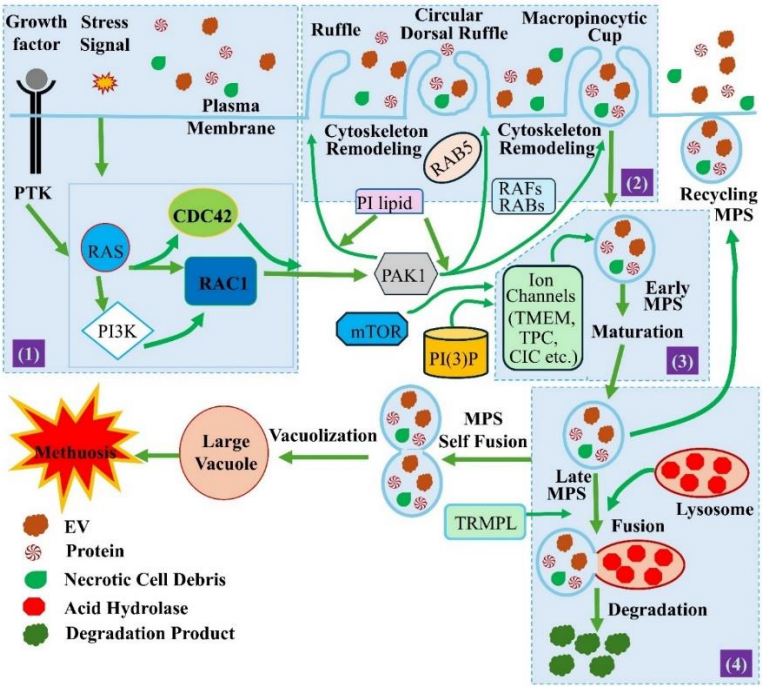

Figure 7. Schematic overview on cellular uptake pathways by macropinocytosis (recreated after Y. Wu et al. (2024), Copyright © 2024, The Author(s)).

1.5.3 Micropinocytosis

Micropinocytosis includes many pathways depending on the involved wide range of protein families, primarily caveolin (cav-1-3), caveolae-associated protein (cavin-1-4), clathrin, clathrin adaptor protein (adaptin; AP-1-5), dynamin (dyn-1-3), and megalin. Caveolin dependent endocytosis cargo size

is ~60 nm and clathrin-mediated endocytosis cargo size is ~100 nm, whereas macropinocytosis cargo size is >200 nm (Rennick et al., 2021).

1.5.3.1 Caveolae-dependent Pinocytosis

Caveolae-dependent endocytosis (CDE) is trafficking molecules by forming caveolae. Caveolae are PM invaginations formed of specific proteins, dominantly cav-1, cavin1, EHD2 and lipid compositions (Hubert et al., 2020). Hubert et al. (2020) described sphingomyelin-mediated stabilization and cholesterol- and glycosphingolipid-mediated scission of caveolae. Various kinds of cytoskeletal filaments associated with caveolae regulate membrane tension, modify the extracellular matrix (ECM) by sensing mechanical properties of the substrate banking on the membrane (Sotodosos-Alonso et al., 2023) (**Fig. 8**). ECM reformation occurs physically by the actin cytoskeleton and chemically by exosome deposition. Non-caveolar invaginations, named dolines, are stabilized by cav-1 and cavin1 binding and deform upon increasing membrane tension, thereby resulting in flattened caveolae which allow cells to adapt complementarily with diverse arrays of mechanical stimuli (Lolo et al., 2023).

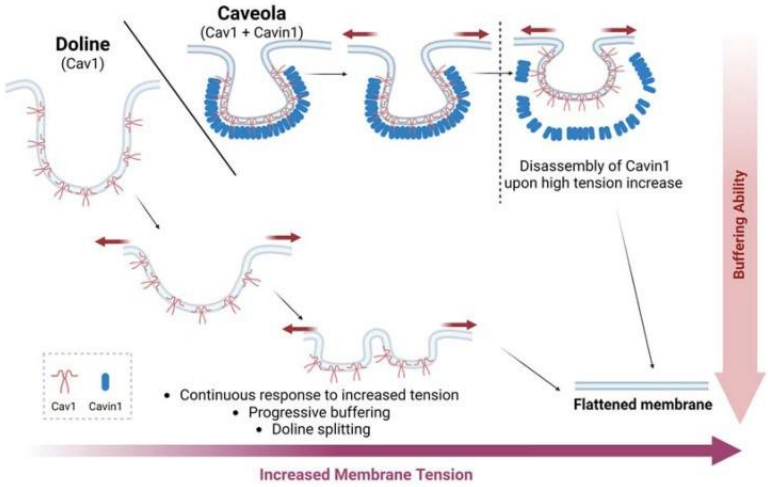

Figure 8. Caveolae formation/deformation based on membrane tension (Sotodosos-Alonso et al., 2023) (image reprinted with permision).

1.5.3.2 Clathrin-mediated Pinocytosis

Clathrin-mediated endocytosis (CME) is employed by eukaryotic cells to transport a wide range of molecules like growth factors, receptors and other large compounds from the PM surface. Clathrin proteins self-assemble into triskelions to organise flat shaped clathrin lattices and progressively bend and manipulate elastic energy from the lattice itself to form curved clathrin coated vesicles (CCVs) that bind to the PM by adaptin (AP-1, AP-2, AP-3) complexes (Sochacki et al., 2021; Tagiltsev et al., 2021). In

adaptor-deficient microenvironment, i.e. more than 1:1 stoichiometry of clathrin to adaptor proteins, clathrin self-assembly can reach up to 20 molecules but fails to bank on PM and spontaneously disassembles the lattice (Guo et al., 2022). Mund et al. (2023) extensively described clathrin-coated structure assembly/disassembly and functional vesicle formation in three different adherently cultured cell lines (SK-MEL-2, U2OS and 3T3). After partial self-assembly on a flat membrane the clathrin coats grow and bend simultaneously. Later the curving speed slows upon reaching a preferred curvature before vesicle scission. CCVs then invaginate on the PM by pushing lattice edges through epsin-mediated actin polymerization independently from the lattice energy in mammalian cells (Yang et al., 2022). Finally, multiple dynamins, which are GTP-ases, work together to generate significant torque, facilitating the twisting and scission of CCVs (Cheng et al., 2021) (**Fig. 9**).

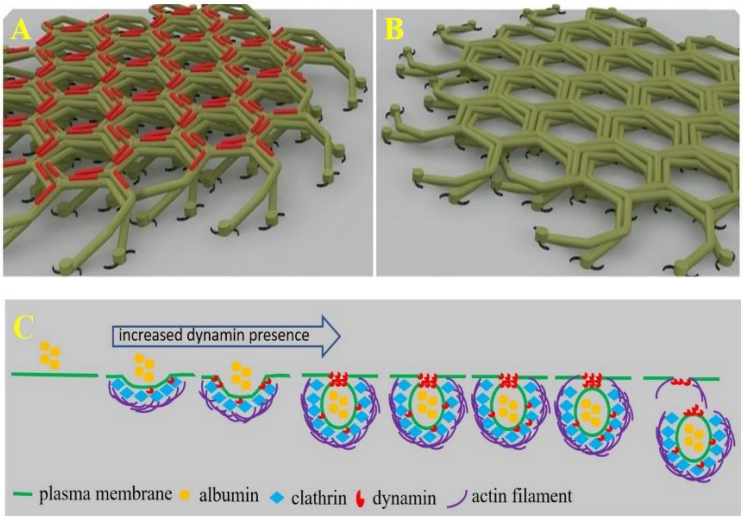

Figure 9. Clathrin lattice formed with triskelia comprising three light chains and three heavy chains.

A: Lattice with both chains, B: Without light chains (reprinted with permission from Dannhauser et al. (2015), C: Lattice transforms into vesicle, and increased presence of dynamin facilitates vesicle fission (recreated with permission after: Cheng et al. (2021).

1.6 Goal of the Study

Being a messenger molecule (Sataric et al., 2023) and possessing multiple binding sites on albumin (Patel et al., 2022) Ca^{2+} supposedly interferes with albumin and IgG trafficking into cells. Albumin is reported to be endocytosed

through different pathways in different cell types, for instance: via megalin, caveolae and cavin in astrocytes (Bento-Abreu et al., 2009), via megalin- and cubilin-mediated endocytosis in renal proximal tubule (PT) cells (Bento-Abreu et al., 2009) and in podocytes (Dobrinskikh et al., 2014), via macropinocytosis in human oral squamous carcinoma cells (Maeda et al., 2022) and glioblastoma (Wang et al., 2023). Endocytotic pathways occurring in ADSCs are currently not sufficiently investigated and the role of Ca^{2+} in these processes are yet unknown.

Transport and recycling of albumin and IgG is mediated by FcRn which determines the half-life of both proteins and has significant impact on immune surveillance (Pannek et al., 2023; Toh et al., 2019). Previously, Ca^{2+}-dependent calmodulin binding sites have been demonstrated on FcRn (Dickinson et al., 2008), suggesting involvement of Ca^{2+} signaling pathways in FcRn-mediated endocytotic processes.

Accounting all these findings we hypothesized, that intracellular Ca^{2+} signaling in ADSCs dictates albumin endocytosis through distinct pathways via FcRn. To test our hypothesis, we set three goals stated below.

A: Characterization of the Albumin Endocytosis Pathways Employed by ADSCs. We investigated the participation of macropinocytosis, caveolae-dependent endocytosis and clathrin-mediated endocytosis in ADSCs.

B: Investigation of Role of Ca^{2+} in Modulating Albumin Endocytosis. To investigate the involvement of Ca^{2+} in modulating albumin endocytosis Ca^{2+} signaling was inhibited on different levels of the signal transduction cascade.

C: Assessment of Ca^{2+} Interplay with FcRn During Albumin Endocytosis. We investigated whether FcRn inhibition affected Ca^{2+} oscillations and albumin/IgG endocytosis in ADSCs.

2. Materials

2.1 ADSC Stem Cell Lines

ADSC lines were isolated from subcutaneous and visceral fat tissues derived from different donors and subsequently processed for different experiments. All cell handling procedures described herein were performed in accordance with the ethical standards laid down in the 1964 Declaration of Helsinki and its later amendments and were approved by the Local Bioethics Committee No. 5092-02/17, AZ 202/21. Written informed consent was obtained from any adults participating in this study. Patient data were anonymized. ADSC isolation was performed using a modified protocol from a previously published study (Zuk et al., 2001). Genetically modified ADSCs where FcRn mRNA expression was inactivated were generated for different experiments. Isolation and culture processes were performed according to established protocols described in the respective ***Method*** sections.

2.1.1 hADSC Cell Lines

The cell lines used in this study are listed below (Table 1) with details. Donors were classified in four age groups comprising young (20–34-year-old), middle (35-49-year-old), old (50-64-year-old) and very old (65-80-year-old) groups. Donors were screened

Table 1. List of stem cell lines isolated and used in different experiments.

Cell ID	Age During Isolation (years)	Gender	Age Group	Origin	Preexisting Disease(s)
ADSC 05	27	Female	Young	Subcutaneous	none*
ADSC 16	26	Female	Young	Subcutaneous	none
vASCm 34	34	Male	Young	Visceral	none
vASCf 23	23	Female	Young	Visceral	none
ADSC 35	40	Female	Middle	Subcutaneous	none
hADSC 23	38	Female	Middle	Subcutaneous	none
vASCf 59	59	Female	Old	Visceral	T2D#

Cell ID	Age During Isolation (years)	Gender	Age Group	Origin	Preexisting Disease(s)
vASCf50	50	Female	Old	Visceral	T2D & S**
ADSCX	75	Female	Very Old	Subcutaneous	T##
ADSCXXII	77	Female	Very Old	Subcutaneous	T
hADSCVIIIn	76	Female	Very Old	Subcutaneous	T
ADSC34	71	Female	Very Old	Subcutaneous	none

*no history of listed diseases, #record of T2D, **record of smoking, ## record of tumour before.

for having any record of tumour (T), diabetes (T2D) and smoking habit (S) prior to the surgery which are noted with their respective cell ID. As exception, the donor of vASCf23 cell line had record of reflux, epilepsy, hypothyroidism and the donor of vASCf50 cell line had record of hypothyroidism, hepatic steatosis, lumbar spine syndrome, ulcer in gastrointestinal tract, lactose intolerance, arterial hypertension.

2.1.2 FcRn^{-} ADSCs

Ab FcRn large subunit p51 protein used to analyse the effect of FcRn. **Table 2** presented all the reagents applied to knockout/block FcRn in ADSCs and si-RNA duplex sequences used in the experiments are listed in **Table 3**.

Table 2. List of Reagents Used to Knockout/block FcRn.

Product	ID	Company
FcGRT (Human)	SR301553	OriGene Technologies Inc., Rockville, MD, USA
RNAse free Resuspension Buffer	SR30005	OriGene
Scrambled Negative Control si-RNA	SR30004	OriGene
TYE 563TM	SR30002	OriGene
INTERFERin	101000028	Polyplus-Sartorius, New York, USA
Nipocalimab	HY-P99037	MedChemExpress

Table 3. List of si-RNA Duplex Sequences Used to Knockout FcRn.

Duplex Sequence	ID	Source
rGrGrArGrCrUrCrUrGrUrUrGrUrGrGrArGrArArGrGrArUGA	SR301553A	OriGene
rCrGrArUrArArUrArUrArArCrArCrGrArGrUrUrUrGrGrGCC	SR301553B	
rGrGrArGrUrUrCrArUrGrArArUrUrUrCrGrArCrCrUrCrAAG	SR301553C	

2.2 Chemical Reagents

2.2.1 Complete Culture Medium

Dulbecco's Modified Eagle Medium (DMEM) High Glucose was used to prepare the complete culture medium (CCM). All other ingredients used in combination of CCM are listed in **Table 4**.

Table 4. List of Ingredients used for CCM.

Ingredients	Ref/Catalog	Company
Dulbecco's Modified Eagle Medium (DMEM) High Glucose	BS, FG0435	Bio & SELL GmbH,
Non-essential Amino	PO8-32100	PANBIOTECH,

Ingredients	Ref/Catalog	Company
L-Glutamine	PO-480100	PAN BIOTECH
2-mercaptoethanol	4227.3	Carl Roth GmbH & Co.
Sodium Pyruvate	PO4-43100	PAN BIOTECH
Penicillin/Streptomycin	PO6-07100	PAN BIOTECH
Fetal Bovine Serum	F7524	Sigma-Aldrich,

2.2.3 Ca^{2+} Channel Modulator

Table 5. List of Ca^{2+} Channel Inhibitors

Reagent	ID	Company
BAPTA-AM	196419	Calbiochem, Merck Millipore, Darmstadt, Germany
SKF-96365 hydrochloride	1147	Tocris, Wiesbaden, Germany
NPS-2143 hydrochloride	17903	Cayman Chemical, Ann Arbor, MI, USA

2.2.4 Endocytosis Blocker

Table 6. List of Different Endocytosis Pathway Inhibitors.

Blocker	**ID /Catalog/ Lot**	**Company**
Macropinocytosis		
Imipramine Hydrochloride	15890	Cayman Chemical, Ann Arbor, MI, USA
EIPA (5-N-ethyle N-isopropyle-amiloride)	14406	Cayman Chemical
Wortmannin	81675	Calbiochem, Merck Millipore, Darmstadt, Germany
Wortmannin	19545-26-7	Cayman Chemical
Cytochalasin D	Cay11330-1	Cayman Chemical
MBQ-167	HY-112842	MedChemExpress, NJ, USA
Caveolae-dependent Endocytosis		
Genistein	Cay10005167	Cayman Chemical
Nystatin	LKT N9874.500	LKT Labs, St Paul, MN, USA
Nocodazole	Sc-3518B	Santa Cruz Biotechnology, Inc., Hidelberg, Germany
Clathrin-mediated Endocytosis		

Blocker	ID /Catalog/ Lot	Company
Monodansylcadaverin	D4008	Sigma-Aldrich
Chlorpromazine	16129	Cayman Chemical
Dyngo-4a	HY-13863	MedChemExpress

2.2.5 Osteogenesis

Table 7. Osteogenesis Differentiation Substances.

Reagent	ID	Origin
Fungizone (Amphotericin B sol 100X)	A2230	United States Biological Inc., Salem, MA, USA
Glycerol-2-phosphate disodium salt hydrate (ß-GP)	50020	Sigma-Aldrich
Dexamethasone	D4902	Sigma-Aldrich
2-Phospho-L-ascorbic acid trisodium salt (Vit C)	49752	Sigma-Aldrich
Recombinant human bone morphogenetic protein-2 (BMP-2)	H4791	Sigma-Aldrich
1α,25 Dihydroxyvitamin D3	D1530	Sigma-Aldrich
Ammonium Hydroxide (NH_4OH)	105426	Merck Millipore

2.2.6 Adipogenesis

Table 8. Reagents Used for Adipogenesis Differentiation.

Substance	ID	Origin
d-Biotin	B4639	Sigma-Aldrich
Dexamethason	4902	Sigma-Aldrich
3-Isobutyl-1-methylxanthin (IBMX)	I5879	Sigma-Aldrich
Insulin (human)	I9278	Sigma-Aldrich
D-Pantothenic acid hemicalcium salt	P5155	Sigma-Aldrich
Rosiglitazon	R2408	Sigma-Aldrich
Transferrin	T8158	Sigma-Aldrich
Triiodo-L-Thyronin (T3)	T6397	Sigma-Aldrich

2.2.7 Chemical Agents for Western Blot

Table 9. List of Chemicals used for Protein Isolation and Quantification.

Chemicals	ID	Company
Protease Inhibitor Cocktail	K271-5000	BioVision Incorporated, CA, USA
EDTA	E5134	Sigma-Aldrich
Deoxycholate	D6750	Sigma-Aldrich
NaCl	3957.1	Carl Roth
Tris	4855.2	Carl Roth

Chemicals	ID	Company
SDS	CN30.3	Carl Roth
Nonidet P40	A1694.0500	AppliChem BioChemica Chemica Synthesis
Potassium Sodium tartrate tetrahydrate	108.087	Merck KGaA, Darmstadt, Germany
Albumin fraction V, Protease-free	T844.4	Carl Roth
Non-fat dried milk powder	A0830,1000	Applichem Panreac ITW Companies

Table 10. List of Lowry Solutions with Respective Composition.

Solution ID	Content(s)
Lowry 1 (L1)	2% Sodium carbonate (w/v) in 0.1N sodium hydroxide solution
Lowry 2 (L2)	1.25% Copper sulphate (w/v)
Lowry 3 (L3)	3.37% Potassium sodium tartrate tetrahydrate (w/v)
Reagent A	L1, L2 and L3 mixed-up in the ratio 100:1:1
Lowry 4 (L4)	1N Sodium hydroxide solution
Lowry 5 (L5)	2N Folin & Ciocalteu's phenol reagent

Table 11. List of Chemicals Used for Electrophoresis and Membrane Transfer.

Chemicals	ID	Company
Aqua B. Braun Ecotainer	0082479E	B. Braun Medical AG, Sempach, Switzerland
NuPAGE 4-12% Bis-Tris Gel	NP0322BOX	Life Technologies Corporation, CA, USA
NuPAGE Sample Reducing Agent	NP0009	Life Technologies
NuPAGE LDS Sample Buffer	NP0007	Life Technologies
NuPAGE Antioxidant	NP0005	Life Technologies
NuPAGE MOPS SDS Running Buffer (20X)	NP0001	Life Technologies
Novex NuPAGE MES SDS Running Buffer (20X)	NP0002	Life Technologies
Novex NuPAGE Transfer Buffer (20X)	NP00061	Life Technologies
Novex Sharp Pre-stained Protein standard	LC5800	Life Technologies

Chemicals	ID	Company
Restore PLUS Western Blot Stripping Buffer	46430	Thermo Fisher Scientific Inc., Illinois, USA

Table 12. Chemicals Used for Enhanced Chemiluminescence (ECL) Solution.

Chemicals	ID	Company
H_2O_2	H1009	Sigma-Aldrich
Luminol	A8511	Sigma-Aldrich
p-Coumaric acid	C9008	Sigma-Aldrich
SuperSignal West Femto Stable Peroxide	1859023	Thermo Fisher
SuperSignal West Femto Luminol/Enhancer	1859022	Thermo Fisher

2.2.9 Fluorescence Reagents

Table 13. List of Fluorescence-labelled Markers/Antibodies.

Reagent	Target	ID	Company
Fluo-4-AM	Intracellular Ca^{2+}	F14201	Invitrogen, ThermoFisher Scientific, MA, USA
Propidium Iodide	Nucleus	P4170	Sigma-Aldrich

Reagent	Target	ID	Company
DRAQ5	Nucleus	4084S	Cell Signaling Technology
Nuclear Green	Nucleus	17540	AAT Bioquest
Alexa-Fluor-488	anti-rabbit	A21206	Invitrogen
Alexa-Fluor-488	anti-mouse	A-21202	Invitrogen
Alexa-Fluor-488	anti-rat	A-21208	Invitrogen
Albumin-Alexa-594	Albumin	A13101	Invitrogen
BODIPY™ FL C5-LactosylCeramide-BSA	Caveolae	B34402	Invitrogen

2.2.10 Solvents

Table 14. List of Solvents Used for Stock Solution Preparation.

Solvent	ID	Company
Aqua B. Braun Ecotainer	0082479E	B. Braun Medical AG
Dulbecco's PBS	PBS-1A	Capricorn Scientific GmbH
DMSO	317275	Calbiochem, MA, USA
Iso-propanol	563935	Sigma-Aldrich
Ethanol	7139041	Otto Fischer, Saarbrücken, Germany

Solvent	ID	Company
Methanol	0082.3	Carl Roth
NaOH	6771.5	Carl Roth

2.2.11 Other Chemicals

Table 15. List of General Chemicals Used in Different Experiments.

Chemicals	ID	Company
Trypsin-EDTA (0.25%), phenol red	25200072	Gibco™, Life Technologies Corporation, ONT, Canada
Gelatin	G-1393	Sigma-Aldrich
Collagenase B	11088807001	Roche Diagnostics GmbH, Mannheim, Germany
Fluoromount G	0100-01	Southern Biotech
Paraformaldehyde	0335.3	Carl Roth
KCl	6781.3	Carl Roth
$CaCl_2$ x $2H_2O$	C7902	Sigma-Aldrich
$MgCl_2$ x $6H_2O$	M9272	Sigma-Aldrich
Glucose Monohydrate	6780.1	Carl Roth
HEPES	HN77.3	Carl Roth
HCl	HN53.3	Carl Roth
Tween-20	P7949	Sigma-Aldrich
Imersionöl	X899.1	Carl Roth
Immersionöl™ 518F	10539438	Carl Zeiss Jena GmbH, Germany

2.3 Antibodies

Table 16. List of Antibodies Used for Western Blot and Immunocytochemistry.

Antibody (Host)	**Clonality/Conjugation**	**MW (kDa)**	**Producer**	**Cat. /Ref.**
Caveolin 1 (Mouse)	Monoclonal	~20	Life Technologies	MA3-600
Anti-LRP-2/Megalin (Mouse)	Monoclonal	250 - 600	Sigma-Aldrich	MABS489
Osteocalcin (Rabbit)	Polyclonal	10-15	BIOSS	Bs-4917R
Adiponectin (Rabbit)	Monoclonal	~36	Invitrogen	701148
FcGrT (Rabbit)	Polyclonal	40-50	Invitrogen	PA5-97738
OCT4 (Rabbit)	Polyclonal	~40	Novus Biologicals	NB100-2379
SOX2 (Rabbit)	Polyclonal	40	Invitrogen	PA1-16968
Nanog (Goat)	Polyclonal	38	Abcam	Ab77095
Vinculin (Rabbit)	Monoclonal	130	Abcam	Ab129002

Antibody (Host)	**Clonality/Conjugation**	**MW (kDa)**	**Producer**	**Cat. /Ref.**
β-Actin (Rabbit)	Polyclonal	40	Biolegend	622102
Anti-Rabbit (Donkey)	HRP		Abcam	Ab205722
Anti-Mouse	HRP		Abcam	Ab97240
Anti-Goat (Donkey)	HRP		Abnova	PAB10570
IgG Human	Unconjugated		Sigma-Aldrich	I2511
Nipocalimab	Anti-FcRn		MedChemExpress	HY-P99037

2.4 Buffers

Table 17. Ingredients Used for Tyrode Buffer (in dH_2O).

Substance	**Concentration (mM)**
NaCl	125
KCl	5
$CaCl_2$ x $2H_2O$	2
$MgCl_2$ x $6H_2O$	2
HEPES	25

Substance	Concentration (mM)
Glucose Monohydrate	5.5
Pyruvate	5
pH: 7.4 adjusted with NaOH	

Table 18. Ingredients Used for E1 Buffer (in dH_2O) Preparation.

Ingredients	Concentration (mM)
NaCl	135
KCl	5.4
$CaCl_2$ x $2H_2O$	1.8
$MgCl_2$ x $6H_2O$	1
Glucose Monohydrate	5
HEPES	10
Na-Pyruvate	1.22% (ml)
pH: 7.4 adjusted with NaOH at 23° C	

Table 19. Ingredients for Radioimmunoprecipitation Assay (RIPA) Buffer.

Ingredients	Concentration
Tris (pH 7.4)	50 mM
NaCl	150 mM
Nonidet P-40	1%
SDS	0.5%
Sodium deoxycholate	0.5%

Table 20. Ingredients Used to Prepare Washing Buffers.

Ingredients	**Concentration (mM)**
PBS (10x) (pH: 7.4 adjusted with NaOH)	
KCl	2.7
KH_2PO_4	2.0
NaCl	137
Na_2HPO_4 x $2H_2O$	10
TBS (20x) (pH: 7.4 adjusted with NaOH)	
Tris	50
NaCl	150
Tween-20 (added to prepare 1x solution of PBST/TBST in Aqua)	**0.1%**

Table 21. Composition of Different Ingredients to Prepare ECL solution.

Ingredients	**Concentration (mM)**
H_2O_2	3
Luminol	1.25
p-Coumaric acid	225
Tris-HCL, pH:7.4 adjusted using concentrated HCL	100

2.5 Equipments

Table 22. List of Cell Culture Equipments.

Instrument	**Ref.**	**Company**
Neubauer Chamber	Improved	Labor Optik, Lancing, UK
CryPure Tube 1.8 ml	72.379.992	SARSTEDT AG & Co. KG, Nümbrecht, Germany
Syringe filter, 0.20 µm	83.1826.001	SARSTEDT
BD Microlance™ 3 Needle	301300	Becton, Dickinson S.A., Ctra. Mequinenza, Spain
BD Discardit™ II Syringe	300296	Becton, Dickinson S.A.
75 cm^2 Tissue Culture Flasks	156472	Corning, New York, USA
TC Dish 60 (22.1 cm^2)	83.3901	SARSTEDT
VWR Tissue Culture Dish 60.8 cm^2	734-2321	VWR International LLC, PA, USA
CELLSTAR Tubes 50 ml	227261	Greiner Bio-One, Kremsmünster, Austria
BD Falcon Tubes 15 ml	352096	BD, One Becton Drive, NJ, USA
TC-Plate 24 Well	83.3922	SARSTEDT
12 mm Cover slips	01-0012/1	R.Langenbrinck GmbH, Emmendingen Germany

Instrument	Ref.	Company
Microscope Slides 7107	1156- 2203	Fisher Scientific GmbH, Schwerte, Germany
µ-Slide 8 Well	80806	Ibidi GmbH, Gräfelfing, Germany
CELLSTAR Serological Pipette 10 ml	607180	Greiner Bio-One, Frickenhausen, Germany
CELLSTAR Serological Pipette 5 ml	606180	Greiner Bio-One
Pipette Tips, 10 µl	70.3010.275	SARSTEDT
Pipette Tips, 20 µl	70.3030.385	SARSTEDT
Pipette Tips, 100 µl	70.3030.255	SARSTEDT`
Pipette Tips, 200 µl	70.3031.355	SARSTEDT`
Pipette Tips, 1000 µl	70.3060.375	SARSTEDT
Costar Cell Scraper	3010	Corning Incorporated, Mexico
Fireboy		Integra Biosciences, Bieberatal, Germany
Pipetus standard		Hirschmann Laborgeräte, Germany
Eppendorf Reference PhysioCare concept		GILSON, France
Finnpipette		ThermoLabsystems
Pipetman		GILSON

Table 23. List of Instruments Used for Microscopy.

Article	**Origin**
Axiovert 40C Trinocular (Art # 6441)	Carl Zeiss AG, Oberkochen, Germany
LEICA TCS SP 2AOBS	Leica Microsystems, Heidelberg, Germany
LEICA DMIRE2	Leica Microsystems
HC Plan s 10x/22 br. m	Leica Microsystems
HC XPL APO 40x/1.25-0.75	Leica Microsystems
Biozero BZ-Series KEYENCE (Art#BZ-X810)	KEYENCE Corporation, Osaka, Japan
Plan Apo 20x NA0.75	KEYENCE Corporation

Table 24. Cryo Storage Facilities Used in This Study.

Instrument	**Origin**
HERA freeze HLE30086V (-86° C Freezer)	Thermo Fisher Scientific, LLC, USA
Freezer, Type: AB400NS/S (Art # FR213TEC)	Thermo Fisher Scientific, Italy
BOSCH economic no frost (-20° C Freezer)	Bosch, Gerlingen, Germany
SIEMENS KD40R423	Siemens AG, Munich, Germany
Liquid Nitrogen Storage Tank (GT38, IATA-BVT N° 1039/47)	Air Liquid

Table 25. List of Other Equipments to Perform Different Experiments.

Instrument	Ref.	Company
Kontes Pellet Pestle Motor	Z359971-1EA	Sigma-Aldrich
Disposable Pestles	BAF199230001	Sigma-Aldrich
Heraeus HERASafe		ThermoFisher Scientific
Heraeus Multifuge 1S-R Centrifuge		ThermoFisher Scientific
Heraeus HERAcell 240		ThermoFisher Scientific
Eppendorf Centrifuge	5417 C	Eppendorf AG, Hamburg, Germany
Eppendorf Centrifuge	5414 S	Eppendorf AG
TECAN infinite M200		TECAN, Männedorf, Switzerland
TB1Thermoblock	2V0032019	Whatman Biometra GmbH, Göttingen, Germany
TB2Thermoblock	JC0708021	Whatman Biometra
Edmund Bühler KL- 2		Edmund Bühler, Bodelshausen, Germany
Stuart Roller mixer	SRT6	Cole-Parmer Instrument Company, USA

Instrument	Ref.	Company
Stuart See-Saw Rocker	SSM4	Cole-Parmer Instrument Company, USA
Heidolph Polymax 1040		Heidolph Instruments, Germany
Lab Dancer D S40		VWR, Germany
Stuart (SA8/011578)		BIBBY STERILIN LTD, UK
IKA RH-KT/C		IKA, Staufen, Germany
pH 211 Microprocessor pH Meter		Hanna Instruments, Rhode Island, USA
LAUDA AQUAline AL 25		Lauda DR. R. Wobser, Lauda, Germany
LAUDA AQUAline AL 12		Lauda DR. R. Wobser
Sartorius Balance	ENTRIS153I-1S	Sartorius Lab Instruments, Germany
Mettler Toledo Balance	AB265-S	Mettler Toledo, Switzerland
PowerEase 500	360423-106	ThermoFisher Scientific
XCell SureLock Mini-Cell electrophoresis		ThermoFisher Scientific

Instrument	Ref.	Company
Immobilion P Transfer Membranes		Merck
Saugpapier (filter paper)	361300	Biotech-Fisher, Reiskirschen, Germany

2.6 Softwares

Table 26. List of Softwares Used in This Study.

Software	Application	Company
Chemi-Capt 5000	Imaging	VILBER, Eberhardzell, Germany
ImageJ	Image analysis	National Institutes of Health, MD, USA
LAS AF Lite 3.3.0	Image analysis	Leica Microsystems
Microsoft Excel, Office 2006	Data analysis	Microsoft, Redmond, WA, USA
Microsoft Word, Office 2006	Documentation	Microsoft
Microsoft PowerPoint, Office 2006	Presentation	Microsoft
GraphPad InStat, version 3.06	Data analysis	GraphPad Software Inc., MA, USA

Software	Application	Company
Tecan Magellan	ELISA	Tecan, Männedorf, Switzerland
Endnote	Reference	Clarivate Analytics, Boston, USA

3. Methods

3.1 Cell Culture and Maintenance

3.1.1 CCM

Ingredients stored in 4° C freezer were warmed in water-bath prior mixing to prepare CCM under the laminar cell culture hood. 2-mercaptoethanol stock solution was prepared by diluting 35 µl 2-mercaptoethanol in 50 ml PBS in safety hood, filtered by 0.20 µm non-pyrogenic syringe filter and stored in 4° C freezer. FBS was inactivated in a waterbath at 56º C for 30 min and subsequently cooled on ice for 1 h.

1.22% NEA (non-essential amino acids), L-glutamine, 2-mercaptoethanol, pyruvate, 0.62% Penicillin/Streptomycin and 18.4% FBS were added and mixed well with DMEM to prepare cell culture medium.

3.1.2 Culture Plate Gelatinization

Cover slips (12 mm) were sterilized with fire (Fireboy, Integra Biosciences), placed in a 24 well plate and subsequently incubated with 0.5 ml/well gelatin (G1393, Sigma) for 30 min at RT. Applied gelatin was aspirated and remaining gelatin was washed off for two times with 1 ml/well PBS, and subsequently placed under a cell culture hood for 1 h for air drying.

3.1.3 Stem Cell Isolation

The ADSC isolation procedure was performed under the laminar flow chamber, and all the used tools were disinfected previously. Tyrode buffer (with 0.5% Pen/Strep) was added to Collagenase (4 mg/ml) to prepare adipose tissue lysis buffer. Falcon tubes containing fat tissue obtained from surgery was kept at 4º C on ice. Tissue was washed two times with pre-warmed (37º C) cell culture medium (DMEM) to remove remaining red blood cells (RBCs). Remaining connective tissues were removed, and the fat was minced with scissors and then with scalpels to obtain small pieces which were placed in cell culture medium to avoid air-drying. After removing the culture medium properly chopped tissue was incubated in falcon tubes with 15 ml lysis

buffer at 37° C for 60 min on a shaker. Subsequently the falcon tubes containing the mix was kept under hood at rest until a solid phase on the bottom and a liquid phase on the top appears. Fresh pre-warmed culture medium was added to the collected liquid phase up to 45 ml final volume and centrifuged at 500 x *g* for 10 min. Fresh culture medium (1 ml) was added to the pellet after removing the supernatant and mixed well to seed onto two 100 mm Petri dishes containing CCM. Cells were washed with pre-warmed cell culture medium, and medium was exchanged with CCM daily to remove remaining RBCs, and cells with fibroblast-like structure became dominant. After reaching 90% confluency cells were expanded, freeze-stored and validated for stemness properties.

3.1.4 Culture Method

Handling of cells was performed under completely aseptic conditions under the cell culture hood. The hood was disinfected using 80% ethanol before initiating the process and in between steps if necessary to avoid any cross contamination between different cell lines.

3.1.4.1 Freezing of ADSCs

Freezing medium was prepared by adding 80% FBS, 20% DMSO to the 4º C cold CCM and kept on ice. Culture medium was aspirated from the culture (Petri dish, T25/T75 flask) and the remaining medium was washed off by warm (37º C) PBS. Cells were detached from the plate by trypsinization (Trypsin-EDTA, 6 ml/100 mm Petri dish) for 2 min at 37° C in 6% CO_2 incubator. Subsequently cells were collected in 50 ml Falcon tubes and 18 ml of CCM was added to stop the enzymatic reaction. After centrifugation for 5 min at 209 x *g* the supernatant was carefully removed, and subsequently 1 ml freezing medium was added by sliding on wall of the Falcon tubes and mixed gently. Cells were then collected to cryotubes on ice. Initially cells were stored in the -80° C freezer (maximum 1 month) and then transferred to a liquid nitrogen tank (-196° C) for prolonged storage.

3.1.4.2 Thawing of ADSCs

Cells preserved in liquid nitrogen tank (or -80° C freezer) were taken out in ice box and quickly warmed in water bath at 37° C till a tiny portion of ice was still present. Cells were mixed gently and seeded to a 6 cm culture plate (Petri dish / flask) containing fresh pre-warmed CCM. Cells were incubated at 37° C in 6% CO_2 and fresh CCM was added

every second day till the cell monolayer reached the desired level of confluency.

3.1.4.3 ADSC Cell Culture for Experiments

Upon reaching the desired level of confluency the CCM was aspirated, remaining medium was washed off with pre-warmed PBS and trypsinization was done as described previously. The number of cells was calculated using a Neubauer counting chamber. After centrifugation (5 min at 209 x *g*) 1 ml fresh CCM was added and cells were seeded at a cell density of $1.5x10^4/cm^2$ (unless otherwise stated) to new culture plates according to the experimental requirement.

3.2 Differentiation of ADSCs

Isolated ADSCs were validated for stemness through differentiation of osteogenic and adipogenic cell lineages and analysed by Western blot and immunohistochemistry (IHC).

3.2.1 Osteogenesis

3.2.1.1 Culture Method

ADSCs were seeded ($1.5x10^4/cm^2$) in 100 mm Petri dishes and 24 well plates containing CCM (10% FBS) on gelatin-coated cover slips. After reaching 80-85% confluency, the continuous stimulation protocol (Kroeze, R.J. et al., 2011) with recombinant human bone morphogenetic protein-2 (BMP-2) and 1,25-dihydroxyvitamin-D3 (Vit-D3) was applied to induce osteogenesis. The induction medium (1 ml/well of 24 well plate) was exchanged every second day till three weeks.

CCM (10% FBS) was used to prepare the osteogenic induction medium which was supplemented with Fungizone (final concentration, f.c. 2.5 µg/ml), Glycerol-2-phosphate disodium salt hydrate (ß-GP) (f.c. 50 ng/ml), 2-Phospho-L-ascorbic acid trisodium salt (Vit-C) (f.c. 50 µg/ml), Dexamethasone (f.c. 10 nM), BMP-2 (f.c. 100 ng/ml), Vit-D3 (f.c. 10 ng/ml). Medium preparation was done under the safety hood without light since Vit-D3 is light sensitive.

3.2.1.2 Validation of Osteogenesis

Alizarin Red S (ARS) staining (Gregory et al., 2004) and osteocalcin IHC (Kroeze et al., 2011) were applied to

investigate osteogenic differentiation. For ARS staining PBS (without Ca^{2+} and Mg^{2+}) washed cells were fixed with 4% PFA for 15 min at RT and gently washed 3 times with dH_2O. After completely removing the fixative cells were incubated with 500 µl of 40 mM ARS per well at RT for 45 min on a shaker in the dark. ARS was removed by washing 5 times with dH_2O. After draining all water cells were analysed on phase contrast microscope.

For IHC experiment, sample ADSCs were fixed with PFA (4%) at RT for 40 min, then PFA was drained out and remaining PFA was washed off three times with PBS. Cells were blocked for 1 h with 10% FBS at RT and incubated with an anti-osteocalcin antibody (1:200 dilution, BIOSS, Cat# Bs-4917R) for overnight at 4° C. After washing 3 times with PBS, ADSCs were incubated with a secondary IgG-conjugated Alexa Fluor 488 (1:400, anti-rabbit) antibody for 1 h at RT. Sample cells were incubated with DRAQ 5 (1:2000) for nuclear staining and investigated using C-LSM.

3.2.2 Adipogenesis

3.2.2.1 Culture Method

For adipogenic differentiation, ADSCs were seeded ($1.5x10^4/cm^2$) in 100 mm Petri dishes and 24 well plates containing CCM onto gelatin-coated cover slips. After reaching 80-85% confluency, cells were incubated with complete differentiation medium (CDM) for 6 d to induce the differentiation and subsequently with maintenance medium (MM) for the next 6 d. The control cells were given only 3% FBS containing culture medium. Medium volume was 10 ml/100 mm Petri dish and 1 ml/well of 24 well plates during the experiment.

To prepare CDM, fresh culture medium was used as previously described (section 4.1.1) with exception of 3% FBS. The medium was supplemented with D-Biotin (3.3 mM), dexamethasone (50 µM), 3-Isobutyl-1-methylxanthin (IBMX, 500 µM), human insulin (1.7 mM), pantothenic acid (17 µM), rosiglitazone (1 µM), transferrin (0.1 % of 100 mg/ml) and triiodo-L-thyronin (T3, 20 µM). Maintenance medium lacks rosiglitazone and IBMX. Reagents stock solutions were prepared according to the manufacturer's guidelines.

3.2.2.2 Validation of Adipogenesis

Conventional Oil Red O protocol for lipid staining and western blotting for adiponectin protein expression was performed to verify successful adipogenesis. Oil Red O stock solution was prepared with 150 mg Oil Red O in 50 ml iso-propanol on magnetic stirrer and stored at room temperature (RT). Working solution was prepared by adding stock liquid with ddH_2O at 6:4 ratio and filtered with Whatmann filter paper.

At desired time points cells were washed with pre-warmed PBS for 3 times and fixed with 4% PFA for 45 min at RT. Subsequently cells were washed three times to remove remaining PFA solution and incubated with 300 µl freshly prepared Oil Red O working solution for 1 h at RT on shaker avoiding light exposure. Cells were washed with ddH_2O until discoloration and air-dried cover slips were fixed on glass slides with Fluoromount solution. Cells were analysed with laser scanning microscopy (Leica SP2 AOBS, C-LSM) or Biozero BZ-Series (KEYENCE) at 518/>575 nm (excitation/emission).

3.3 Ca^{2+} Oscillations Recording

ADSCs were cultured as a monolayer on gelatin-coated glass cover slips in 24 well plate till confluency. To perform Ca^{2+} oscillations recording, fluorescence dye Fluo-4, AM (10 mM in DMSO, stock concentration (s.c.) was supplemented to CCM (1:1000) medium (without FBS unless otherwise stated) to reach a f.c. of 10 µM. Subsequently, ADSCs were incubated in Fluo-4, AM-conditioned medium for 20 min at 37° C in 6% CO_2 incubator. ADSCs monolayer was washed with fresh culture medium and analysed by C-LSM (objective: HC Plan s 10x/22 br. M) for Ca^{2+} oscillations. Fluorescence was recorded with 3 s intervals for 10-15 min depending on the experiment using an argon ion laser at 488/>515 nm (excitation/emission). Oscillating cells (50 +) were selected using overlay mask (region of interest, ROI), subsequently, data of fluorescence intensity at respective time (s) was recorded by Leica image analysis software (LAS AF Lite 3.3.0) and stored for analysis.

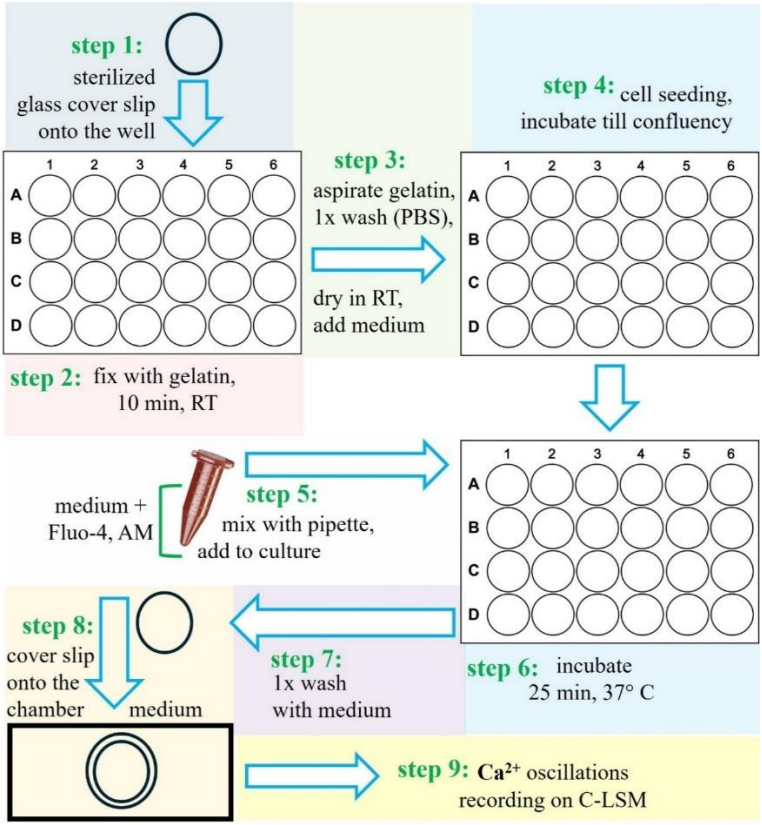

Figure 10. Schematic Presentation for Ca^{2+} Oscillations Experiment.

3.3.1 Analysis of Ca^{2+} Oscillations in ADSCs

ADSCs actively presenting recurrent fluctuation of green Fluo-4 fluorescence were counted as actively oscillating

cells and the value of mean active cells was analysed by using following equation:

$$\text{Active cells (\%)} = \left(\frac{\text{Number of cells with fluctuation of Fluo}-4\text{ fluorescence}}{\text{Total number of selected cells}}\right) * 100$$

$$\text{Mean Active cells (\%)} = \frac{\text{Active Cells (\%)}}{\text{Number of Experiments}}$$

Stored data of fluorescence intensity was processed in Microsoft Excel (Office 2006) data analysis software. Number of peaks was calculated for each selected cell and presented as the mean value from each experimental group. Amplitude of peaks was calculated as the percentage of fluorescence variation (F/F_0) with respect to the resting level fluorescence (F_0), which was set to 1.

3.4 Albumin Endocytosis Tracking

Sun H et al.; 2022 used fluorescein isothiocyanate-labelled albumin (FITC-albumin) as a potent marker of endocytosis in ADSCs, whereas we deployed Alexa-594 conjugated bovine albumin (Albumin-Alexa-594) for our experiments. Albumin-Alexa-594 was dissolved in DMSO to prepare 60

mM stock solution and aliquots were stored in the -20º C freezer. When sample cell cultures became confluent, they were incubated for 1 h in the 6% CO_2 incubator at 37° C with medium containing Albumin-Alexa-594 (300 µM) and analysed in C-LSM using a Leica LSM SP2 AOBS (Leica, Wetzlar, Germany) equipped with a 40x oil-immersion objective (numerical aperture 0.7) and a He/Ne 594 nm laser line. Emission was recorded in single cells at > 618 nm and analysed by the image analysis software of the confocal setup. Image analysis was performed according to the protocol described in ***section 3.9***.

3.4.1 Effect of DMSO on Albumin Uptake in ADSCs

We have applied DMSO as a solvent for most of the reagents (according to the manufacturer guidelines). Hence, it was necessary to investigate how ADSCs react upon DMSO treatment during albumin endocytosis. We preincubated ADSCs with DMSO (1 µl/ml CCM) for 1 h and co-incubated with Albumin-Alexa-594 (300 µM) for another 1 h to analyse the effect on endocytosis. Fluorescence analysis at C-LSM presented no significant difference in albumin

uptake in DMSO-treated cells (**Fig. 11**), thus excluding any effect of the vehicle on endocytotic processes.

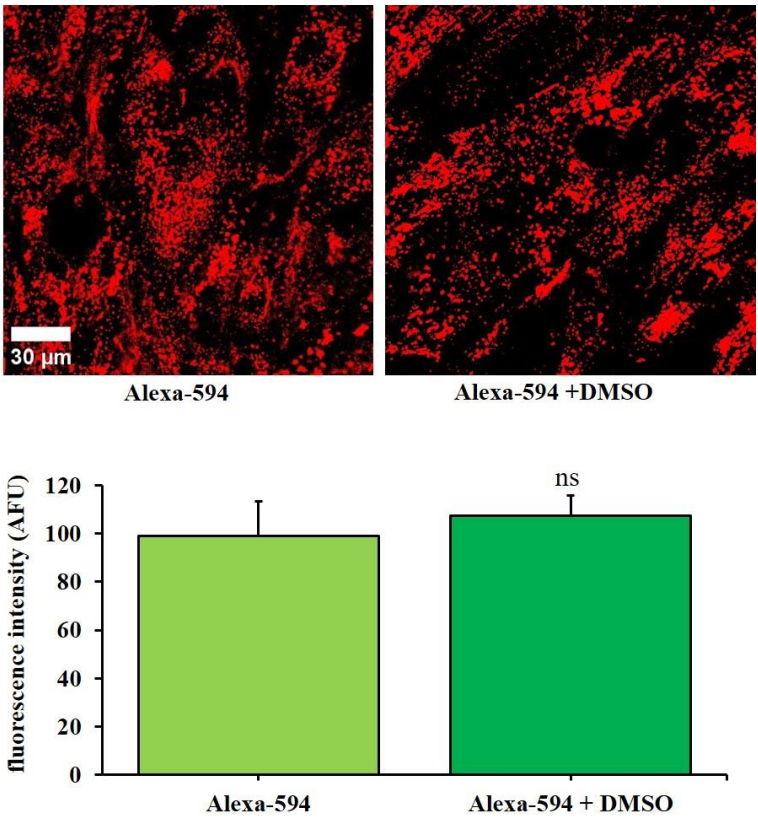

Figure 11. Effect of DMSO on Albumin Endocytosis in ADSCs.

Completely confluent ADSCs were incubated with Albumin-Alexa-594 (300 µM) for 1 h at 37° C in 6% CO_2 incubator. The bar chart presents differences of Alexa-594 fluorescence in ADSCs. Values are given as mean ± SD of

four individual experiments, data are statistically not significant, ns = >0.05. Scale bar (30 μm) subjected for both images.

3.4.2 Intervention with Endocytosis Inhibitors

Different endocytosis blockers were applied to track albumin internalization pathways in ADSCs. Cells were pre-incubated with blockers for 1 h in the 6% CO_2 incubator at 37° C and then for another h with fluorescence-labelled albumin (Albumin-Alexa-594, 300 μM) in presence of respective blockers (Lin et al., 2018). After washing with PBS (without Mg^{2+}, Ca^{2+}) cells were investigated and analysed by C-LSM.

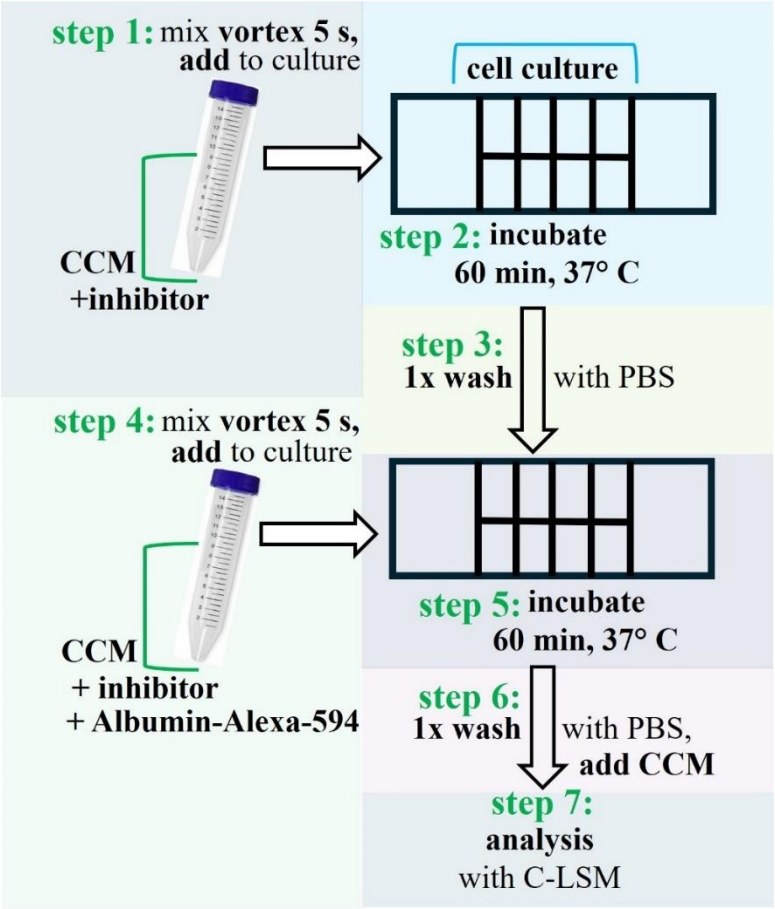

Figure 12. Experimental Design for the Investigation of Albumin Endocytosis with Different Inhibitors.

3.4.2.1 Macropinocytosis Inhibitors

The effects of *5-N-Ethyl-N-Isopropyl-Amiloride* (*EIPA*), *Cytochalasin D* (*CD*), *Wortmannin* (*Won*), *Imipramine* (*Imp*)

and *MBQ-167* were investigated to elucidate macropinocytosis of albumin in ADSCs. Stock solutions were: *EIPA* (10 mM), *CD* (50 mM), *Won* (10 mM), *Imp* (10 mM), and *MBQ-167* (10 mM) prepared using DMSO as solvent. Stock solution aliquots were stored according to the manufacture's guidelines.

3.4.2.2 Caveolae-dependent Inhibitors

The CDE inhibitors *Genistein* (*Gen*), *Nocodazole* (*Noco*), and *Nystatin* (*Nyn*) were tested for albumin uptake analysis. *Gen* (100 mM) and *Noco* (10 mM) stock solutions prepared using DMSO as solvent. *Nyn* was dissolved in methanol to prepare a 50 mM stock solution.

3.4.2.3 Clathrin-mediated Inhibitors

Chlorpromazin (*CPZ*) is a potent inhibitor of CME. *Dyngo-4a* blocks CME with higher specificity by interfering dynamin to bind clathrin-coated vescicles. Both *CPZ* and *Dyngo-4a* were dissolved in DMSO to prepare 10 mM stock solutions, and aliquots were stored according to the manufacture's guidelines.

3.4.3 Intervention with Ca^{2+} Channel Modulators

Similar protocols were applied for Ca^{2+} channel modulators as described in ***section 3.5.1***. For incubation medium buffer solution (E1, ***section 2.4***) was used instead of cell culture medium. In case of Ca^{2+} release inhibitor experiments, incubation buffer lacked Ca^{2+} to avoid interference with the Ca^{2+} scavenging between the extracellular and intracellular region. ADSCs were preincubated for 1 h in 37 °C in respective E1 buffers (with or without Ca^{2+} 1.8 mM) before incubation with the inhibitors. The E1 buffer (without Ca^{2+}) was used for washing steps. 10 mM stock solutions in DMSO were prepared from each agent described below, and aliquots were stored in -20° C freezer.

3.4.3.1 Ca^{2+} Release Inhibitor

BAPTA-AM binds Ca^{2+} only after the acetoxymethyl (-AM) group is cleaved by cytoplasmic esterase upon entering the cell and can be applied as a selective intracellular Ca^{2+} scavenger that does not bind Mg^{2+} or protons. It maintains cytosolic Ca^{2+} homeostasis. *BAPTA* is trapped inside the cell since it is membrane-impermeable and prevents Ca^{2+} release

from intracellular stores that elevate cytosolic Ca^{2+} (Ferdowsi et al., 2022).

3.4.3.2 Ca^{2+} Entry Inhibitor

The receptor potential antagonist *SKF-96365* hydrochloride (*SKF-96365*) inhibits store operated Ca^{2+} entry (SOCE) via voltage gated T-type Ca^{2+} channels (VGCCs) (Singh et al., 2010). *SKF-96365* prevents Ca^{2+} entry in human neutrophils, platelets and endothelial cells without interfering Ca^{2+} release (Merritt et al., 1990).

3.4.3.3 Ca^{2+} Sensing Receptor Antagonist

The calcilytic agent *NPS-2143 hydrochloride* (*NPS-2143*) acts as a Ca^{2+} -sensing receptor (CaSR) antagonist through inhibition of whole cell VGCC currents extracellularly to maintain intracellular Ca^{2+} homeostasis (Greenberg et al., 2016). *NPS-2143* is reported to alter epidermal function and UV-induced DNA damage through CaSR (C. Yang et al., 2023).

3.4.3.4 Different Ca^{2+} Concentrations

Albumin has distinct Ca^{2+} binding sites which determine the conformational structure of the protein (Patel et al., 2022). Three different Ca^{2+} concentrations (0.5 mM, 1.0 mM and 1.8 mM) were investigated to analyse the effect on albumin

internalization by ADSCs. The performed protocol is depicted in **Fig. 13** below.

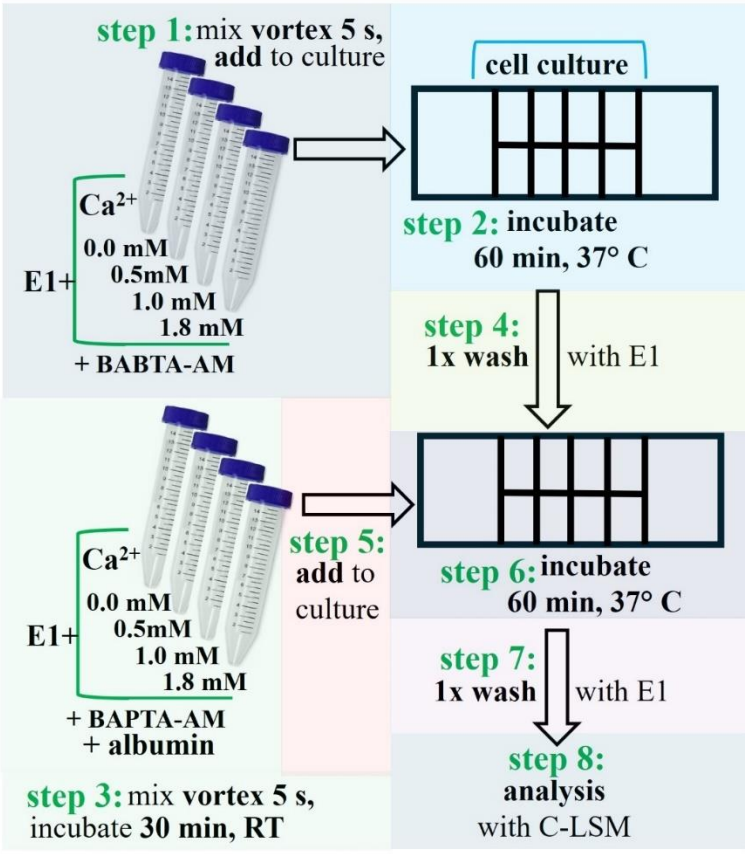

Figure 13. Experimental Design for Ca^{2+} Concentration-dependent Effects on Albumin Endocytosis.

$CaCl_2$ was dissolved in E1 buffer devoid of Ca^{2+} to prepare the desired f.c. of Ca^{2+}-containing medium adjusted with *BAPTA-AM* (10 µM, f.c.). Confluent cells were cultured in 8 well micro slide chambers and incubated for 1 h at 37° C in a 6% CO_2 incubator. Fluorescence-labelled albumin in E1 buffer-Ca^{2+}-supplemented solution was incubated for 30 min at RT allowing to bind with albumin molecules and added to the cells washed with E1 buffer. After 1 h of incubation at 37° C cells were washed with E1 buffer and were analysed using C-LSM for endocytosis.

3.5 FcRn Blocking

Three different strategies were used to interfere with FcRn signaling: siRNA electroporation, chemical transfection and *Nipocalimab* (*M281*) antibody directed against the FcRn ligand binding site (Choudhury et al., 2022).

3.5.1 Knock-down with si-RNA Technology

ADSCs derived from different donor age groups (ADSC 16, 26 years, ADSC 35, 40 years, ADSC 34, 71 years) were cultured for transfection experiments during passage 5 – 10. After enzymatic detachment and counting according to the

previously described protocol cells were used for transfection experiments according to the manufacturer's guidelines. Si-RNA duplexes (100 nM) (si-RNA against FcGRT, scrambled siRNA negative control, TYE 563TM si-RNA positive control) were used for transfection either by electroporation or INTERFERin technique.

3.5.1.1 Electroporation

ADSCs, when reached ± 90 % confluency, were collected in 50 ml Falcon tubes in culture medium (20 ml) and centrifuged for 5 min at 300 x *g*. Cells were washed with 20 ml PBS (without Ca^{2+}, Mg^{2+}) by centrifugation for 5 min at 300 x *g*. Subsequently, PBS was aspirated, and cells were resuspended in sufficient volume of Buffer R to reach $1.0x10^7$ cells/ml. Neon Transfection System (cat # MPK5000, Invitrogen) was used for electroporation according to the manufacturer's guidelines. The system was configured for pulse voltage (1400 V), pulse width (10 ms, milisecond), and pulse number (3). After electroporation cells were seeded directly to the 24 well plate on gelatin-coated cover slips containing pre-warmed culture medium and incubated for 24 - 48 h before experiments.

3.5.1.2 Chemical Transfection

ADSCs seeded into the 100 mm Petri dishes and 8 well chambers were cultivated to reach ± 50 % confluency before INTERFERin transfection. Respective si-RNA duplexes diluted in serum free medium (100 µl/well, 500 µl/Petri dish) were mixed for 10 s and spun down. INTERFERin transfection reagent (4 µl/well, 50 µl/ 100 mm Petri dishes) was added to the solution, mixed on a Vortex mixer for 10 s and spun down. The mix was incubated for 10 min at RT and added to the cells which were incubated in fresh serum-containing medium (500 µl/well, 5 ml/Petri dish). Cells were analysed after 48 h for validation and other applications.

3.5.2 Blocking with *M281*

Cells were incubated with *M281* at three different concentration (5.0, 15.0 and 25.0 µg/ml) for 1 or 2 h at 37° C to analyse for albumin, IgG internalization and Ca^{2+} oscillations according to the previously described protocols. The respective *M281* f.c. was maintained throughout all the experiments.

3.5.3 FcRn and Albumin Localization

Successful transfection was validated by fluorescence analysis of the TYE 563TM fluorescence-labelled transfection control si-RNA duplex. FcRn knock-out was validated by IHC using an antibody against FcRn (dilution 1:200) conjugated with Alexa-Fluor-488 donkey anti-rabbit (dilution 1:400) for 1 h at 37° C and analysed by C-LSM. Cells were incubated with Albumin-Alexa-594 (300 μM) for 1 h at 37° C, washed with fresh medium and analysed for albumin endocytosis efficiency. Selected regions of interest (ROI) from fluorescent images were analysed between transfected and wild type ADSCs.

3.6 Immunocytochemistry

3.6.1 Cell Fixation

Paraformaldehyde (PFA, 4%) solution was prepared by dissolving PFA in PBS, stirred at 60° C under safety hood, and pH was adjusted to 6.9 – 7.4 after cooling. The solution was filter-sterilized and stored in 4° C. Sample cells were washed with PBS to remove culture medium and sufficient PFA was added to cover the entire surface, and samples were

incubated for 30–45 min at RT. PFA was removed by washing three times with PBS.

3.6.2 Blocking

FBS (10%) solution in PBS was prepared, and aliquots were stored at 4° C for short term use. Fixed cells were incubated with FBS solution for 1 h at RT on shaker avoiding light exposure. FBS was washed off with PBS to remove unbound FBS from the sample.

3.6.3 Antibody Conjugation

Primary antibody at desired dilution factor in FBS solution was added to the blocked sample and incubated for overnight at 4° C. Unbound antibodies were washed off and incubation with respective secondary antibody was performed for 1 h at RT. For negative control, the incubation step with primary antibody was omitted. Nuclear staining was conducted with DRAQ5 or nuclear green as specified in different experiments. Cells were washed for three times to remove all staining agents from the sample.

3.6.4 Microscopy

Prepared cover slips were air dried and attached on the glass slide with Fluoromount G marked with sample identification details and stored at RT under light protection. Slides were investigated by C-LSM using Leica LSM SP2 AOBS (Leica, Wetzlar, Germany) equipped with a 40 x oil-immersion objective (numerical aperture 0.7) and analysed by the image analysis software of the confocal setup. Specific excitation/emission wave lengths setups were used for different experiments as mentioned in the respective section and protocol of image analysis was described in ***section 3.9***.

3.7 Western Blot

3.7.1 Protein Isolation

Samples were collected into a 1.5 ml microtube by cell scraper after washing with pre-warmed PBS. Samples were centrifuged for 5 min at 209 x *g* and remaining PBS was removed. A 400 µl volume per 10 cm Petri dish of freshly prepared RIPA buffer supplemented with protease inhibitor cocktail (2 µl/ml) was used as lysis solution. After homogenizing by Pellet Pestle Motor samples were kept on ice for 20 min and centrifuged with pre-chilled (+ 4° C)

centrifuge at 35,395 x *g* for 10 min. Supernatant was collected to a new sterile microtube properly marked and stored in - 80° C freezer.

3.7.2 Protein Quantification

Protein quantification was performed by Lowry assay (Lowry et al., 1951) with the aid of spectrophotometric analysis. The mix was prepared by adding reagent A, L4, dH_2O, and protein sample at 1000:100:100:10 ratio, respectively. A concentration series of protein standards was prepared with BSA. The mixed solutions were incubated for 10 min at RT, then 200 µl of L5 was added to 1000 µl of the mixed solutions and then incubated for an additional 30 min at 37° C on pre-heated thermoblock. The solutions were centrifuged for 30 min at RT, 35,395 x *g*. A 200µl aliquot of the middle portion of the final mix was transferred to a 96-well ELISA plate and absorbance measured by using Tecan Infinite m200 microplate reader at a wavelength of 578 nm.

3.7.3 Protein Separation and Transfer

Protein separation depending on molecular weight differences was performed by gel electrophoresis. Sample

protein (30 µg) was mixed with NuPAGE LDS sample buffer (2.5 µl), NuPAGE sample reducing agent (1 µl) and H_2O (Aqua B. Braun) to reach a final volume of 10 µl. Samples were incubated for 10 min at 70° C to denature and subsequently spun down by short (3 s) centrifugation (209 x *g*). Protein samples (10 µl) and Novex Sharp Pre-stained Protein standard (3 µl) were loaded into 4-12% Bis-Tris gel previously mounted in the XCell SureLock Mini-Cell electrophoresis chamber. NuPAGE Running buffer (50 ml) was mixed with H_2O (Aqua B. Braun) to reach the final volume of 1 L and subsequently added to the chamber to dip the gel up to the top and NuPAGE antioxidant (500 µl/gel) was added to the buffer. Electrophoresis was performed using PowerEase 500 at 180 V and 120 mA for 90 min.

Separated proteins were transferred to PVDF membranes (Immobilion P Transfer Membranes, 0.2 µm pore size). NuPAGE Transfer Buffer (50 ml) and methanol 100 ml were stocked up with 850 ml H_2O (Aqua B. Braun) to prepare transfer buffer (1X). 1 ml NuPAGE antioxidant was added to the transfer buffer. Precisely cut of transfer membrane was incubated with methanol for 30 s and subsequently with

transfer buffer for 3 min. Transfer sandwich was prepared by placing 3 sponges and 2 filter papers previously socked in transfer buffer on both face of the gel-membrane. The gel was placed on the cathode side and membrane on the anode side of the sandwich. Protein transfer was done at 200 mA for 2 h with the same power station, and the membrane was marked for molecular weight at specific kDa according to the protein ladder provided by the manufacturer. Subsequently membranes were washed with TBST (1x) for 5 min on a shaker.

3.7.4 Immune Staining with Antibodies

Blocking buffer was prepared with BSA (5%) dissolved in TBST (1x). Membranes were incubated with blocking buffer for 1 h on a roller mixer and incubated with primary antibodies overnight at + 4° C and with secondary antibody for 1 h in RT on shaker. Membranes were washed with TBST three times for 5 min to remove unbound proteins.

3.7.5 ECL Assay

Horseradish peroxidase (HRP) labelled secondary antibody was detected by ECL assay. This assay depends on the

reaction between HRP and ECL solution containing enhanced luminol, p-coumaric acid and stable hydrogen peroxide solution. The protein containing membrane was incubated with 1 ml ECL solution for 3 min and light signal captured by chemiluminescence imaging system using ChemiCapt 500 imaging software. The membrane was washed with TBST (1x) three times to remove ECL solution and stored at + 4° C in TBS (1x) for future experients. The saved image was analysed by ImageJ image analysis software.

3.7.6 Multiple Protein Detection

To use the same membrane for detection of multiple proteins, membranes were stripped by incubating with Restore PLUS Western Blot Stripping Buffer for 15 min. After three washing steps with TBST (1x) for 5 min the same protocol was performed as described in ***section 3.7.4*** and ***3.7.5***.

3.8 Nuclear Staining

3.8.1 DRAQ5

DRAQ5 (Cat# 4084S, Cell Signaling Technology) was dissolved in PBS (without Ca^{2+}, Mg^{2+}, sodium azide) at 1:2000 dilution. Culture medium was washed off from the cells using PBS. Dissolved DRAQ5 was added in a volume of 500 µl/well of 24 well plates to the cells and incubated for 15 min at 37° C in a 6% CO_2 incubator, and the solution was washed off for three times with PBS. Fluorogenic agent was analysed in C-LSM with 633 nm helium/neon laser. Emission was recorded at >650 nm wavelength.

3.8.2 Nuclear Green

Nuclear Green (Cat# 17540, AAT Bioquest) was provided as 5 mM stock in DMSO. Sufficient volume of diluted Nuclear Green solution (2 µM) was added to cover the cell surface and incubated for 30 min at 37° C in a 6% CO_2 incubator and washed of three times with PBS to remove extra dye from the environment. Treated cells were analysed with C-LSM at excitation/emission max: 503/610 nm.

3.9 Image Analysis

Western blot image analysis was performed using the image analysis software (ImageJ). Endocytosis and immunohistochemistry analysis were performed by capturing randomly selected spots (10 ± 2) using a confocal microscope (LEICA TCS SP 2AOBS, objective: HC XPL APO 40x/1.25-0.75) as shown in figure **(Fig. 14)**. Mean fluorescence values for each image were measured after background subtraction. Mean fluorescence of entire image (frame) is referred to as the fluorescence of selected image. Fluorescence regions close to the nucleus were selected as the region of interest (ROI, selected using an overlay mask) at desired numbers (12 ± 3) from each image, and mean fluorescence was analysed by Leica image analysis software (LAS AF Lite 3.3.0).

$$\text{Fluorescence of Image} = \frac{\Sigma\ \text{Fluorescence of ROI}}{\text{Total number of ROIs}}$$

$$\text{Fluorescence of Individual Experiment} = \frac{\Sigma\ \text{Fluorescence of Image}}{\text{Total number of Images}}$$

$$\text{Mean Fluorescence} = \frac{\Sigma \text{ Fluorescence of Individual Experiment}}{\text{Total number of Experiments}}$$

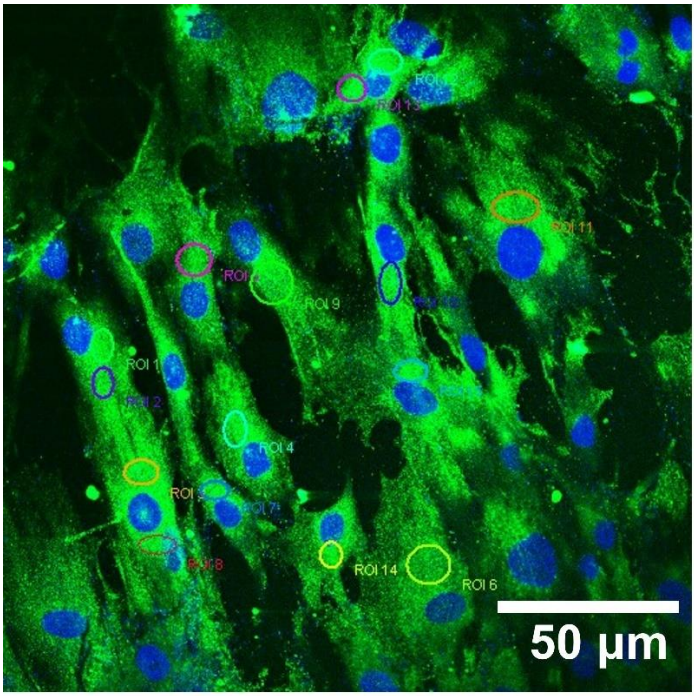

Figure 14. ROI Selection on a Representative Image from ICC Experiment. ROI selections are shown with differentially coloured circles close to the nucleus (blue pseudo-color labelled with DRAQ5 DNA dye).

3.10 Data Analysis

Data are presented as mean values (± SD) with given number of individual experiments as n (number of individual experiments). Statistical analysis was performed using Microsoft Office Excel and GraphPad InStat data analysis software. Students' *t*-test and one-way analysis of variance (ANOVA) were applied depending on the experimental setup. Significance level was estimated from p-value of <0.05, significant (presented as *), <0.001, very significant (presented as **), <0.001, extremely significant (presented as ⁂), and >0.05 considered not significant (presented as ns).

4. Results

4.1 Isolation of Visceral ADSCs

Fat tissue of visceral origin was collected from different patients (vASC2, 59 years, female, vSCf50, female, 50 years, vASC34, male, 34 years, vASCf23, female, 23 years) and processed to isolate ADSCs according to the protocol described in ***section 3.1.3***. Two cell populations with different morphologies were observed: fibroblast-shaped

cells which is typical for ADSCs, and oval cells (**Fig. 15**). The oval shape cell population decreased in ratio to the fibroblast-shaped cells (oval: fibroblast = 85:15% at day 1, 72:28 %) at day 3) (**Fig. 16**). Representative light microscopic images (**Fig. 17**) demonstrated differences in shape between visceral ADSCs and subcutaneous ADSCs. After isolation every cell line was validated for stemness with the stem cell markers, OCT 4; SOX 2; and Nanog (data not shown).

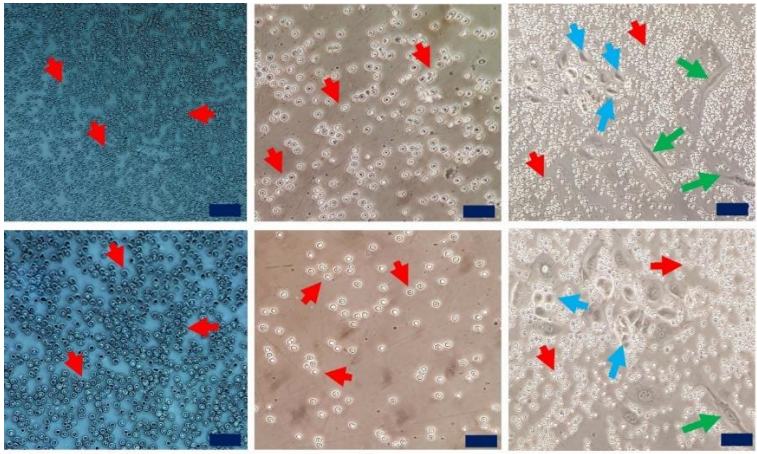

Figure 15. ADSCs obtained from human visceral fat tissues.

Approximately $4x10^4/cm^2$ cells were seeded (passage 0) on 10 cm Petri dishes containing pre-warmed CCM for incubation at 37º C in 6% CO_2 incubator and washed everyday with culture medium to remove unbound cells (e.g.

RBCs) before microscopic analysis. Phase-contrast images denoting: spherical RBCs (red arrow), ADSC monolayer adherent cells with oval (blue arrow) and fibroblast-like morphology (green arrow) at different time points after isolation (passage 0) at 10 x (upper panel) and 20 x (lower panel) magnification. Scale bar stated (100 µm) is subjected for all images.

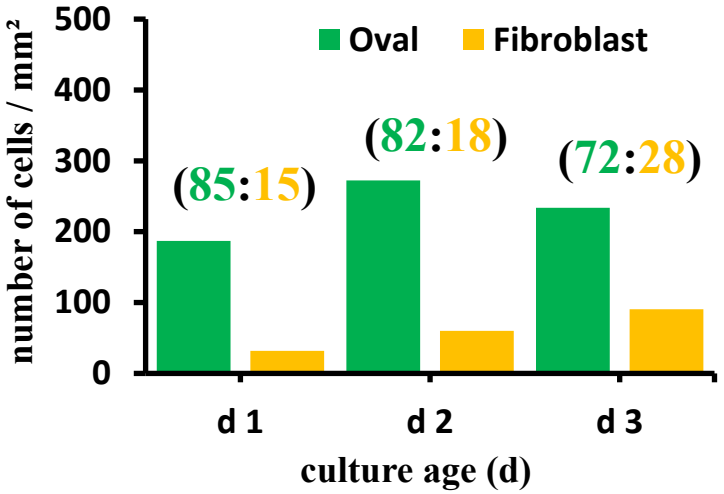

Figure 16. Number of cells/mm^2 With Oval Versus Fibroblast-like Appearance. The bar chart displays the total number of visceral ADSCs (cell/mm^2) from passage 1 and the ratio of oval cells to fibroblast-shaped cells at different days (d1 to d3).

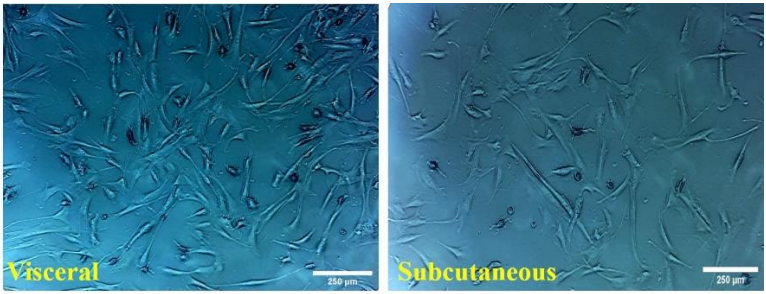

Figure 17. Comparison of ADSCs from Visceral Fat and Subcutaneous Fat.

Phase-contrast images representing ADSCs from visceral fat (passage 3) and subcutaneous fat (passage 5) origin on day 1 after isolation from female donors. Scale bar (250 µm).

4.2 ADSCs from Different Sources Investigated for Albumin Endocytosis and Ca^{2+} Oscillations

We investigated Ca^{2+} signaling as well as albumin endocytosis in ADSCs isolated from subcutaneous and visceral fat tissues following the protocol described in ***section 3.3*** and ***section 3.4***, respectively. Cell culture of subcutaneous ADSCs (passage 8) and visceral ADSCs (passage 5) from the same age group (middle: 35 – 49-year-old) were used for this experiment. Our study suggested

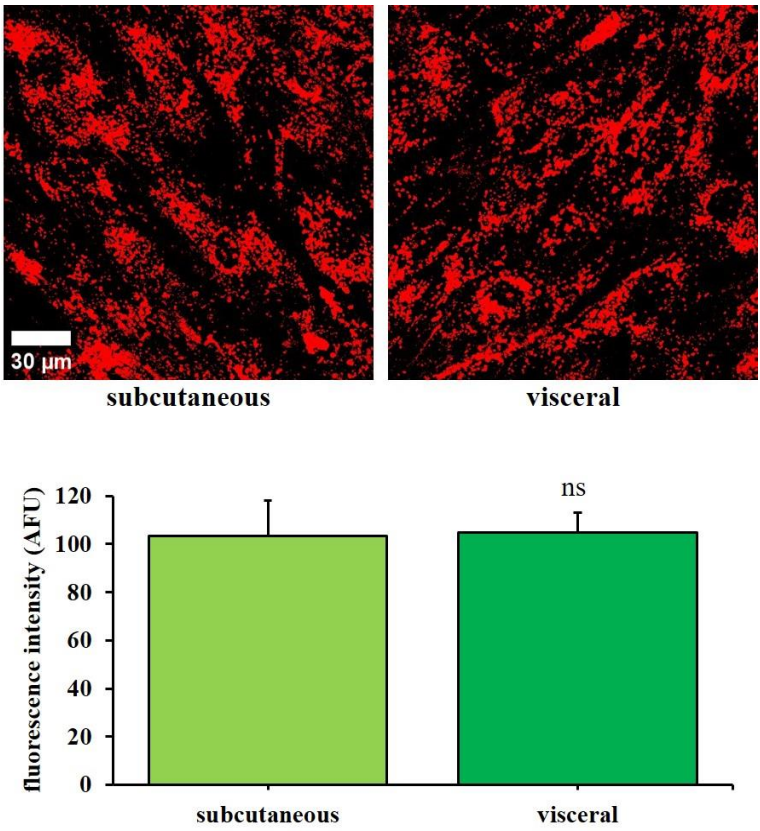

Figure 18. Comparison of Albumin Endocytosis in ADSCs from Different Origin.

Upper panel shows representative images of subcutaneous and visceral ADSCs incubated with Albumin-Alexa-594 (300 µM) for 1 h at 37° C in 6% CO_2 incubator. The bar chart represents semiquantitative analysis of cellular Alexa-594 fluorescence. Values are given as mean (± SD) of four individual experiments, data are statistically not significant, ns = >0.05. Scale bar (30 µm) subjected for both images.

comparable uptake capacity for albumin in ADSCs from both sources (**Fig. 18**). Performance of Ca^{2+} oscillations showed no significant difference in Ca^{2+} oscillation characteristics with regard to spike frequency and spike amplitude (**Fig. 19**). Since no differences in albumin uptake and Ca^{2+} spiking characteristics were observed, further experiments were conducted exclusively with ADSCs from subdermal origin.

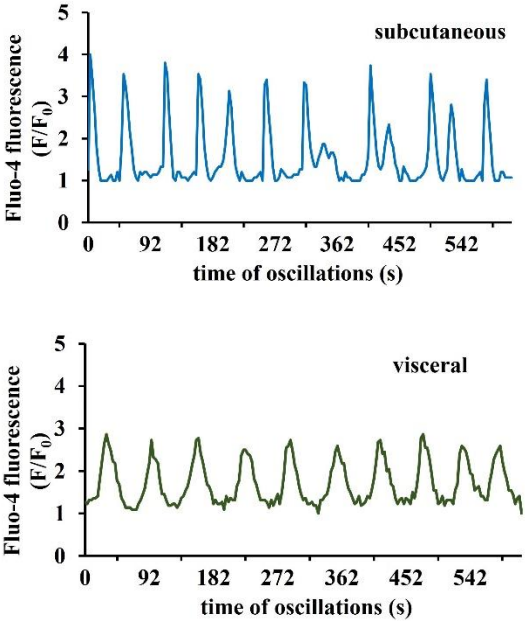

Figure 19. Representative time course of Ca^{2+} oscillations in ADSCs from Subcutaneous Fat (passage 8) and Visceral Fat (passage 5) Origin. Shown is intracellular Fluo-4 fluorescence.

4.3 Plasticity of ADSCs

ADSCs have the potential to differentiate into multiple cell lineages, including adipocytes, osteocytes (Chang et al., 2023; Shao et al., 2022), retinal cells (Huang et al., 2018; Qin et al., 2023), chondrocytes, myocytes (Yogi et al., 2021), and neurons (Masoumi et al., 2023). We tested plasticity of subcutaneous ADSCs isolated in the present study for osteogenesis and adipogenesis to validate differentiation capacity of the stem cells.

4.3.1 Osteogenesis

Subcutaneous ADSCs from donors of the middle age group (35 – 49-year-old) were treated with osteogenesis induction medium and analyzed using Alizarin Red S staining for their osteogenic potential according to the protocol described in ***section 3.2.1***. Osteocytes differentiated from ADSCs showed distinguishable difference between undifferentiated ADSCs (**Fig. 20-A**) and differentiated osteocytes (**Fig. 20-B, C, D**) tested by Alizarin red assay. Immunostaining with antibody against osteocalcin demonstrated significant difference between undifferentiated ADSCs (**Fig. 21-A**) and cells

differentiated into osteocytes (**Fig. 21-C**). Immunofluorescence assay of Alexa-fluor-488 conjugated with osteocalcin presented significantly higher fluorescence intensity for cells induced with osteogenic medium (**Fig. 21-D**).

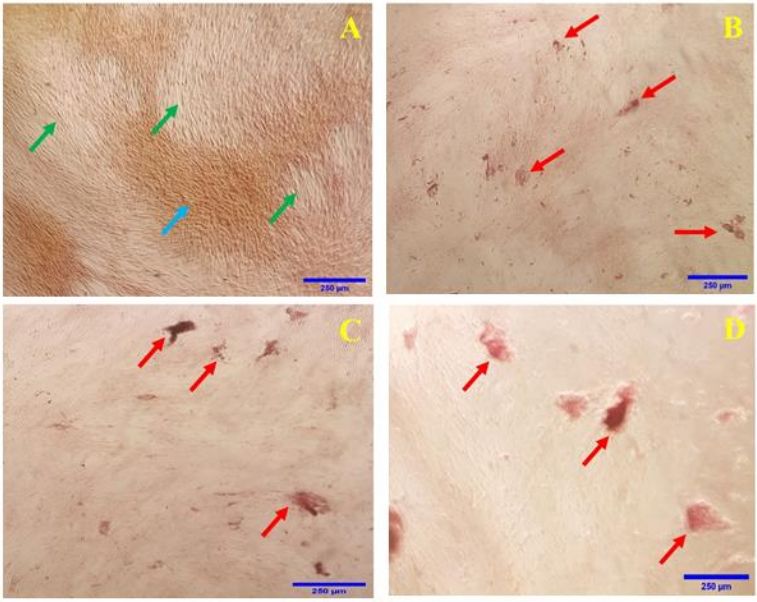

Figure 20. Osteogenic Differentiation of ADSCs Investigated with Alizarin Red S Staining.

A: ADSCs (green arrow) not induced to osteogenesis presented no Ca^{2+} deposition. Blue arrow shows staining agent not washed away properly. B-D: Ca^{2+} deposition (red arrow) observed in the osteogenic culture. Scale bar stated (250 µm) is subjected for all images.

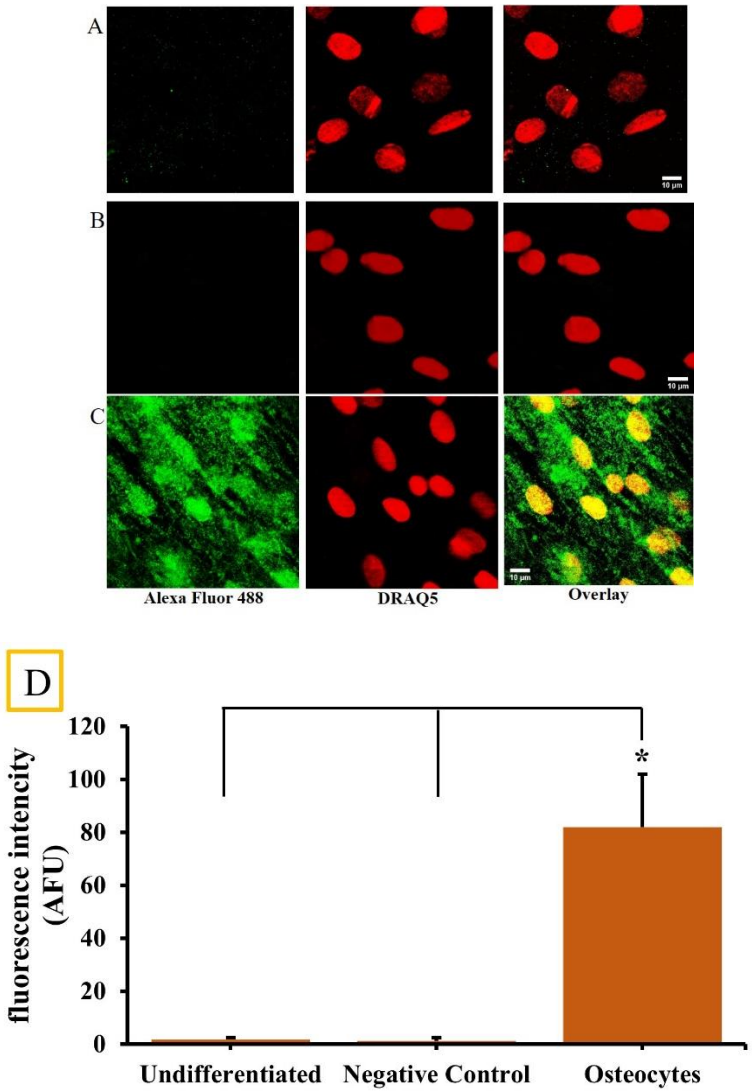

Figure 21. Osteocalcin localization in osteocytes differentiated from ADSCs …(continue next page)

Figure 21. Osteocalcin localization in osteocytes differentiated from ADSCs (cell ID: ADSC 35, 40 year-old donor).

A. Undifferentiated ADSCs (not induced for osteogenesis), and **C.** Osteocytes (after osteogenic induction of ADSCs). Cells (representative images on row **A** and **C**) were incubated overnight with an antibody directed against osteocalcin. **B.** Negative control (osteocytes) not incubated with antibody against osteocalcin. All samples were incubated with secondary antibody Alexa Fluor 488 (Donkey Anti-rabbit) (green) for 1 h at RT and incubated with nuclear stain DRAQ5 (red) for 1 h at RT. **D.** Osteocalcin expression in differently treated samples was investigated by C-LSM. Scale bar stated (10 μm) is subjected for all images.

4.3.2 Adipogenesis

Subcutaneous ADSCs from donors of three different age groups (20-34, 35-49, and 65-80-year-old patients) were treated with adipogenesis induction medium and analyzed using Oil Red-O staining for their adipogenic potential according to the protocol described in ***section 3.2.2***. The data of the present study demonstrated that the adipogenic potential of ADSCs decreased with advanced patient age which was significant between 20-34 and 65–80-year-old patients. **Fig. 22** shows Oil-red stained lipid bodies recorded C-LSM fluorescence images on the upper panel and with phase contrast images on the lower panel. The oil-red-

positive cell area increased from day 6 to day 12 of cell culture.

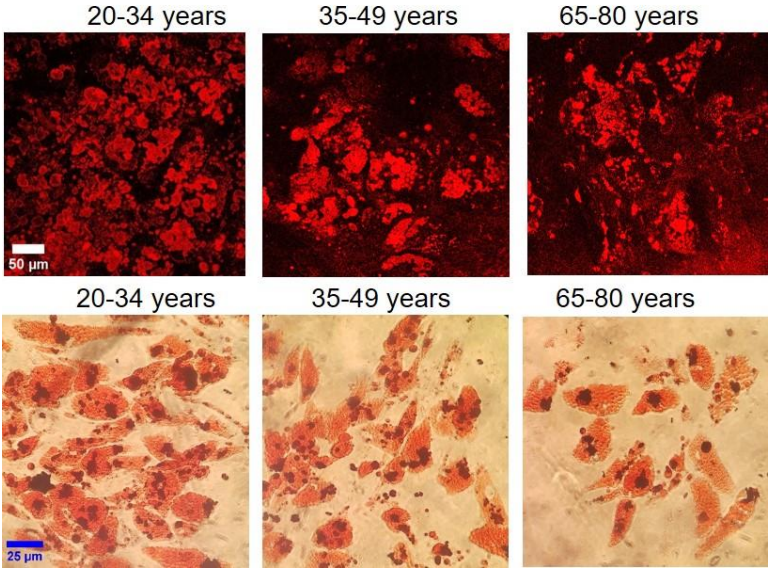

Figure 22. Adipogenic Differentiation Induced in ADSCs of Different Age Groups.

Representative Oil Red O-stained cell cultures at day 12 as evaluated by CLSM fluorescence imaging (upper panel, scale bar: 50 µm) and phase-contrast images (lower panel, scale bar: 25 µm).

4.4 Ca^{2+} Signaling in ADSCs

We investigated Ca^{2+} oscillations using Fluo-4, AM according to the method stated in ***section 3.3***. DMSO (1

µl/ml) was used as solvent for most of the blockers of Ca^{2+} channels and endocytosis pathways were tested for their effects on spontaneous Ca^{2+} oscillations in ADSCs. Ca^{2+} oscillations were observed for ± 10 min and DMSO added to investigate effects of solvent in oscillation characteristics. In our experiments DMSO treatment had no detectable effect on Ca^{2+} oscillations (**Fig. 23**).

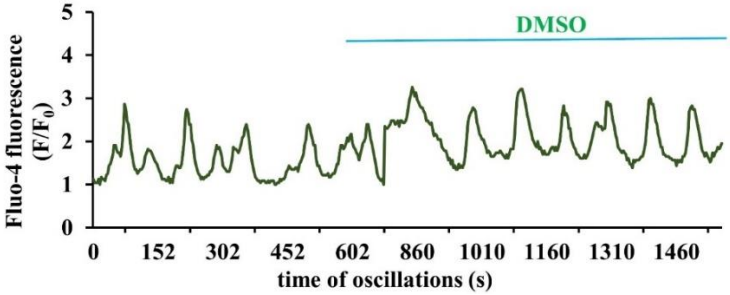

Figure 23. Effect of DMSO on Ca^{2+} Oscillations in Representative ADSCs Derived from Subcutaneous Adipose Tissue. The time point of DMSO (1 µl/ml)-conditioned medium is indicated with bar.

4.4.1 Albumin, FcRn-stimulating antibody, IgG and FBS Initiated Ca^{2+} Oscillations in ADSCs

Our data demonstrated that Ca^{2+} oscillations were absent in ADSCs incubated with serum free culture medium (**Fig. 24-**

A), whereas Ca^{2+} oscillations were apparent in serum-containing cell culture medium during the entire time course of the experiment (**Fig. 24-B**). To validate the hypothesis that serum albumin was the driver of Ca^{2+} oscillations we incubated cells in serum-free medium and added either foetal bovine serum (FBS) (10%) (**Fig. 24-F**) or albumin (fraction V, bovine origin, 0.05%) (**Fig. 24-C**). Under these experimental conditions Ca^{2+} oscillations were readily induced, thus supporting the notion that albumin is inducing Ca^{2+} oscillations in ADSCs. Since albumin and IgG uptake in the cells can be mediated by FcRn we incubated ADSCs in serum-free culture medium with either a stimulating antibody directed against FcRn (1µg/ml) (**Fig. 24-D**) or with IgG (1 µg/ml) (**Fig. 24-E**) which resulted in induction of Ca^{2+} oscillations, indicating that FcRn-mediated uptake of albumin and presumably IgG may drive Ca^{2+} oscillations in ADSCs.

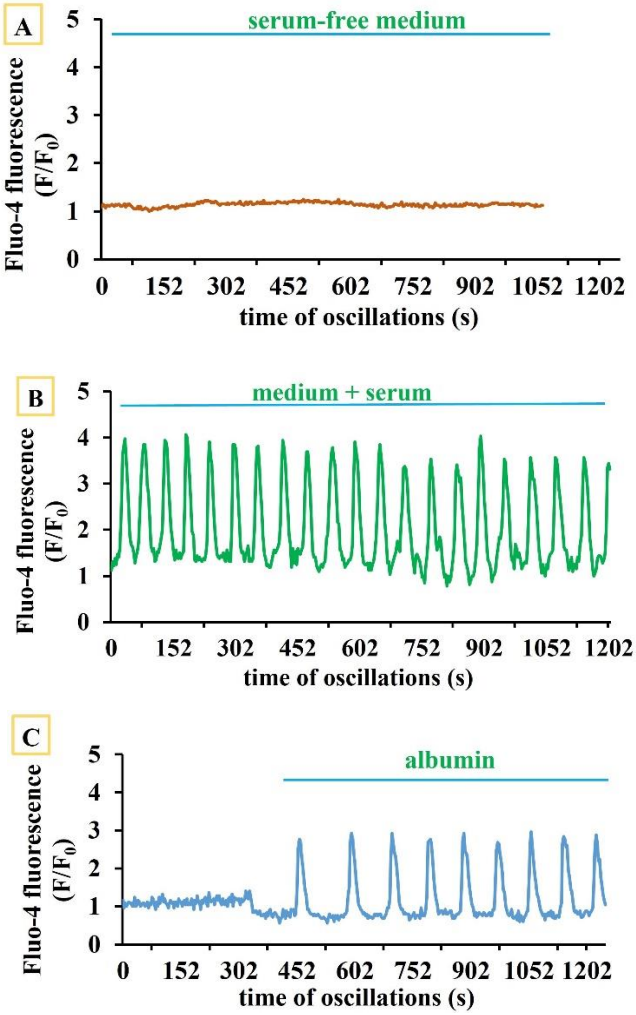

Figure 24. Induction of Ca^{2+} oscillations in ADSCs by Albumin, hFcRn, hIgG and FBS… (continues next page)

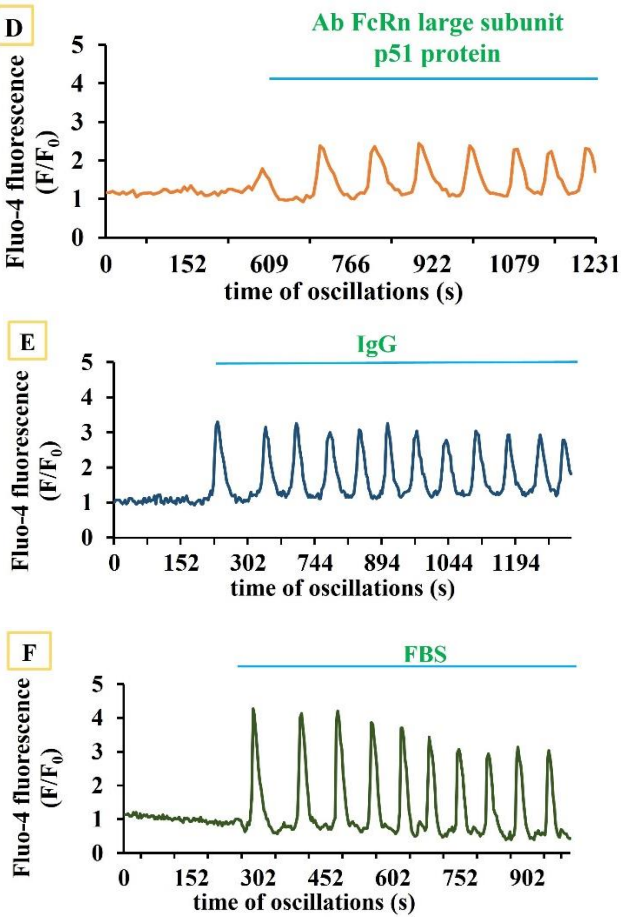

Figure 24. Induction of Ca^{2+} oscillations in ADSCs by Albumin, hFcRn, hIgG and FBS.

Shown are representative traces of Ca^{2+} oscillations in individual cells incubated in **A:** serum-free growth medium, **B:** CCM, **C:** albumin (0.05%), **D:** antibody against hFcRn large subunit p51 protein (1µg/ml), **E:** hIgG (1µg/ml) **F:** FBS (10%).

4.4.3 Termination of Ca^{2+} Oscillations by Ca^{2+} Channel Modulators

To investigate the source of Ca^{2+} driving Ca^{2+} oscillations in ADSCs the effect of the Ca^{2+} release inhibitor *BAPTA-AM*, the store operated Ca^{2+} entry (SOCE) inhibitor *SKF-96365* hydrochloride and the CaSR inhibitor *NPS-2143* were assessed.

Our data demonstrated that *BAPTA* (20 μM), *SKF-96365* (4 μM) and *NPS-2143* (5 μM) inhibited Ca^{2+} oscillations, indicating that Ca^{2+} is perceived by CaSR at the outer membrane, induces Ca^{2+} release from intracellular stores and initiates Ca^{2+} entry by store-operated Ca^{2+} channels.

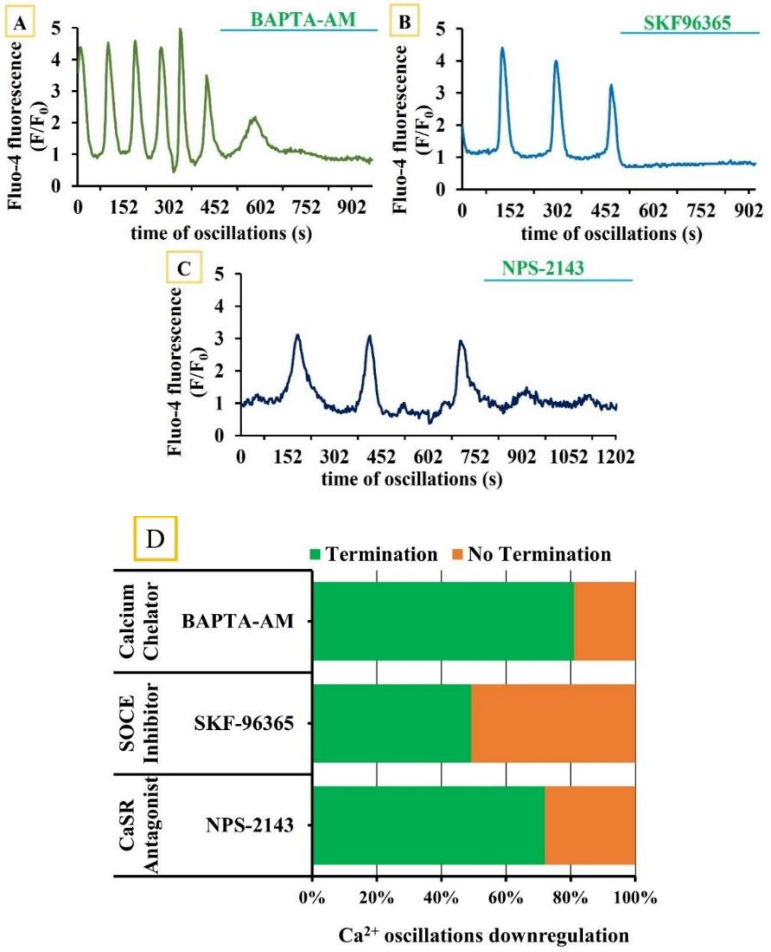

Figure 25. Inhibition of Ca^{2+} Oscillations in ADSCs Upon Interference With Ca^{2+} Signaling. **A.** Cells treated with *BAPTA-AM* (20 μM), **B.** Cells treated with *SKF-96365* (4 μM), **C.** Cells treated with *NPS-2143* (5 μM). **D.** The bar chart presenting percentages of total active cells in which Ca^{2+} oscillations were terminated under the experimental regimen. At least three experiments were performed for each group, and 50 (±) cells selected for each experiment.

4.4.4 Inhibition of Ca^{2+} Oscillations in ADSCs by Endocytosis Inhibitors

According to the working hypothesis of the present study Ca^{2+} oscillations in ADSCs are regulating albumin uptake in ADSCs. To validate this assumption, we investigated the effects of some molecule inhibitors of distinct endocytosis pathways on Ca^{2+} oscillations according to the protocol described in ***section 3.3***. Respective inhibitors were added after observing Ca^{2+} oscillations in serum-containing cell culture medium for ± 5 min, and inhibitor effects were recorded for about 10 min. It was demonstrated that blockers of different endocytosis pathways, namely CDE, macropinocytosis and CME terminated Ca^{2+} oscillations at a different rate. Incubation with the CME pathway blockers (*Dyngo-4a* and *CPZ*), the CDE pathway blockers (*Gen* and *Nyn*) and the macropinocytosis blockers (*Imp*, *Won*, *EIPA* and *CD*) terminated Ca^{2+} oscillations (**Fig. 26-A-H**). The efficiency of Ca^{2+} oscillation inhibition was different between the applied agents (**Fig. 27**). *Dyngo-4a* (10 µM), *CPZ* (10 µM) downregulated Ca^{2+} oscillations by about 21% and 71% respectively. 36%, 58%, 78%, 39% of Ca^{2+} oscillations were inhibited by *Imp* (10 µM), *Won* (10 µM), *EIPA* (50 µM), and *CD* (20 µM) respectively. *Nyn* (10 µM)

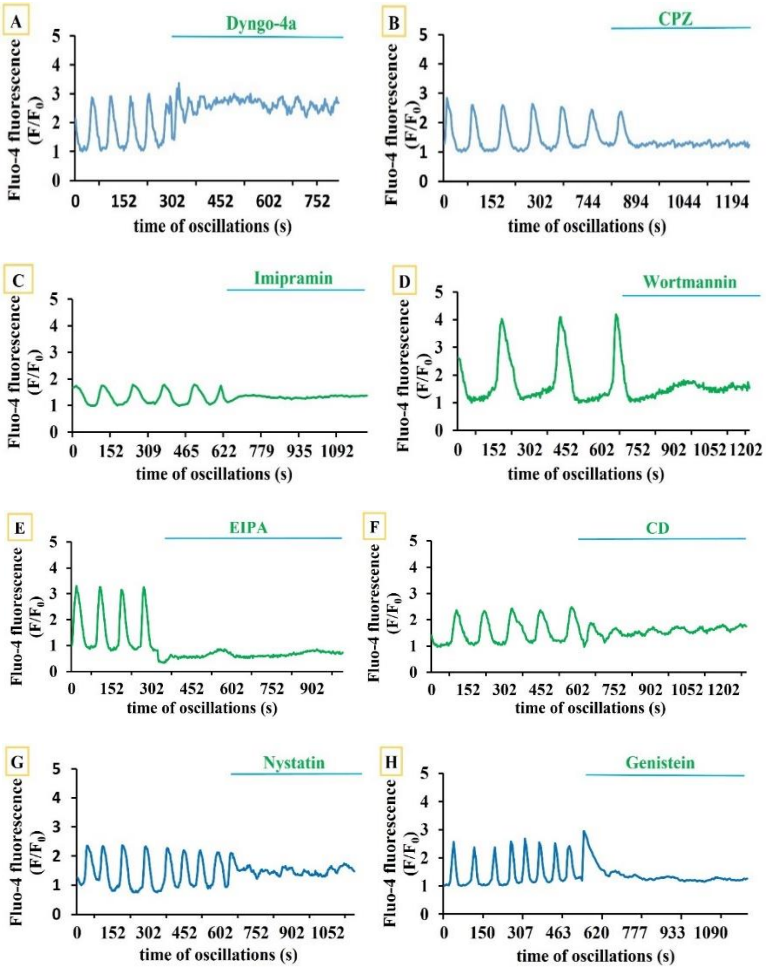

Figure 26. Effect of Different Endocytosis Inhibitors on Ca^{2+} Oscillations in Subcutaneous ADSCs From Middle-aged (35-49 year) Donors.Subcutaneous ADSCs were incubated with CCM for a few min to observe Ca^{2+} oscillations and treated with inhibitors of endocytotic pathways. Upper panels (A-H) representative traces of Ca^{2+} oscillations in ADSCs treated with endocytotic blockers. Ca^{2+} oscillations were abolished by the CME pathway inhibitors (*Dyngo-4a*

(10 µM) (**A**), *CPZ* (10 µM) (**B**), the macropinocytosis inhibitors (*Imp*, 10 µM (**C**), *Won*, 10 µM (**D**), *EIPA* (50 µM) (**E**), *CD* (20 µM) (**F**) and the CDE pathway blockers (*Nyn*, 10 µM) (**G**), *Gen*, 25 µM (**H**).

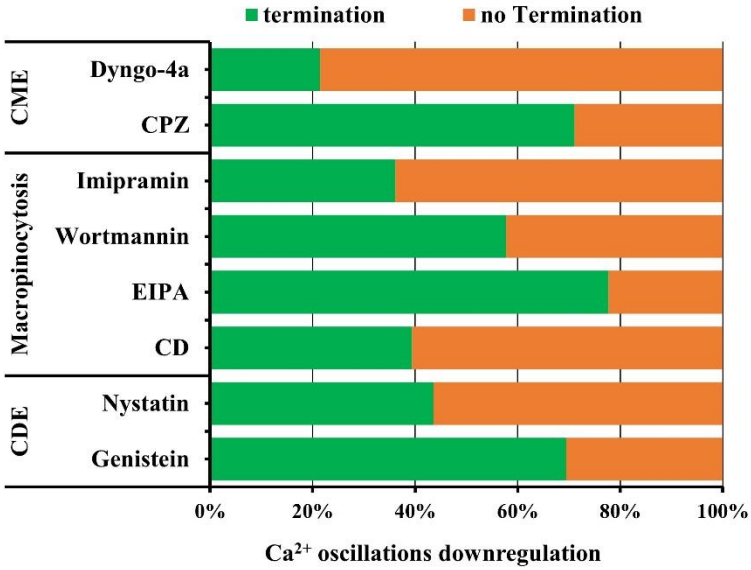

Figure 27. Efficiency of Different Endocytosis Inhibitors on the Termination of Ca^{2+} Oscillations. The bar chart presents the percentage of cells with inhibited Ca^{2+} oscillations upon treatment with blockers targeting different endocytosis pathways. Each data presented are mean (± SD) from at least three experiments conducted for each group, and 50 (±) of total active cells selected per experiment.

and *Gen* (25 µM) inhibited Ca^{2+} oscillations by approximately 44 and 69%, respectively.

4.5 Albumin Endocytosis in ADSCs

Our experiments demonstrated that inhibition of Ca^{2+} oscillations was achieved by inhibitors of endocytotic pathways, suggesting that Ca^{2+} signals may orchestrate albumin uptake in ADSCs. Were therefore performed experiments to characterize endocytosis pathways for albumin in ADSCs. Albumin endocytosis was investigated according to the protocol described in ***section 4.4***. We investigated effect of stress (13 oscillations per min, 7º rocking angle, 50/60 Hz on Stuart See-Saw Rocker, SSM4) at different incubation time (0.5, 1, 2, 4, 5 and 6 h) for Albumin-Alexa-594 (300 µM) endocytosis. Our data suggested low albumin uptake in cells incubated for 0.5 h in both stress and without stress conditions, and significantly higher albumin uptake was accomplished in stress-

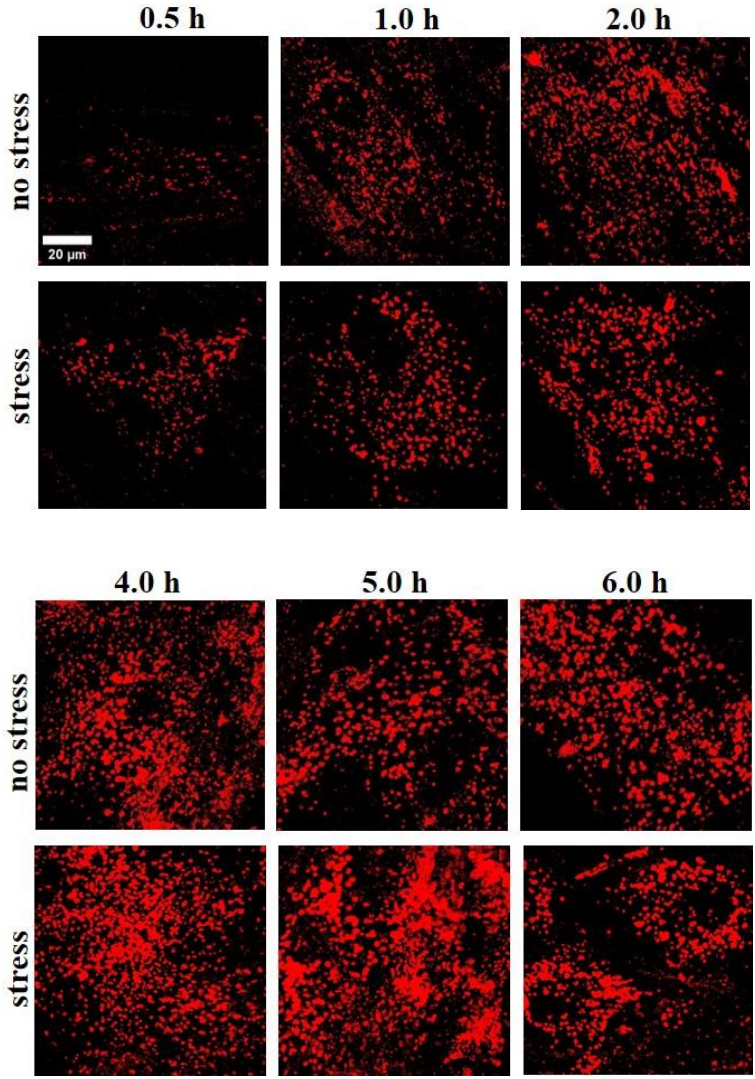

Figure 28. Albumin Endocytosis Perforance of ADSCs Incubated in Different Culture Conditions… (continues next page)

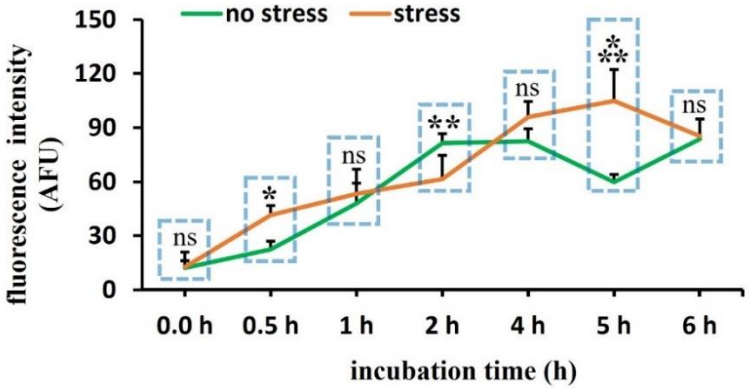

Figure 28. Albumin Endocytosis Performance of ADSCs Incubated in Different Culture Conditions. Representative C-LSM images demonstrate albumin endocytosis in ADSCs with stress and without stress condition. Scale bar (20 µm) is subjected for all images. Each data points represents mean (± SD) of four individual experiments. *p= <0.05, **p= <0.01, ⁂p= <0.001 and ns = not significant (p= >0.05).

conditioned ADSCs compared to the cells without stress after 2 h incubation. However, ADSCs incubated for 1 h presented comparable albumin endocytosis in stress and without stress condition. Hence, we consider 1 h incubation time for albumin endocytosis as standard for our intervention experiment with endocytosis blockers to reduce stress condition and excess time from the experimental setup.

4.5.1 Characterization of Albumin Uptake Pathways in ADSCs

As noted in ***section 1.6*** albumin endocytosis has been described in many studies to be diverse dependent on the investigated cell types, and many include several pathways in individual cells. Since endocytosis pathways in ADSCs are not sufficiently investigated, we assessed albumin endocytosis in ADSCs using potent inhibitors of major routes namely, macropinocytosis, CDE and CME pathways.

4.5.1.1 Macropinocytosis Blockers

The vast majority of animal cells utilize macropinocytosis (clathrin-independent) pathways for cargo (e.g. growth factors) intake which activate cell surface receptors (e.g. K-RAS-dependent macropinocytosis in lung and pancreatic cells (Sutton et al., 2022) to initiate the process.

4.5.1.1.1 Macropinocytosis Inhibition via Disrupting Actin De/polymerization

CD is a potent inhibitor of actin polymerization and depolymerization in living cells (Lambert et al., 2023). *CD* (50 mM, s.c.)-conditioned CCM was prepared to reach 10 μM and 20 μM f.c.. Cells were pre-incubated with CD-containing medium for 1 h in 6% CO_2 incubator at 37° C and

then another h with fluorescence-labelled albumin (Albumin-Alexa-594, 300 µM) in respective blocker-conditioned CCM. After washing with PBS (without Mg^{2+}, Ca^{2+}) cells were investigated and analysed using C-LSM. For individual experiment 10 ± 2 images were analysed. Our study suggested significant dose-dependent reduction of albumin endocytosis in ADSCs upon interfering with *CD* at a concentration of 10 and 20 µM (**Fig. 29**), indicating that actin polymerization plays crucial role in macropinocytic albumin uptake.

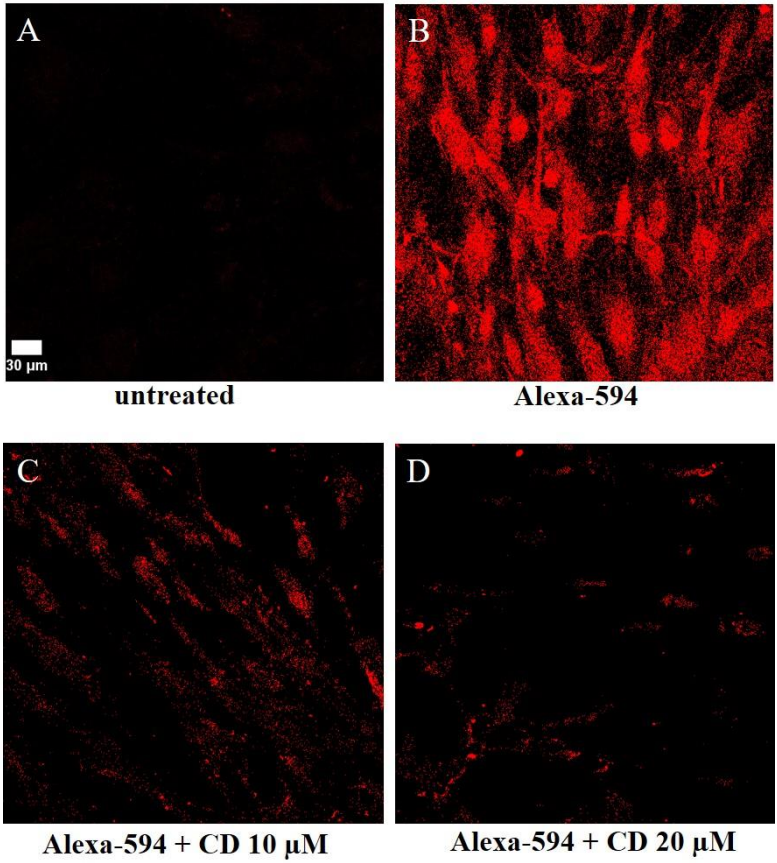

Figure 29. Effect of the Macropinocytosis Inhibitor *CD* on Albumin Uptake in ADSCs. **A:** Untreated ADSCs, **B:** Positive Control, cells incubated with Albumin-Alexa-594 (300 µM) for 1 h without blocker, **C:** Cells incubated with *CD* (10 µM) for 1 h and then with *CD* (10 µM) and Albumin-Alexa-594 (300 µM) for 1 h, **D:** Cells incubated with *CD* (20 µM) for 1 h and then with *CD* (20 µM) and Albumin-Alexa-594 (300 µM) for 1 h. Scale bar stated (30 µm) is subjected for all images.

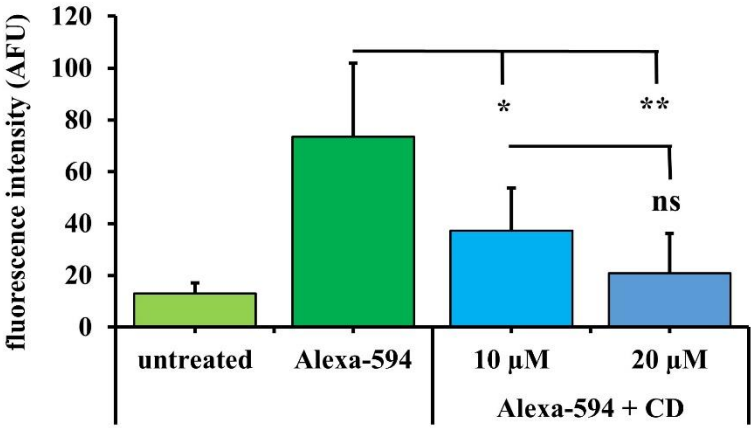

Figure 30. Semiquantitative Analysis of Intracellular Albumin upon *CD* Treatment. The bar chart presents differences in Alexa-594 fluorescence. Values are given as mean (± SD) of 5 individual experiments. (*p= <0.05, **p= <0.01)

4.5.1.1.2 Macropinocytosis Inhibition by Interference with NHE

EIPA inhibits macropinocytosis via interfering NHE (Na^+/H^+ exchanger) PM transport proteins that catalyse the electroneutral exchange of intracellular H^+ for extracellular Na^+ ions (Rennick et al., 2021). In the present investigation, *EIPA* (10 mM, s.c.) was added with CCM to reach 50 µM f.c. to intervene PM transport proteins. Cells were pre-incubated with *EIPA*-conditioned culture medium for 1 h and subsequently incubated at 6% CO_2 (37º C) in the incubator

for 1 h with Albumin-Alexa-594 (300 µM) added with *EIPA*-conditioned culture medium. Cells were investigated after washing with PBS (without Mg^{2+} and Ca^{2+}) and Alexa-594 fluorescence was analysed using C-LSM. Our data demonstrated that ADSCs treated with *EIPA* led to significant downregulation of albumin uptake compared to the untreated cells (**Fig. 32**).

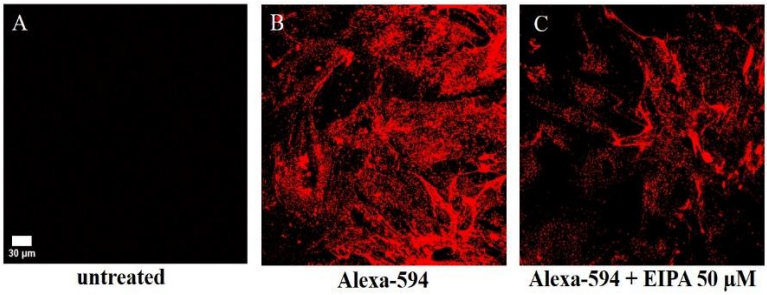

Figure 31. *EIPA* Effect on Albumin Uptake Inhibition via NHE Protein. Representative images are shown here. **A:** Untreated ADSCs, **B:** Positive control, ADSCs treated with Albumin-Alexa-594 (300 µM), **C:** ADSCs pre-incubated with *EIPA* (50 µM)-conditioned medium for 1 h and subsequently *EIPA* (50 µM) with Albumin-Alexa-594 (300 µM) for 1 h. Scale bar stated (30 µm) subjected for all images.

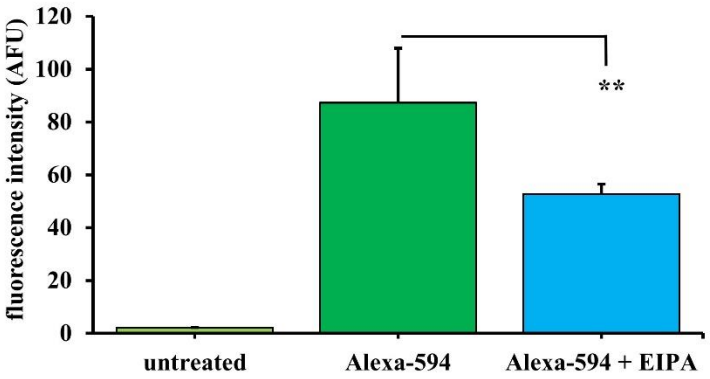

Figure 32. Semiquantitative Analysis of Intracellular Albumin upon *EIPA* Treatment. The bar chart presents differences in Alexa-594 fluorescence in different experimental groups. **p = <0.01, n = 4 individual experiments.

4.5.1.1.3 Macropinocytosis Inhibition by Arresting Ruffle Emergence on PM

Initiation of PM ruffle formation at the early step of macropinocytosis is significantly terminated by *Imp* without interfering NHE protein activity which makes it distinct from the pathway employed by *EIPA* in bone marrow-derived dendritic cells (Lin et al., 2018).

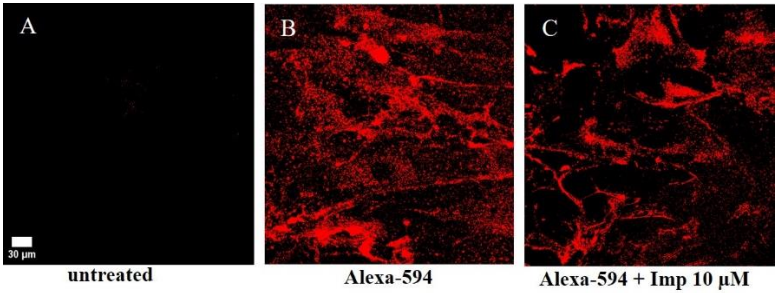

Figure 33. Effect of Imipramine on Albumin Endocytosis in ADSCs. **A:** Untreated ADSCs, **B:** Positive control, ADSCs treated with Albumin-Alexa-594 (300 µM), **C:** ADSCs incubated with *Imp* (10 µM) for 1 h and *Imp* (10 µM) with Albumin-Alexa-594 (300 µM) for 1 h. Scale bar stated (30 µm) subjected for all images.

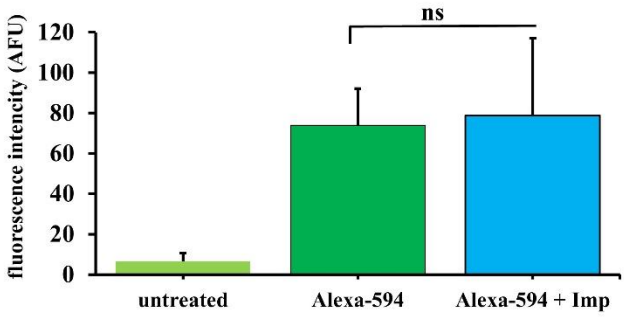

Figure 34. Semiquantitative Analysis of Intracellular Albumin upon *Imp* Treatment. The bar chart presents comparable differences in Alexa-594 fluorescence in *Imp*-treated ADSCs with untreated ADSCs. ns = not statistically significant (p = >0.05), data presented as mean of 9 individual experiments.

To investigate albumin uptake pathway in ADSCs, cells were preincubated in *Imp* (10 µM, f.c.)-conditioned culture medium for 1 h and subsequently incubated with *Imp*-conditioned medium supplemented with fluorescence-labelled albumin (300 µM) for 1 h, at 37º C in 6% CO_2 incubator. After washing with PBS, cells were analysed with C-LSM to determine albumin endocytosis inhibition by *Imp*. Our data suggested no significant downregulation of albumin endocytosis in *Imp*-treated ADSCs (**Fig. 34**).

4.5.1.1.4 Macropinocytosis Inhibition by *Won*-mediated Interference with PI3-kinase

Phosphatidylinositol 3-kinase (PI3k) is responsible for the closure of macropinosomes and phagosomes facilitating internalization of large cargo into the cells (Araki et al., 1996). In this segment of our study, we tested *Won* as a PI3k antagonist to explore macropinocytosis inhibition of albumin endocytosis in ADSCs. *Won* (10 mM in DMSO) was dissolved in cell culture medium to reach 20 µM f.c., and was used to incubate ADSCs for 37º C for 1 h at 37º C. Subsequently, cells were washed once with PBS and incubated for 1 h in fluorescence labelled albumin (300 µM) and *Won*-conditioned medium. After a washing step cells

were analysed for difference in Alexa-594 fluorescence on C-LSM. Our data suggested that PI3k intereference by *Won* significantly downregulated albumin endocytosis in ADSCs.

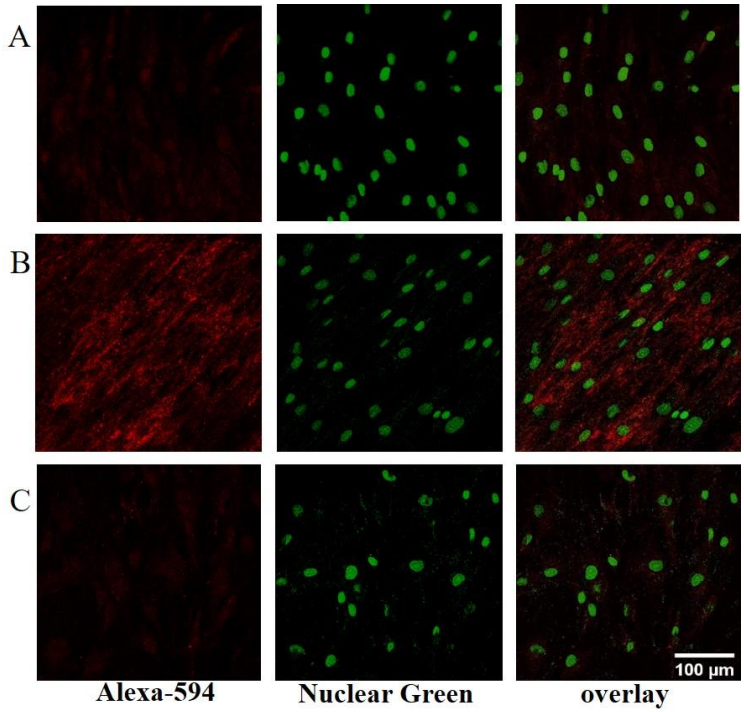

Figure 35. Albumin Uptake Inhibition in ADSCs by *Won*-mediated Interference of Macropinocytosis Pathway. **A:** Untreated ADSCs, **B:** Positive control, ADSCs treated with Albumin-Alexa-594 (300 µM), **C:** ADSCs incubated with *Won* (20 µM) for 1 h and *Won* (20 µM) with Albumin-Alexa-594 (300 µM) for 1 h. Scale bar stated (100 µm) subjected for all images.

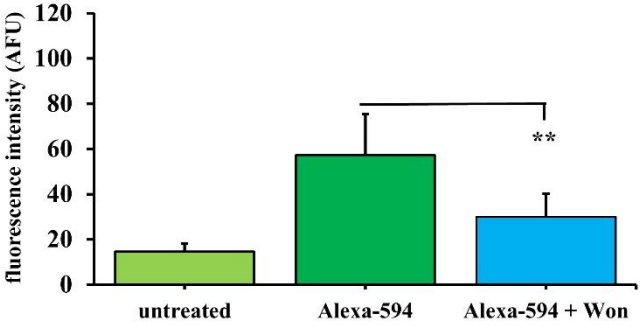

Figure 36. Semiquantitative Analysis of Intracellular Albumin upon *Won* Treatment. The bar chart presents Alexa-594 fluorescence in different experimental groups of ADSCs. **p = <0.01, data presented as mean (± SD) values of 9 individual experiments.

4.5.1.1.5 Macropinocytosis Inhibition by *MBQ-167*-mediated Blocking of Actin Polymerization

Rho, Rac, Cdc 42 GTPases activate actin polymerisation to drive macropinosomes (Song et al., 2020) which were reported to be inhibited by *MBQ-167* in myeloid lineage derived cells (Palam et al., 2023). In this study, we preincubated ADSCs with *MBQ-167* (10 µM and 20 µM) containing CCM for 1 h and subsequently with fluorescence-labelled albumin (300 µM) and *MBQ-167* (respective doses)-conditioned medium for 1 h. Samples were analysed for Alexa-594 fluorescence using C-LSM. Our data showed

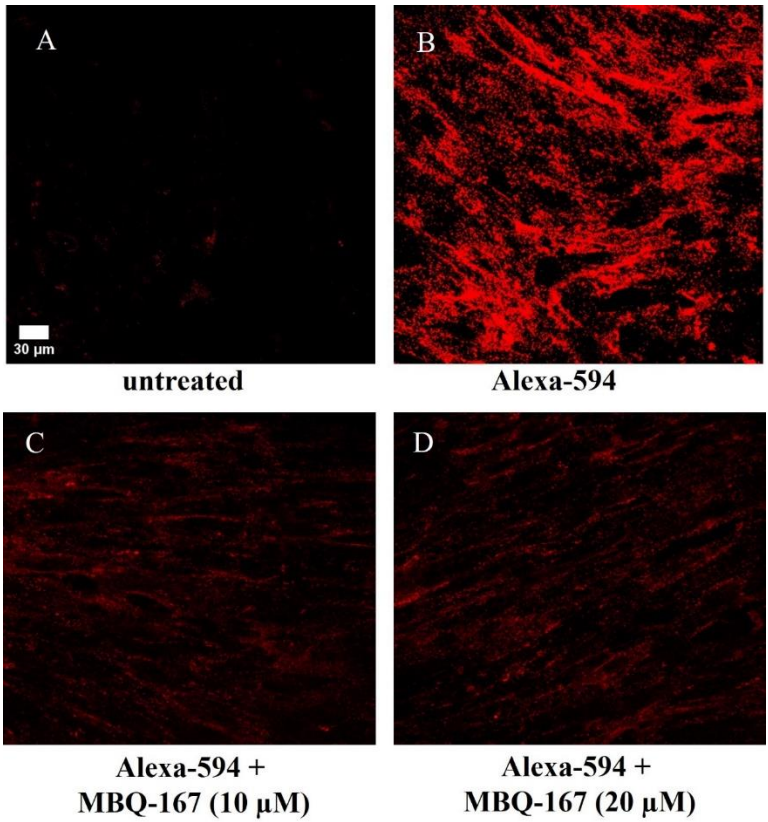

Figure 37. Inhibition of Albumin Internalization by *MBQ-167* in ADSCs. **A:** Untreated ADSCs, **B:** Vehicle (ADSCs treated with *MBQ-167*, 20 µM), **C:** Positive control, ADSCs incubated with Albumin-Alexa-594 (300 µM) for 1 h without *MBQ-167*, **D:** ADSCs incubated with *MBQ-167* (10 µM) for 1 h and subsequently with *MBQ-167* (10 µM) + Albumin-Alexa-594 (300 µM) for 1 h, **E:** ADSCs incubated with *MBQ-167* (20 µM) for 1 h and subsequently with *MBQ-167* (20 µM) and Albumin-Alexa-594 (300 µM) for 1 h. Scale bar stated (30 µm) is subjected for all images.

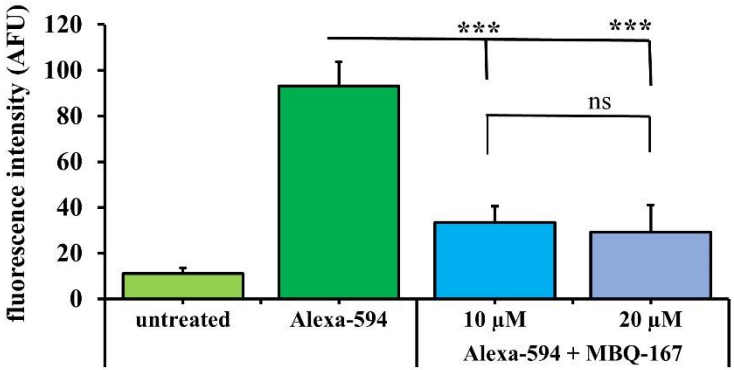

Figure 38. Semiquantitative Analysis of Intracellular Albumin Upon Treatment With *MBQ-167*. The bar chart is presenting Alexa-594 fluorescence differences in individual treatment groups. Each data point represents mean (± SD) of 6 individual experiments. ⁂p= <0.001, ns = not significant (p = >0.05).

that *MBQ-167* significantly downregulated albumin uptake in ADSCs, however no dose-dependent activity was observed for the investigated concentrations (**Fig. 37** and **38**).

4.5.1.2 Caveolae-dependent Pathway Inhibitors

Skin fibroblasts, endothelial cells, epithelial cells, podocytes were reported to involve CDE (clathrin-independent)

pathways via caveolae and cavin protein family for albumin endocytosis (Dobrinskikh et al., 2014; Razzak, 2014) and astrocytes via megalin, caveolin and cavin (Bento-Abreu et al., 2009). In this part of the study, the CDE pathway is investigated using notable blockers (*Gen*, *Nyn* and *Noco*) mentioned in ***section 3.4.2.2*** for their effects on albumin endocytosis via CDE in subcutaneous ADSCs.

4.5.1.2.1 Blocking Tyrosine Kinase Activity Decreased Albumin Uptake in ADSCs

Gen is an inhibitor of cell surface receptor tyrosine kinase that interferes with the CDE pathway (Rennick et al., 2021). In this segment of the present study, we investigated *Gen* (25 μM) effect on albumin endocytosis in ADSCs. ADSCs were preincubated in *Gen*-conditioned medium for 1 h, subsequently in Albumin-Alexa-594 (300 μM) containing *Gen*-conditioned medium for 1 h in 37º C. Cells were washed with PBS and analysed for Alexa-594 fluorescence using C-LSM. Our study suggested significant reduction in albumin uptake in ADSCs after incubation with *Gen* (**Fig. 39** and **40**), indicating albumin endocytosis is associated with the tyrosine kinase pathway.

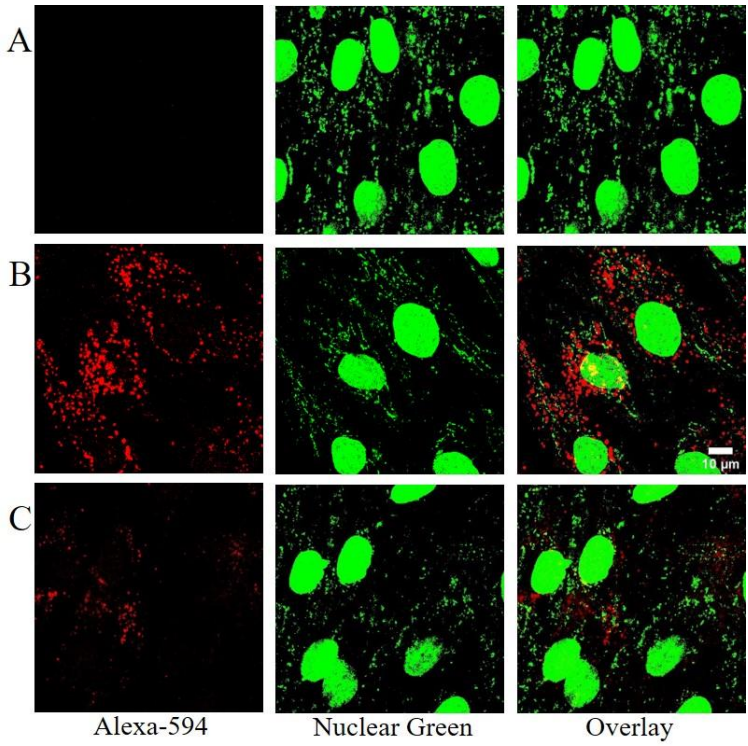

Figure 39. *Gen*-mediated Interference of Albumin Endocytosis in ADSCs. **A:** Untreated ADSCs, **B:** Positive control, ADSCs incubated with Albumin-Alexa-594 (300 µM) for 1 h without blocker, **C:** ADSCs incubated with *Gen* (25 µM) for 1 h and then with *Gen* (25 µM) + Albumin-Alexa-594 (300 µM) for 1 h. Samples were incubated with Nuclear Green (5 µM) (green) for 30 min for nuclear staining. Scale bar stated (10 µm) subjected for all images.

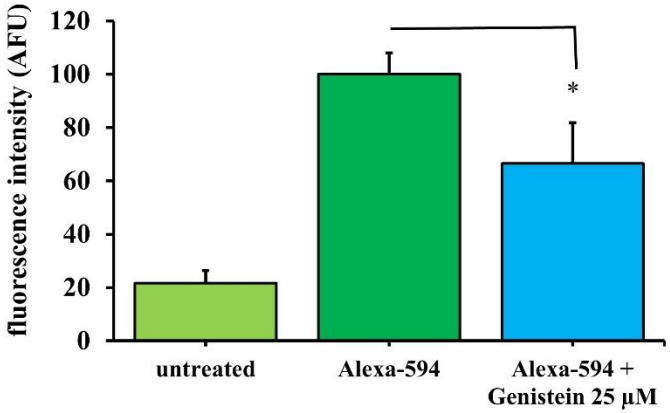

Figure 40. Semiquantitative Analysis of Intracellular Albumin Upon Treatment With *Gen*. The bar chart presents differences of Alexa-594 fluorescence in untreated and *Gen*-treated ADSCs. Each data point represents mean (± SD) of 4 individual experiments. (*p = <0.05)

4.5.1.2.2 Targeting Lipid Rafts by *Nyn* Downregulates Albumin Internalization

Caveolae are invaginations of lipid rafts which are sterol- and sphingolipid enriched microdomains. *Nyn* prevents aggregation and sequesters lipid rafts thereby inhibiting caveolae dependent endocytosis in hepatocytes and hepatic stellate cells (Rennick et al., 2021). In this segment of our study, we investigated the effect of *Nyn* (10 µM) on albumin trafficking into ADSCs using fluorescence labelled albumin and analysed on C-LSM. Our data suggested significant

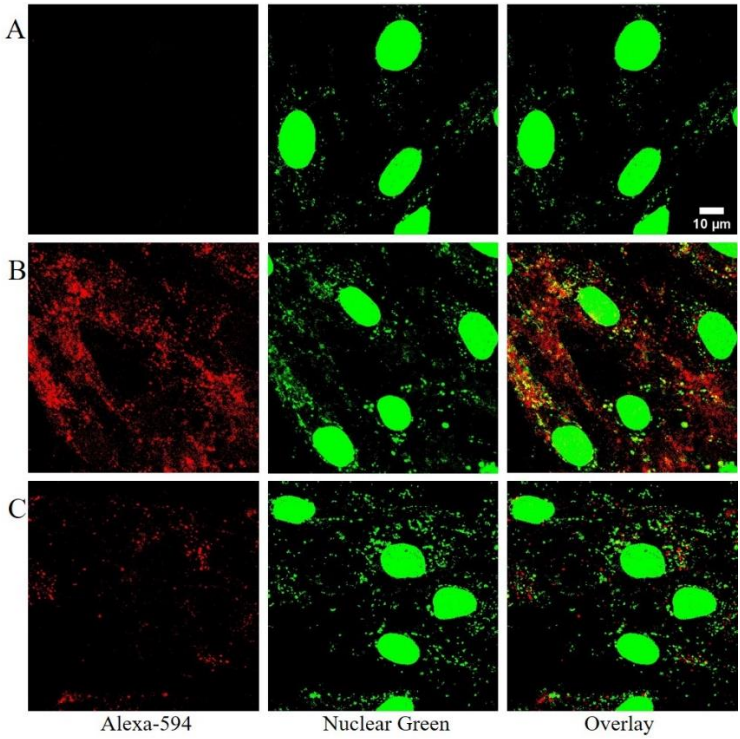

Figure 41. Albumin Uptake Inhibition in ADSCs Via Sequestering Lipid Raft by *Nyn*. Shown are representative images from C-LSM microscopy of different experimental groups: **A.** Untreated ADSCs, **B.** Positive control, ADSCs incubated in Albumin-Alexa-594 (300 µM)-conditioned medium for 1 h, **C.** ADSCs incubated in *Nyn* (10 µM) -conditioned medium for 1 h and subsequently in medium containing *Nyn* (10 µM) with Albumin-Alexa-594 (300 µM) for 1 h at 37º C in 6% CO_2 incubator. Sample cells were incubated with Nuclear Green (5 µM) (green) for 30 min at 37º C for nuclear staining. Stated scale bar (10 µm) is subjected for all images.

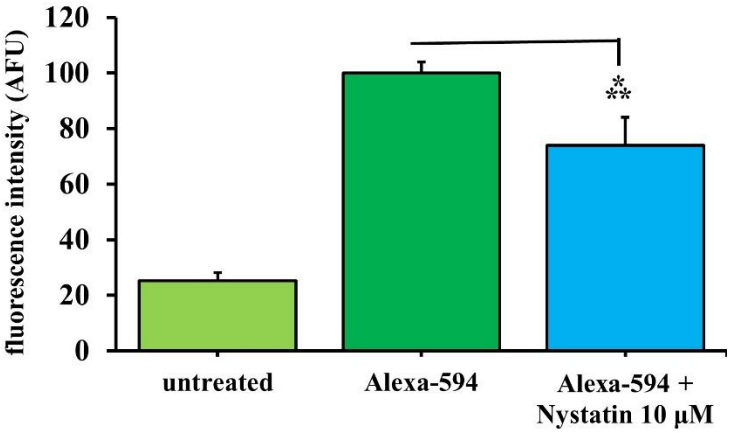

Figure 42. Semiquantitative Analysis of intracellular Albumin upon Treatment with *Nyn*. The bar chart presents Alexa-594 fluorescence in different treatment groups of *Nyn* experiment. Each data point represents mean (± SD) of 6 individual experiments. (⁂p = <0.001)

downregulation of albumin uptake by *Nyn*, indicating that ADSCs involve the caveolae-dependent pathway for albumin endocytosis (**Fig. 41** and **42**).

4.5.1.2.3 Obstruction of Caveolar Structural Conformation Reduced Albumin Uptake

Noco disrupts microtubule assembly/disassembly that produces loss of morphologic caveolae to inhibit the CDE pathway in endothelial cells (Head et al., 2006; Sun et al., 2010). In the present study, we pre-incubated ADSCs in

medium conditioned with *Noco* (30 μM, 40 μM) for 1 h and subsequently incubated in *Noco*-conditioned medium with Albumin-Alexa-594 (300 μM) for 1 h at 37º C in 6% CO_2 incubator. Samples were tested for albumin endocytosis by Alexa-594 fluorescence using C-LSM microscopy. Representative fluorescence images indicating albumin endocytosis are demonstrated in following figures (**Fig. 43-A-D**). Our accumulated data presented that *Noco* significantly shows dose-dependent downregulation of albumin uptake (**Fig. 44**), corroborating our previous data of caveolar association for albumin endocytosis in ADSCs.

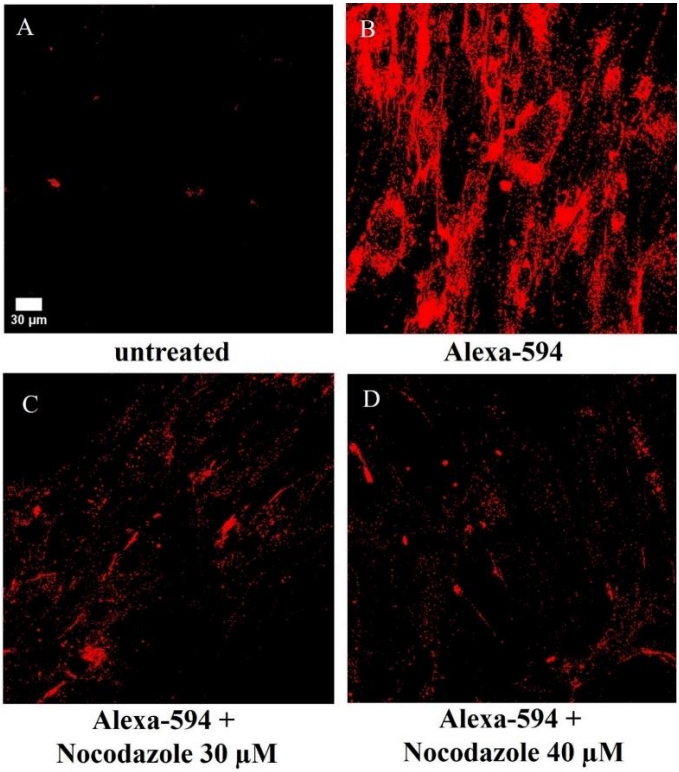

Figure 43. Albumin Uptake Inhibition by *Noco*-mediated Disruption of Microtubule Conformational Arrangement. Shown are representative confocal microscopy images of different experimental groups of untreated ADSCs (**A**), positive control, ADSCs incubated with Albumin-Alexa-594 (300 µM) for 1 h without blocker (**B**), ADSCs incubated in *Noco* (30 µM)-conditioned medium for 1 h and subsequently in *Noco* (30 µM)-conditioned medium containing Albumin-Alexa-594 (300 µM) for 1 h (**C**), ADSCs incubated in *Noco* (40 µM)-conditioned medium for 1 h and subsequently with *Noco* (40 µM)-conditioned medium with Albumin-Alexa 594 (300 µM) for 1 h (**D**) at 37º C in 6% CO_2 incubator. The stated scale bar (30 µm) is subjected for all images.

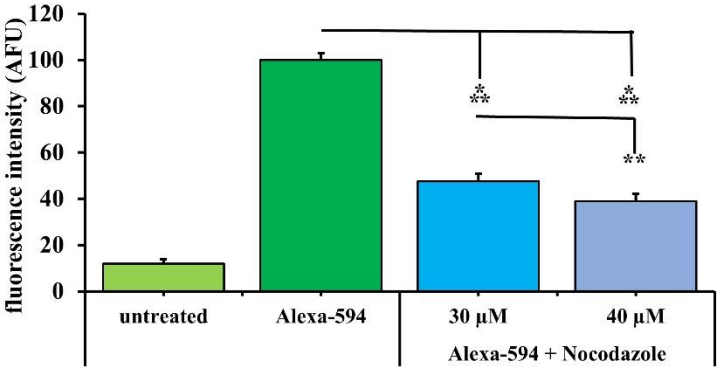

Figure 44. Semiquantitative Analysis of intracellular Albumin upon Treatment with *Noco.* The bar chart presents Alexa-594 fluorescence differences in treatments of *Noco* experiment. Each data point represents mean (± SD) value of 6 individual experiments. (**p= <0.01, ⁂P= <0.001)

4.5.1.3 Blockers Targeting Clathrin-mediated Endocytic Pathway

CME pathway involves albumin trafficking via megalin (/LRP2), a membrane glycoprotein in renal proximal tubule (PT) cells (Caruso-Neves et al., 2006). In this segment of study, we targeted CME pathway with *Chlorpromazine* (*CPZ*) and *Dyngo-4a* to investigate albumin uptake in ADSCs.

4.5.1.3.1 Inhibition of CCVs-binding to PM

CPZ was reported to downregulate CME pathway by blocking adaptin (AP2), which is crucial for orchestrating membrane proteins and other endocytic proteins for clathrin polymerization to form efficient CCVs that bind PM (Mund et al., 2023; Tobys et al., 2021). In our investigation, we preincubated sample ADSCs in *CPZ* (30 µM)-conditioned medium and subsequently in *CPZ* (30 µM)-conditioned medium with Albumin-Alexa-594 (300 µM) for 1 h at 37º C in 6% CO_2 incubator. Samples were analysed for Alexa-594

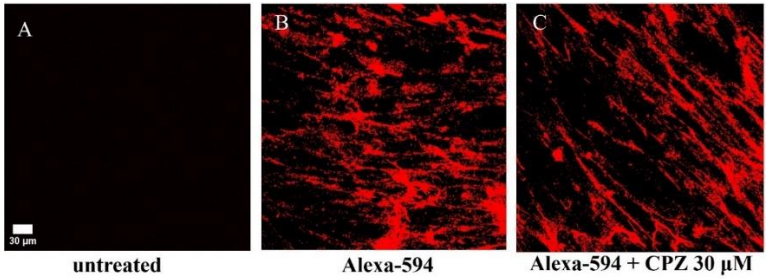

Figure 45. *CPZ*-mediated Inhibition of Albumin Uptake in ADSCs. Shown are representative confocal microscopy images of different experimental groups of untreated ADSCs (**A**), positive control, cells treated with Albumin-Alexa-594 (300 µM) (**B**), ADSCs incubated with *CPZ* (30 µM)-conditioned medium for 1 h and subsequently in *CPZ* (30 µM)-conditioned medium with Albumin-Alexa-594 (300 µM) for 1 h (**C**) at 37º C in 6% CO_2 incubator. The stated scale bar (50 µm) is subjected for all images.

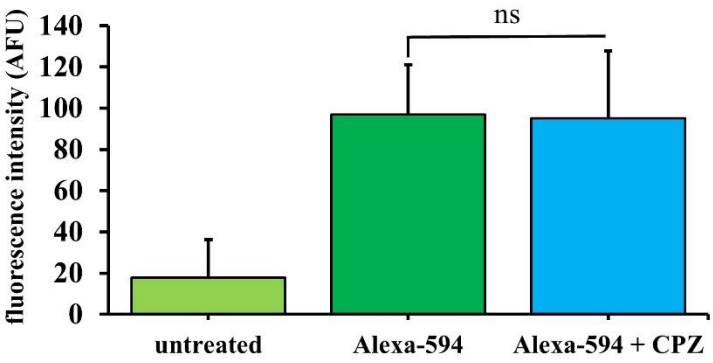

Figure 46. Semiquantitative Analysis of Intracellular Albumin upon *CPZ* Treatment. The bar chart presents Alexa-594 fluorescence difference in ADSCs. ns = not statistically significant (p = >0.05), data presented as mean (± SD) value of 6 individual experiments.

fluorescence in C-LSM to assess the level of albumin endocytosis in *CPZ* treated ADSCs. However, our data suggested no inhibitory effect of *CPZ* on albumin endocytosis in ADSCs (**Fig. 45**).

4.5.1.3.2 CME Pathway Inhibition by Blocking CCVs' Fission from PM

Dyngo-4a is a more potent version of *Dynasore* that efficiently blocks dynamin targeting membrane bound CCVs; thereby inhibiting scission of CCVs that is crucial for

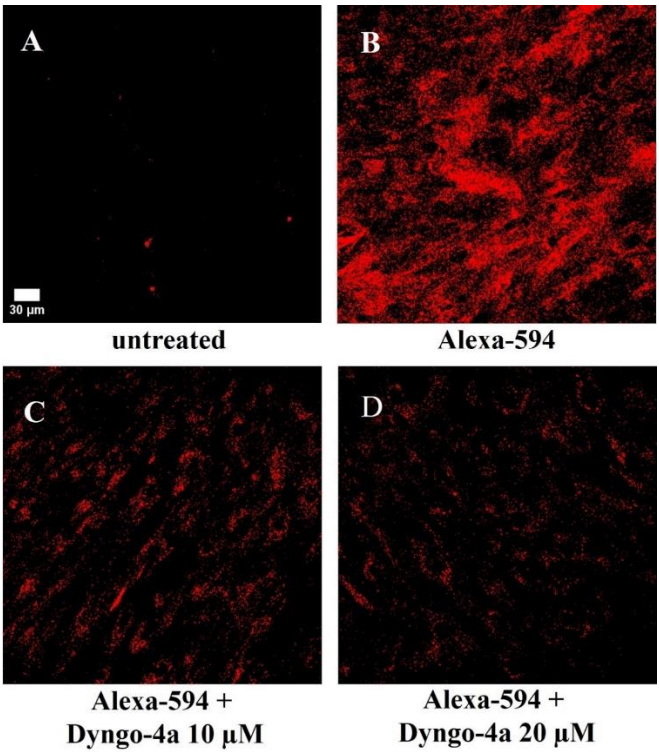

Figure 47. Clathrin-mediated Albumin Uptake Inhibition in ADSCs via Dynamin Blocking by *Dyngo-4a*. Shown are representative images from each experimental group of untreated ADSCs (**A**), positive control, ADSCs incubated in Albumin-Alexa-594 (300 µM) for 1 h without blocker (**B**), ADSCs incubated in *Dyngo-4a* (10 µM)-conditioned medium for 1 h and subsequently in *Dyngo-4a* (10 µM)-conditioned medium with Albumin-Alexa-594 (300 µM) for 1 h (**C**), ADSCs incubated with *Dyngo-4a* (20 µM)-conditioned medium for 1 h and subsequently with *Dyngo-4a* (20 µM)-conditioned medium with Albumin-Alexa-594 (300 µM) for 1 h (**D**) at 37º C in 6 % CO_2 incubator. The stated scale bar (30 µm) is subjected for all images.

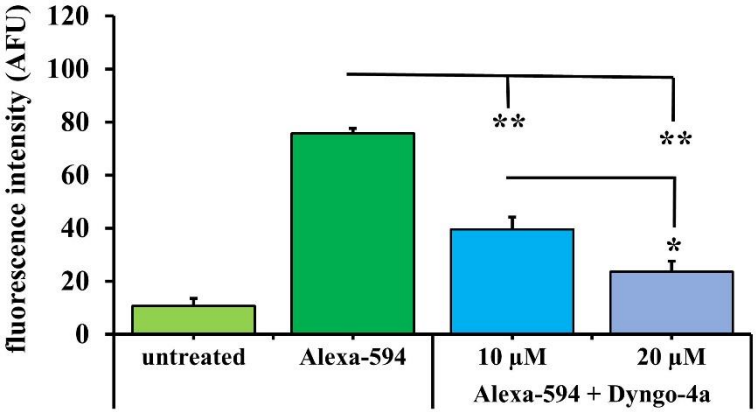

Figure 48. Semiquantitative Analysis of intracellular Albumin upon Treatment with *Dyngo-4a*. The bar chart presents Alexa-594 fluorescence differences in ADSCs incubated in *Dyngo-4a*-conditioned medium. Each data point represents mean (± SD) value of 3 individual experiments. (*p= <0.05, **p= <0.01)

the CME pathway (McCluskey et al., 2013). In the present study, ADSCs were incubated in *Dyngo-4a*-conditioned medium (10 µM, 20 µM) for 1 h at 37º C in 6% C_2O incubator and subsequently incubated in fluorescence-labelled albumin containing *Dyngo-4a*-conditioned medium to investigate albumin endocytosis. Our data demonstrated that *Dyngo-4a* significantly downregulated albumin uptake in ADSCs in a dose-dependent manner (**Fig. 47** and **48**).

4.5.1.4 Intervention of Multiple Endocytotic Pathways

Our study suggested more than one pathway involvement for albumin uptake in ADSCs where macropinocytosis and CDE seems to be dominant compared to CME. Hence, we investigated albumin endocytosis employing four sets of regimens each consisting with one blocker targeting macropinocytosis and one blocker targeting caveolae dependent pathways to test their effect in downregulating albumin uptake in ADSCs.

4.5.1.4.1 Inhibition of Albumin Endocytosis by *EIPA* in Coalition with Either *Gen* or *Nyn*

We investigated the effect of the macropinocytosis blocker *EIPA* in coalition with the CDE pathway blockers *Gen* and *Nyn*. To perform the experiment, *EIPA-Gen* regimen was formulated with *EIPA* (50 μM) and *Gen* (25 μM), whereas *EIPA-Nyn* regimen was formulated with *EIPA* (50 μM) and *Nyn* (10 μM). ADSCs were incubated in either CCM-conditioned with *EIPA-Gen* or *EIPA-Nyn* regimen for 1 h at 37º C in 6% CO_2 incubator and subsequently incubated for 1 h with Alexa-594 conjugated albumin (300 μM) added with respective regimen-conditioned medium. Sample cells were

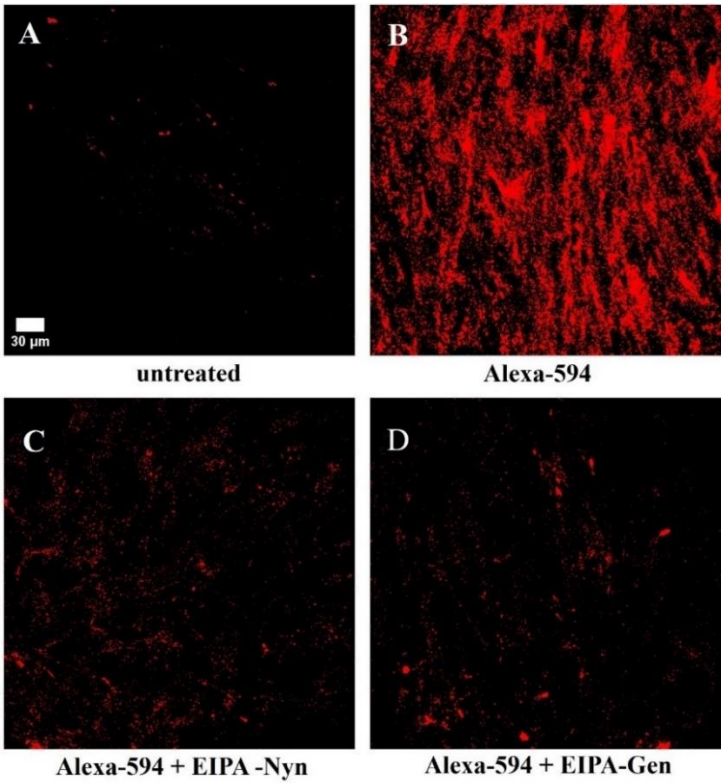

Figure 49. Multiple Pathway Intervention Effect on Albumin Endocytosis in ADSCs. Shown are representative images from different experimental groups of untreated, ADSCs incubated in CCM (**A**), positive control, ADSCs incubated for 1 h in medium conditioned with Albumin-Alexa-594 (300 µM) (**B**), ADSCs incubated for 1 h in medium conditioned with *Nyn* (10 µM), *EIPA* (50 µM) and Albumin-Alexa-594 (300 µM) (**C**), ADSCs incubated for 1 h in medium conditioned with *Gen* (25 µM), *EIPA* (50 µM) and Albumin-Alexa-594 (300 µM) for 1 h (**D**) at 37º C in 6% CO_2 incubator. The stated scale bar (30 µm) is subjected for all images**.**

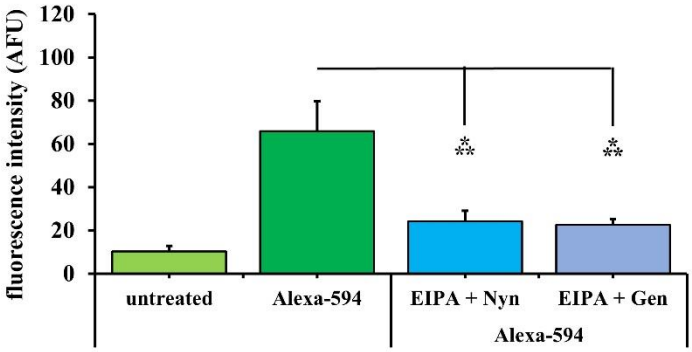

Figure 50. Semiquantitative Analysis of Intracellular Albumin upon *EIPA-Nyn*, *EIPA-Gen* Treatment. The bar chart presents Alexa-594 fluorescence differences in ADSCs. Each data point represents mean (± SD) value of 6 individual experiments. (⁂p = <0.001)

washed with PBS and investigated for differences in Alexa-594 fluorescence in C-LSM. Our data suggested that both *EIPA-Gen* and *EIPA-Nyn* regimens significantly downregulated albumin endocytosis (**Fig. 49**). Moreover, the downregulation is significantly higher compared to single pathways targeted individually (**Fig. 50**).

4.5.1.4.2 Inhibition of Albumin Uptake by *Won* in Coalition with Either *Gen* or *Nyn*

Accordingly, *Won* tested in combination with either *Gen* or *Nyn*. To perform the experiment, *Won-Gen* regimen was formulated with *Won* (20 μM) and *Gen* (25 μM), whereas

Won-Nyn regimen was formulated with *Won* (20 μM) and *Nyn* (10 μM). In this experiment, we preincubated ADSCs in either CCM-conditioned with *Won-Gen* and *Won-Nyn* regimen for 1 h at 37º C in 6% CO_2 incubator and subsequently incubated for 1 h with Alexa-594-conjugated albumin (300 μM) added with respective regimen-conditioned medium. After washing step, sample cells were investigated for albumin endocytosis at C-LSM. Accumulated data demonstrated that both *Won-Gen* and *Won-Nyn* regimens significantly downregulated albumin endocytosis in ADSCs (**Fig. 51**). For these combinations, the downregulation of albumin endocytosis is significantly higher compared to single pathways targeted individually (**Fig. 52**), indicating the participation of multiple pathways in parallel for albumin endocytosis.

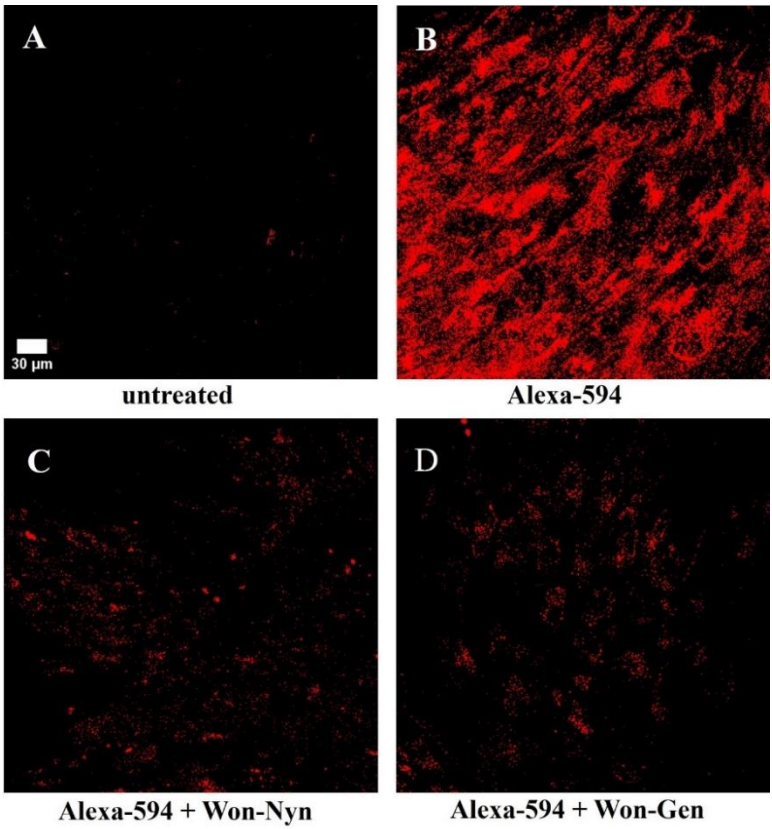

Figure 51. Albumin Uptake Downregulation by Multiple Pathway Intervention in ADSCs. Shown are representative images from different experimental groups of (**A**) untreated ADSCs, (**B**) positive control, ADSCs incubated in medium conditioned with Albumin-Alexa 594 (300 µM) for 1 h, (**C**) ADSCs incubated in *Nyn* (10 µM), *Won* (20 µM) and Albumin-Alexa-594 (300 µM)-conditioned medium for 1 h, (**D**) ADSCs incubated with *Gen* (25 µM), *Won* (20 µM) and Albumin-Alexa-594 (300 µM)-conditioned medium for 1 h at 37º C in 6% CO_2. The stated scale bar (30 µm) is subjected for all images.

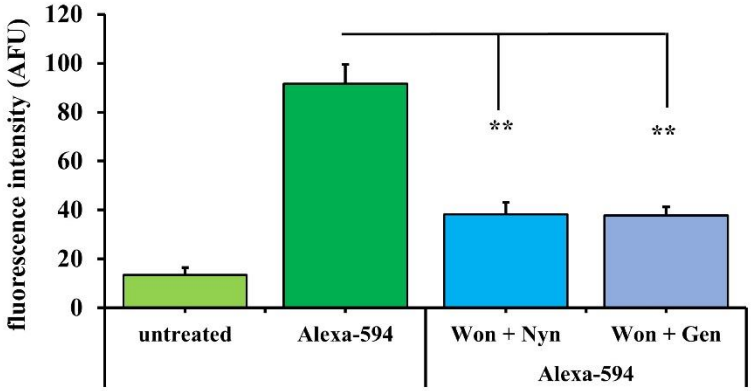

Figure 52. Semiquantitative Analysis of Intracellular Albumin upon *Won-Nyn*, *Won-Gen* Treatment. The bar chart presents Alexa-594 fluorescence of *Won-Nyn* regimen compared with *Won-Gen* . Each data point represents mean (± SD) value of 6 individual experiments. *p = <0.05, **p = <0.01.

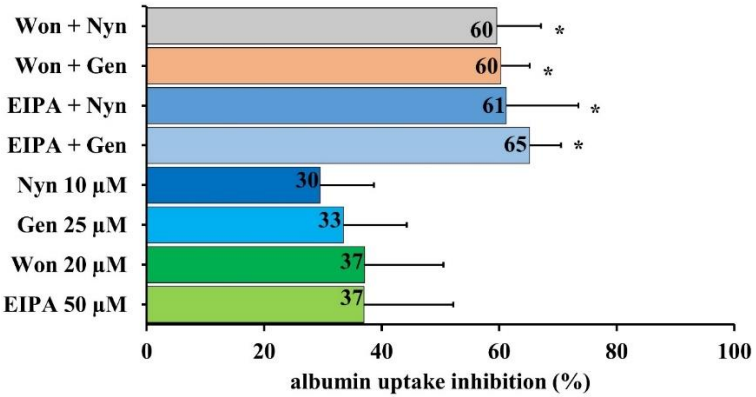

Figure 53. Albumin uptake inhibition (%) by intervention of different pathways. Each data point represents mean (± SD) value of 6 individual experiments. *p = <0.05, **p = <0.01.

4.5.1.5 Colocalization of Endocytosed Albumin with Caveolin-1 in ADSCs

Albumin trafficking via CDE pathway was further confirmed by intracellular localization of albumin with the central protein cav-1. In this experiment, we incubated living ADSCs with fluorescence-labelled albumin (300 μM) for 1 h to allow endocytosis. The cells were then incubated with mouse anti cav-1 antibody at dilution factor 1:100 for 1 h and subsequently with Alexa-Fluor-488 anti-mouse antibody (dilution factor 1:400) for 1 h. Samples were further incubated with nuclear marker DRAQ5 (1:2000) for 30 min and analyzed using C-LSM. Our data demonstrated albumin endocytosis and successful colocalization with caveolae in nuclear proximity (**Fig. 54**).

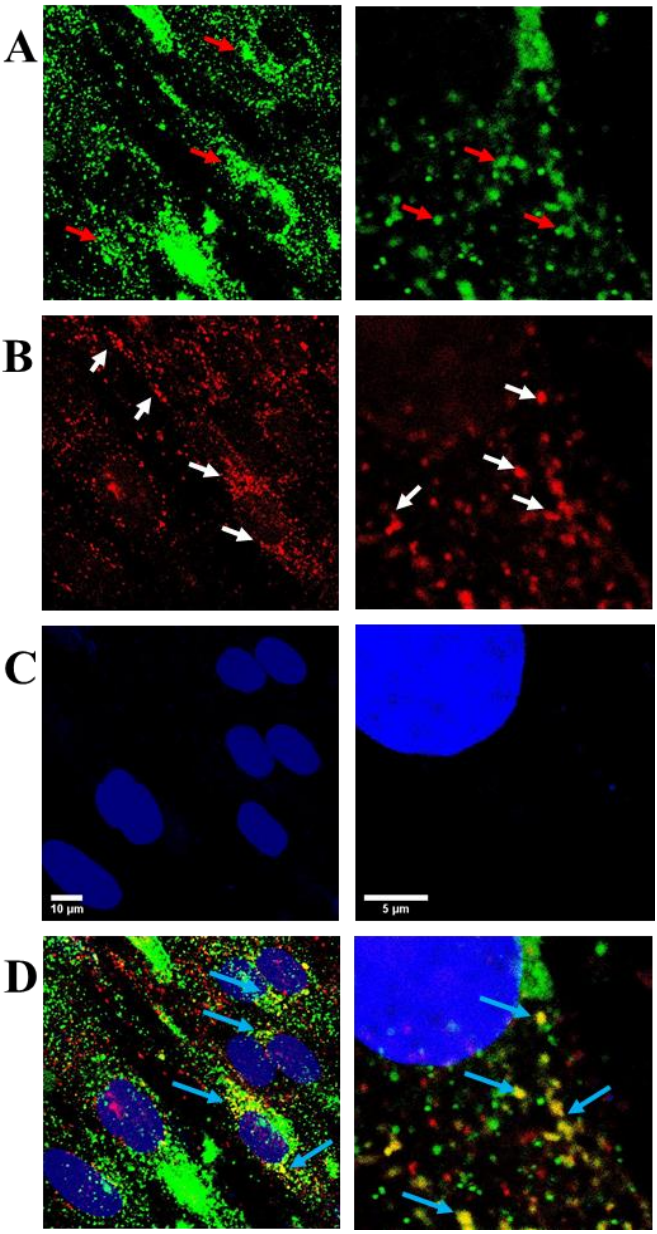
A
B
C
10 µm
5 µm
D

Figure 54. Representative Images Presenting cav-1 Colocalization with Endocytosed Albumin in ADSCs. Shown are representative confocal microscopic images of cav-1 antibody labelling (dilution 1:100) (red arrow) conjugated with Alexa-Fluor-488 anti-mouse (dilution 1:400, ThermoFischer, cat# A-21202) in ADSCs (**A**), Albumin-Alexa-594 (300 μM) (white arrow) **(B)**, nuclear region is presented with DRAQ5 (dilution 1:2000) (masked in blue) (**C**), colocalization of cav-1 and albumin (overlay) is presented by blue arrow (**D**). The stated scale bar (10 μm and 5 μm) is subjected for all images in respective columns.

4.5.1.6 Colocalization of Internalized Albumin with Megalin in ADSCs

Our data also demonstrated megalin, the CME pathway-associated protein, to be colocalized with albumin internalized in ADSCs. In this segment of experiments, ADSCs were incubated with albumin conjugated with Alexa-594 for 1 h at 37º C in 6% CO_2 incubator. The cells were incubated with anti-LRP2/megalin at a dilution factor of 1:500 for 1 h and subsequently with Alexa-Fluor-488 anti-mouse antibody (dilution 1:400). Samples were further incubated with DRAQ5 (dilution 1:2000) to label nuclear region. Our data demonstrated that megalin colocalized with endocytosed albumin (**Fig. 55**) indicating receptor-mediated endocytosis in ADSCs.

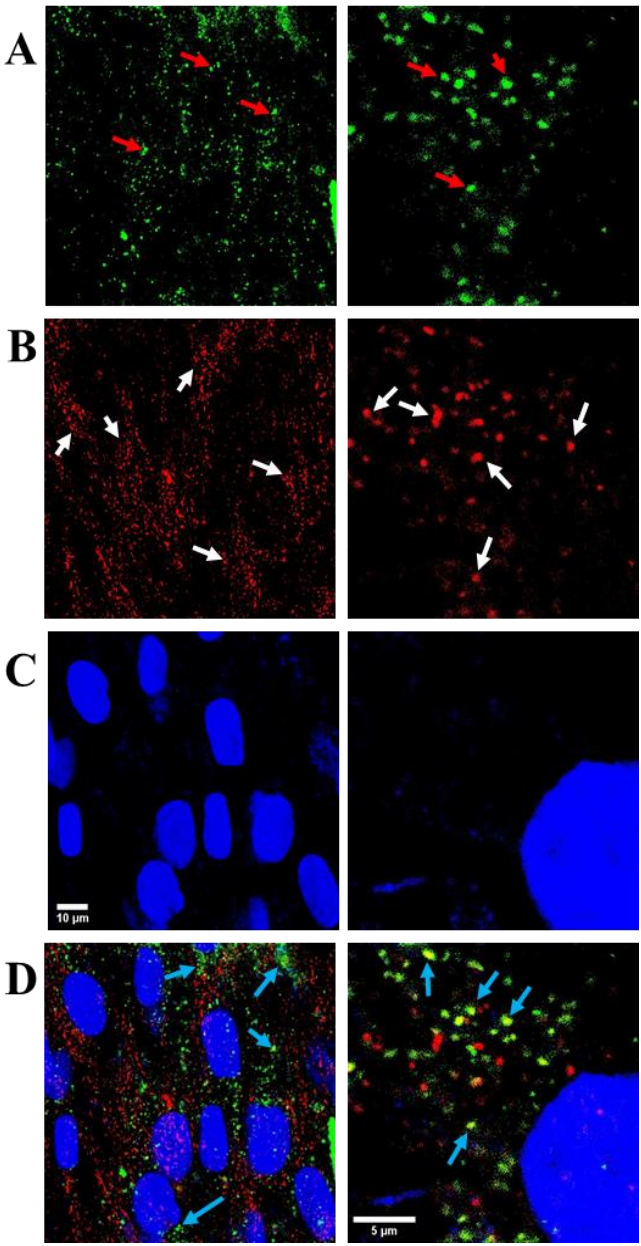
A
B
C
10 µm
D
5 µm

Figure 55. Representative Images of Megalin/Anti-LRP-2 Colocalization with Endocytosed Albumin in ADSCs. Shown are representative confocal microscopic images of anti megalin antibody (dilution 1:500) (red arrow) conjugated with anti-mouse Alexa-Fluor-488 (dilution 1:400) (**A**), Albumin-Alexa-594 (300 μM) (white arrow) **(B)**, nuclear region is detected with DRAQ5 (dilution 1:2000) nuclear staining (**C**), colocalization of megalin and albumin (overlay) is presented by blue arrow (**D**). The stated scale bar (10 μm and 5 μm) is subjected for all images in respective columns.

4.5.1.7 Investigation of Albumin Uptake in ADSCs by BSA-conjugated Endocytic Probe

LactosylCeramide endocytosis is a marker for CDE however independent of dynamin-2, caveolae-1 and clathrin (Glebov et al., 2006; Vercauteren et al., 2010). We investigated *BODIPY™ FL C5-LactosylCeramide-BSA* (*LacCer*, Invitrogen, cat # B34402) uptake at two different concentrations (2 μM and 4 μM) in ADSCs. In this experiment, we pre-incubated ADSCs with *Gen* (25 μM) for 1 h and subsequently with *Gen*-conditioned CCM containing *LacCer* with respective concentrations for 1 h at 37º C in 6% CO_2 incubator. ADSCs were subsequently investigated at C-LSM at the excitation wavelength of 488 nm and emission at >515 nm. Representative fluorescence images from each experimental group are presented in **Fig. 56-A-E**. Our data

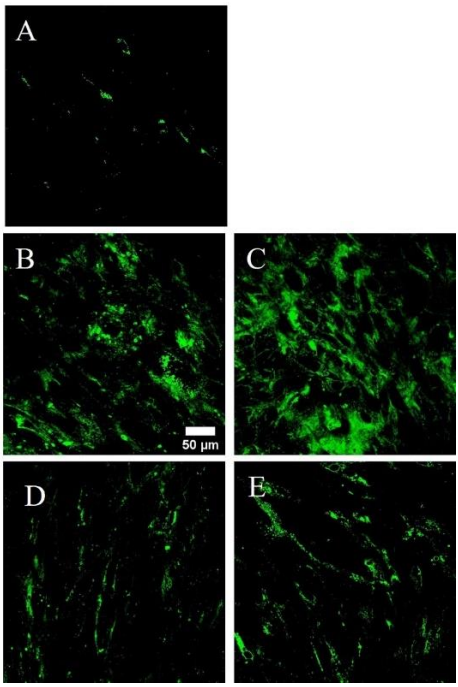

Figure 56. *Gen*-mediated inhibition of *BODIPY FL C5-LactosylCeramide-BSA* (*LacCer*) Uptake in subcutaneous ADSCs. Shown are representative images from each experimental group of (**A**) negative control, untreated ADSCs, (**B**) positive control 1, ADSCs incubated in *LacCer* (2 µM) containing medium for 1 h without *Gen*, (**C**) positive control 2, ADSCs incubated in *LacCer* (4 µM) containing medium for 1 h without *Gen*, (**D**) ADSCs incubated in *Gen* (25 µM)-conditioned medium for 1 h and subsequently with *Gen* (25 µM)-conditioned medium with *LacCer* (2 µM) for 1 h, (**E**) ADSCs incubated with *Gen* (25 µM)-conditioned medium for 1 h and subsequently with *Gen* (25 µM)-conditioned medium with *LacCer* (4 µM) for 1 h at 37º C in 6% CO_2 incubator. The stated scale bar (50 µm) is subjected for all images.

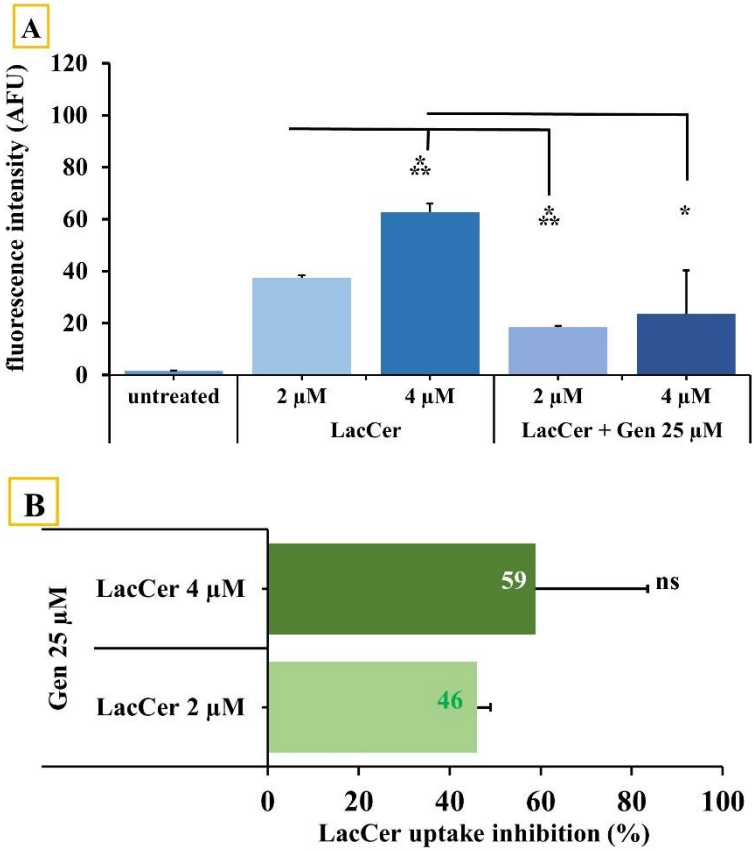

Figure 57. *Gen*-mediated Inhibition of *LacCer* Uptake in subcutaneous ADSCs. The upper bar chart presents fluorescence differences in ADSCs incubated without *Gen*-conditioned medium compared with ADSCs incubated with *Gen*-conditioned medium (**A**). The lower bar chart presents *Gen*-mediated inhibition (%) of *LacCer* (2 µM, 4 µM) endocytosis (**B**). At least 4 individual experiments were done for each group. *p= <0.05, ⁂p = <0.001, ns = not significant (p = >0.05).

showed that *Gen* significantly downregulated *LacCer* uptake at both concentrations (**Fig. 57-A**), indicating caveolae-dependent endocytosis in ADSCs. We observed dose-dependent effects with higher concentration of *LacCer*, however the rate of endocytosis downregulation by *Gen* remained unaffected (**Fig. 57-B**).

4.5.2 Ca^{2+} Signaling Regulates Albumin Endocytosis

We hypothesised that intracellular Ca^{2+} signal drives albumin endocytosis in ADSCs. To test this hypothesis, we intervened Ca^{2+} signaling through Ca^{2+} signal blockers as described in ***section 3.4.3*** (**a**. *NPS-2143*, a CaSR antagonist, **b**. *SKF-96365*, a SOCE inhibitor and **c**. *BAPTA-AM*, an intracellular Ca^{2+} scavenger) to investigate their effect on albumin endocytosis in ADSCs.

4.5.2.1 Downregulation of Albumin Uptake by Inhibition of Ca^{2+} Signaling Via *NPS-2143*

We incubated ADSCs in *NPS-2143* (5 μM)-conditioned E1 buffer (with Ca^{2+}, 1.8mM) (described in ***section 2.4***) for 1 h and subsequently with fluorescence-labelled albumin (300 μM) along-with *NPS-2143* (5 μM) for 1 h at 37º C in 6% CO_2. Sample ADSCs were subjected to incubation with nuclear green (5 μM) for 30 min which resulted in nucleus labelling. Sample cells were washed with E1 buffer (without Ca^{2+}) to remove unbound agents after each incubation steps and analysed for Alexa-594 fluorescence on C-LSM. The data accumulated in this investigation demonstrated significant downregulation of albumin uptake indicating that disruption of Ca^{2+} signaling by the calcilytic activity of *NPS-2143* downregulated albumin endocytosis in ADSCs (**Fig. 58** and **59**). We observed unspecific nucleotide binding presumably in mitochondria as well as in the nuclear region by Nuclear Green (**Fig. 58-A-C**).

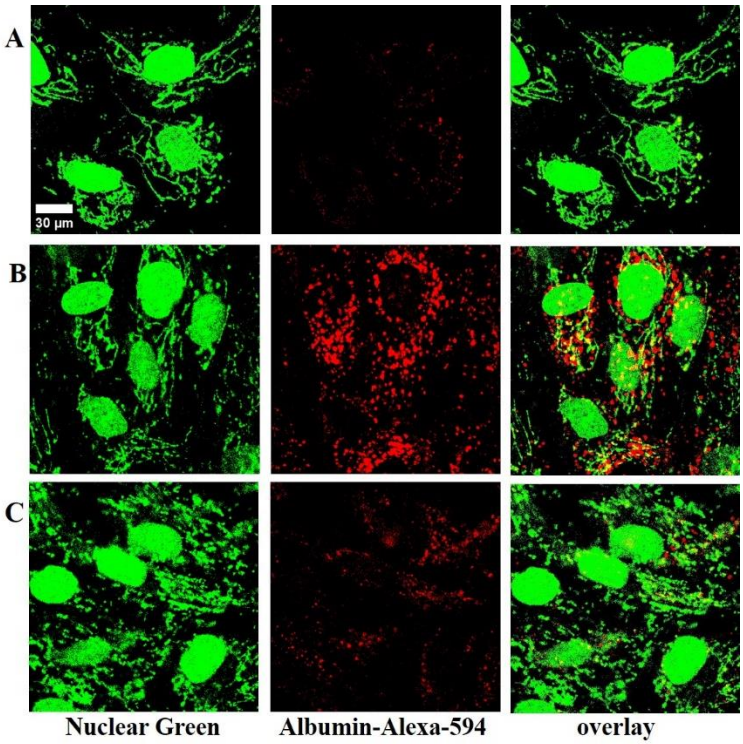

Figure 58. Downregulation of Albumin Uptake by Modulating Ca^{2+} Signaling via CaSR in ADSCs. ADSCs were preincubated for 1 h in 37 °C in E1 buffer (with Ca^{2+}), **A.** Untreated ADSCs, **B.** ADSCs were incubated with Albumin-Alexa-594 (300 µM), without *NPS-2143*, **C.** ADSCs were incubated with *NPS-2143* (5 µM) for 1 h and with *NPS-2143* (5 µM) and Albumin-Alexa-594 (300 µM) for 1 h. For Nuclear staining, sample ADSCs were incubated with Nuclear Green (5 µM) for 30 min. Scale bar stated (20 µm) subjected for all images.

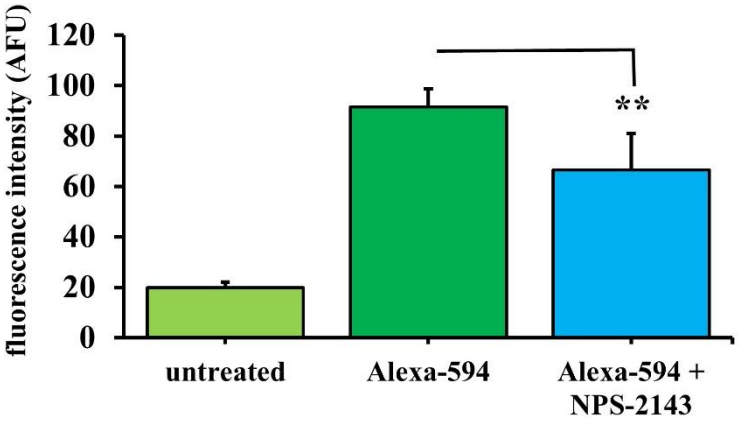

Figure 59. Semiquantitative Analysis of Intracellular Albumin Upon Treatment with *NPS-2143*. The bar chart presents Alexa-594 Fluorescence in different experimental groups from CaSR-mediated downregulation of albumin uptake. Presented data are mean (± SD) of 6 individual experiments, **p= <0.01.

4.5.2.2 Inhibition of Albumin Endocytosis by Blocking Ca^{2+} Influx via SOCE Inhibitor

The clathrin-mediated endocytosis was reported to be associated with Ca^{2+} influx through SOCE (Wang et al., 2017; Zeng et al., 2017). To investigate the association of SOCE-mediated Ca^{2+}-signal with albumin uptake in ADSCs, we preincubated ADSCs with *SKF-96365* (2 µM)-conditioned E1 buffer (with Ca^{2+}, 1.8 mM) (described in ***section 2.4***) for 1 h and subsequently added fluorescence-

labelled albumin (300 µM) for 1 h at 37º C in 6% CO_2 incubator. Intervention of albumin endocytosis via SOCE inhibition was investigated by contrasting Alexa-594 fluorescence between different groups. Our accumulated data presented significant reduction in albumin endocytosis upon blocking SOCE which indicates albumin endocytosis in ADSCs is associated with SOCE mediated Ca^{2+} flux.

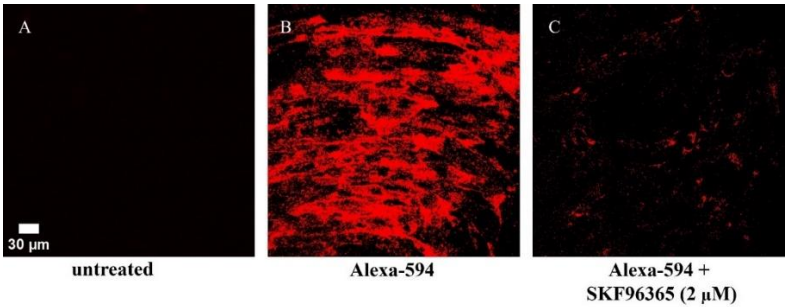

Figure 60. Inhibition of Albumin Endocytosis by Interfering with Ca^{2+} Entry through SOCE in ADSCs. Sample ADSCs were preincubated for 1 h in 37 °C in E1 buffer (containing Ca^{2+}) at 37º C in 6% CO_2. Shown are representative images from different experimental groups of untreated ADSCs (**A**), positive control, ADSCs incubated with Albumin-Alexa-594 (300 µM) (without *SKF-96365*) for 1 h (**B**), ADSCs incubated in *SKF-96365* (2 µM)-conditioned buffer with Albumin-Alexa-594 (300 µM) for 1 h (**C**) at 37º C in 6% CO_2. Samples were investigated in C-LSM. The stated scale bar (30 µm) is subjected for all images.

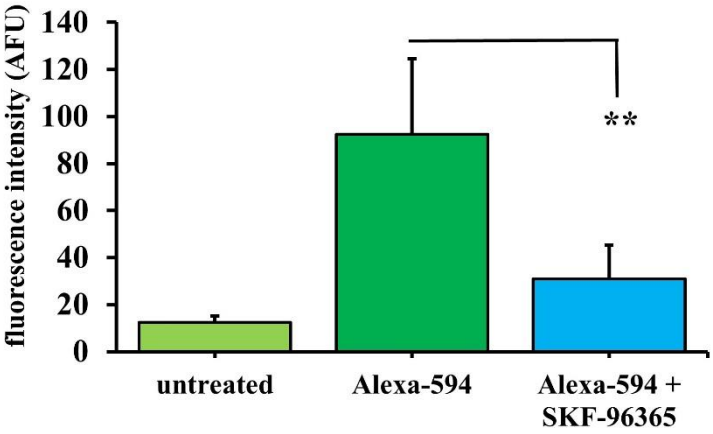

Figure 61. Semiquantitative Analysis of Intracellular Albumin upon *SKF-96365* Treatment. The bar chart presents fluorescence intensity in different treatments. Each data points are presented as mean (± SD) of 6 individual experiments (**p = < 0.01).

4.5.2.3 Intracellular Ca^{2+} Scavenger *BAPTA* Downregulates Albumin Uptake

BAPTA-AM is a well-documented intracellular Ca^{2+} scavenger. In the next experiment, we investigated whether intracellular Ca^{2+} transients modulate albumin endocytosis in ADSCs by *BAPTA-AM* administration. For this experiment, ADSCs were preincubated with *BAPTA-AM*

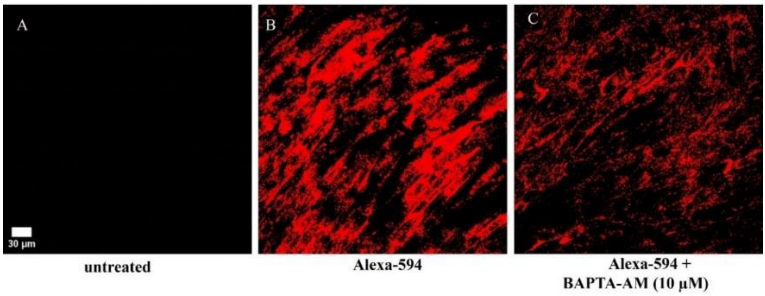

Figure 62. Downregulation of Albumin Endocytosis by Interfering Ca^{2+} Release via *BAPTA* in ADSCs. Sample ADSCs were preincubated for 1 h in 37 °C in E1 buffer (without Ca^{2+}). Shown are representative images from different experimental groups of untreated ADSCs (**A**), positive control, ADSCs incubated with albumin-Alexa-594 (300 µM), without *BAPTA-AM* (**B**), ADSCs incubated with *BAPTA-AM* (10 µM) and Albumin-Alexa-594 (300 µM) (**C**). The stated scale bar (30 µm) is subjected for all images.

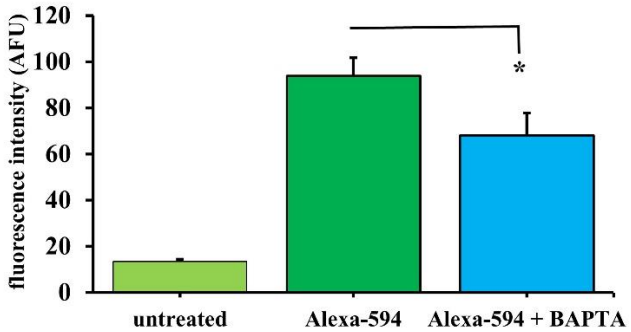

Figure 63. Semiquantitative Analysis of Intracellular Albumin upon *BAPTA* Treatment. The bar chart presents a comparison of Alexa-594 fluorescence intensity between different experimental groups. Each data point represents mean (± SD) value of 3 individual experiments. (*p = < 0.05)

(10 µM)-conditioned E1 buffer (without Ca^{2+}) (described in ***section 2.4***) for 1 h and subsequently incubated with fluorescence-labelled albumin (300 µM) in *BAPTA*-conditioned E1 buffer for 1 h at 37º C in 6% CO_2 incubator. Sample ADSCs monolayers were washed with E1 buffer (without Ca^{2+}) after each incubation steps. Albumin endocytosis was analysed by Alexa-594 fluorescence of different samples using C-LSM. Our data from *BAPTA*-treated group presented significant downregulation of albumin uptake compared to the untreated group indicating intracellular Ca^{2+} signaling as a vital player in regulating albumin endocytosis (**Fig. 63**).

4.5.2.4 Extra-/Intra-cellular Ca^{2+} Signal Dictates Albumin Endocytosis

Albumin has at least thirty negatively charged amino acid side chains which can bind Ca^{2+}, where eleven sites are described as stable and three are highly stable, and this binding imparts concentration-dependent conformational change without impairing the secondary structure (Patel et al., 2022). This binding and change of the protein structure at tertiary level may impose functional differences.

Our accumulated data from Ca^{2+} scavenger and different modulators indicated that albumin endocytosis is modulated by Ca^{2+} signals. These findings led us to investigate further albumin uptake regulation at different Ca^{2+} concentrations to explore whether extracellular as well as intracellular Ca^{2+} levels are modulating albumin uptake in ADSCs. In this part of the study, sample ADSCs were incubated for 1 h with *BAPTA-AM* (10 M) and different concentration (0.0, 0.5, 1.0 and 1.8 mM) of Ca^{2+} dissolved in E1 buffer, and subsequently in fluorescence-labelled albumin with respective $CaCl_2$/*BAPTA-AM*-conditioned E1 buffer for 1 h at 37º C in 6% CO_2 incubator. Respective f.c. of Ca^{2+} and *BAPTA-AM* were maintained throughout the experiment. Control group was devoid of any added Ca^{2+} or *BAPTA-AM*. The data accumulated from this experiment demonstrated that ADSCs with intracellular Ca^{2+} (not scavenged with *BAPTA* and without additional extracellular Ca^{2+}) presented significantly higher albumin endocytosis compared to the cells devoid of Ca^{2+} (intracellular and extracellular). The level of albumin uptake in the ADSCs in which intracellular Ca^{2+} is not scavenged by *BAPTA* was reached by the cells supplemented with 1.0 mM (and 1.8 mM) Ca^{2+}. Moreover, significantly lower albumin endocytosis was observed in

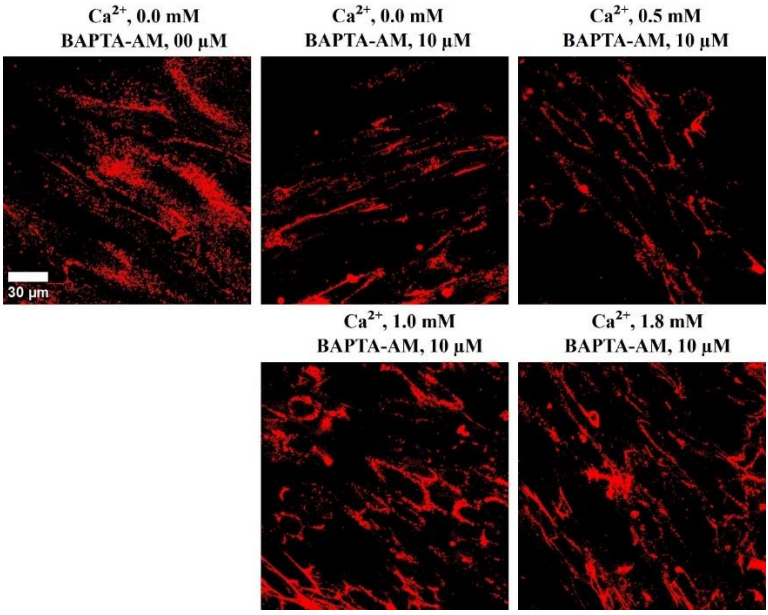

Figure 64. Albumin Endocytosis in ADSCs Depends on Extra/intra-cellular Ca^{2+} Signaling. **A.** Representative C-LSM images depicted from ADSCs incubated with different Ca^{2+} concentration and *BAPTA-AM* (10 µM) for 1 h at 37º C in 6% CO_2 incubator. Each group was incubated for 1 h at 37º C with fluorescence-labelled albumin to trace albumin endocytosis in ADSCs. Scale bar (30 µm) is subjected for all images.

cells presumably devoid of Ca^{2+} (intracellular Ca^{2+} scavenged with *BAPTA* and absence of extracellular Ca^{2+}) compared with cells containing extracellular Ca^{2+} (intracellular Ca^{2+} was scavenged by *BAPTA* and incubation

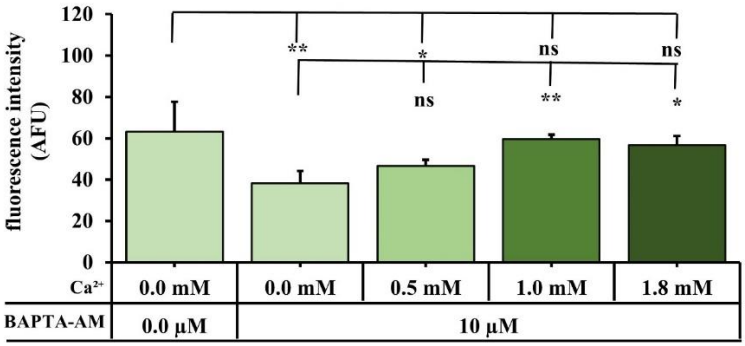

Figure 65. Semiquantitative Analysis of Albumin Uptake Upon Different Extracellular Ca^{2+} Concentrations. The bar chart presents Alexa-594 fluorescence in different treatment groups of ADSCs incubated in Ca^{2+}-conditioned medium. Each data point represents mean (± SD) of 4 individual experiments. *p= <0.05, **p= <0.01 and ns = not significant (p= >0.05).

buffers were supplemented with 0.5 and 1.0 mM Ca^{2+}), indicating that the albumin endocytosis was increased by extracellular Ca^{2+} in a concentration-dependent manner. These observations suggest that Ca^{2+} signal dictates albumin endocytosis from either extracellular or intracellular stores in ADSCs.

4.6 Interplay Between FcRn-mediated Albumin Internalization and Ca^{2+} Signaling

To the best of our knowledge, FcRn was not described in ADSCs of human origin in previous studies. We investigated FcRn expression in ADSCs across three different age-groups (20-34-, 35-49- and 65–80-year-old). This experiment was performed according to the protocol described in ***section 3.7***. The blots were incubated overnight with rabbit anti FcRn antibody at a dilution factor of 1:2000 to validate the presence of FcRn in ADSCs. FcRn was conjugated with donkey anti-rabbit antibody at a dilution factor 1:1000 as secondary antibody. Rabbit anti-vinculin antibody was used at a dilution factor 1:2000 as a loading reference. A representative WB densitometric comparison is presented below (**Fig. 66-A**). Relative FcRn expression showed no significant difference in three different age groups (**Fig. 66-B**), indicating constant FcRn expression across different age groups.

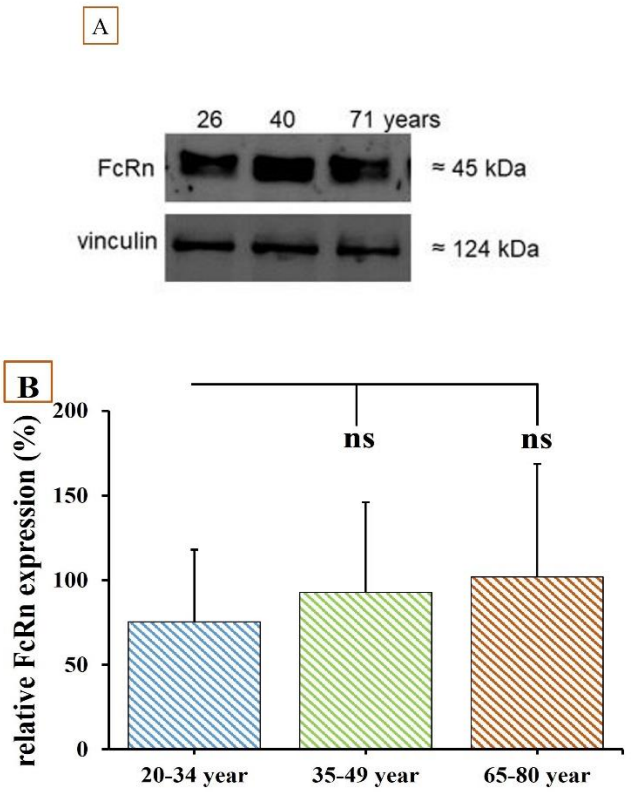

Figure 66. FcRn Expression in ADSCs Isolated from Donors of Different Age Groups (20-34-, 35-49- and 65–80-year-old). **A.** Densitometric analysis of a representative FcRn protein expression. The blot was incubated with rabbit anti-FcGrT polyclonal antibody and rabbit anti-vinculin antibody used as a reference housekeeping protein. HRP-conjugated donkey anti-rabbit antibody was used for secondary conjugation. **B.** The bar chart shows comparison of FcRn expression in different age groups. (n=9 individual experiments, ns = not statistically significant, *p= <0.05)

4.6.1 Colocalization of FcRn and Albumin in ADSCs

Since we observed FcRn protein expression in subcutaneous ADSCs across different age groups, we performed immunocytochemical detection of FcRn in ADSCs by confocal microscopy. In this segment of study, we demonstrated that intracellular albumin is colocalized with FcRn in ADSCs. To perform this experiment, we incubated ADSCs with Albumin-Alexa-594 (300 μM)-conditioned medium for 1 h at 37º C in 6% CO_2 incubator to facilitate albumin internalization. After washing steps cells were incubated with antibody directed against FcRn at a dilution factor of 1:200 and subsequently conjugated with Alexa-Fluor-488 donkey anti-rabbit at a dilution factor of 1:400 incubating for 1 h at 37º C in 6% CO_2 incubator. All the samples were incubated with nuclear marker DRAQ5 (1:2000) for 30 min at 37º C in 6% CO_2 incubator. Immunofluorescence analysis at C-LSM revealed endocytosed albumin colocalization with FcRn. Representative immunofluorescent images are demonstrated here depicting FcRn (red arrow, **Fig. 67-A**), albumin (white arrow, **Fig. 67-B**) and colocalization (blue arrow, **Fig. 67-D**).

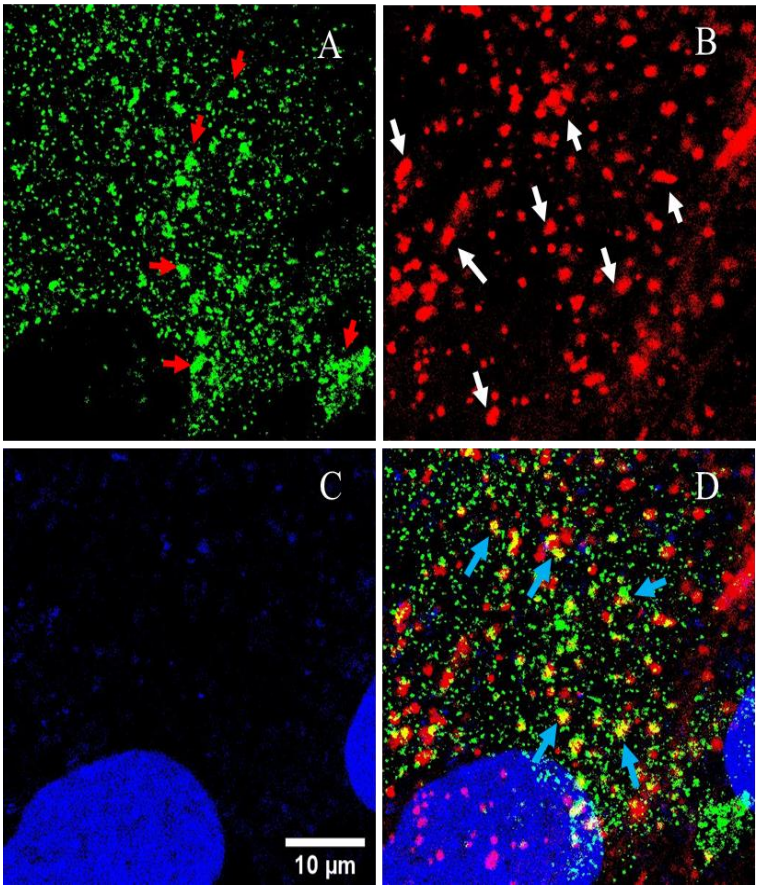

Figure 67. Representative Images of FcRn and Endocytosed Albumin Colocalization in Subcutaneous ADSCs. Representative images demonstrated FcRn (red arrow, image **A**), albumin (white arrow, image **B**), nuclear region marked with DRAQ 5 (blue region, image **C**), and overlay (blue arrow, image **D**) shows colocalization of FcRn and endocytosed albumin. The stated scale bar (10 µm) is subjected for all images.

4.6.2 Generation of FcRn Knockout ADSC Population

To test our hypothesis that Ca^{2+} modulates FcRn during albumin endocytosis, we investigated FcRn interplay with Ca^{2+} oscillations and albumin internalization using FcRn-deficient ADSCs or by blocking ligand binding receptors on FcRn. To generate FcRn knockout cells we conducted both the electroporation and the chemical transfection approach. Moreover, we confirmed our data by further investigating the impact of FcRn expression in ADSCs on albumin content and Ca^{2+} signaling by blocking FcRn with the novel synthetic anti FcRn antibody *M281* which is designed to block the IgG binding site on FcRn (Choudhury et al., 2022; Guptill et al., 2022).

4.6.2.1 FcGRT Knockout by Electroporation of si-RNA Directed Against FcRn

We downregulated FcRn expression in ADSCs using si-RNA directed against FcRn (human FcGRT) by Neon Transfection technology to generate $FcRn^{-}$ ADSC cell lines according to the protocol described in ***section 3.5.1.1*** and validated for transfection efficiency by $FcRn^{+}$ immunocytochemistry.

Sample ADSCs from all experimental groups were incubated with antibody against FcRn at a dilution factor of 1:200 and subsequently conjugated with Alexa-Fluor-488 donkey anti-rabbit at a dilution factor of 1:400 incubating for 1 h. All the samples were incubated with nuclear marker DRAQ5 (1:2000) for 30 min at RT. All the sample ADSCs monolayers were washed with PBS after each incubation steps. All the samples were analysed using C-LSM and computer assisted image analysis software. Our accumulated data demonstrated that the ADSCs group which was not transfected (positive control), the vehicle ADSC group which was pulse--treated with buffer lacking si-RNA duplexes and the ADSCs which were transfected with sc-RNA (scrambled si-RNA) duplexes did not display significant differences in FcRn expression, whereas the group treated with si-RNA against FcRn presented significantly lower FcRn fluorescence, indicating successful downregulation of FcRn. Representative immunofluorescent images are presented to demonstrate different groups contrasting FcRn expression in $FcRn^{+}$ ADSCs and $FcRn^{-}$ ADSCs (**Fig. 68-A-E**). Analysis of fluorescent intensity of Alexa-Fluor-488 presented significantly downregulated

FcRn expression in $FcRn^{-}$ ADSC generation contrasting with FcRn expression in $FcRn^{+}$ ADSCs (**Fig. 69**).

Subsequently, $FcRn^{-}$ ADSCs were investigated for albumin internalization (**Fig. 70**) according to the protocol described in ***section 3.4***. The data accumulated in this experiment suggested that significantly lower albumin was endocytosed in the cells transfected with si-RNA compared with the sc-RNA treated and untreated ADSCs (**Fig. 71**), indicating FcRn-mediated albumin internalization.

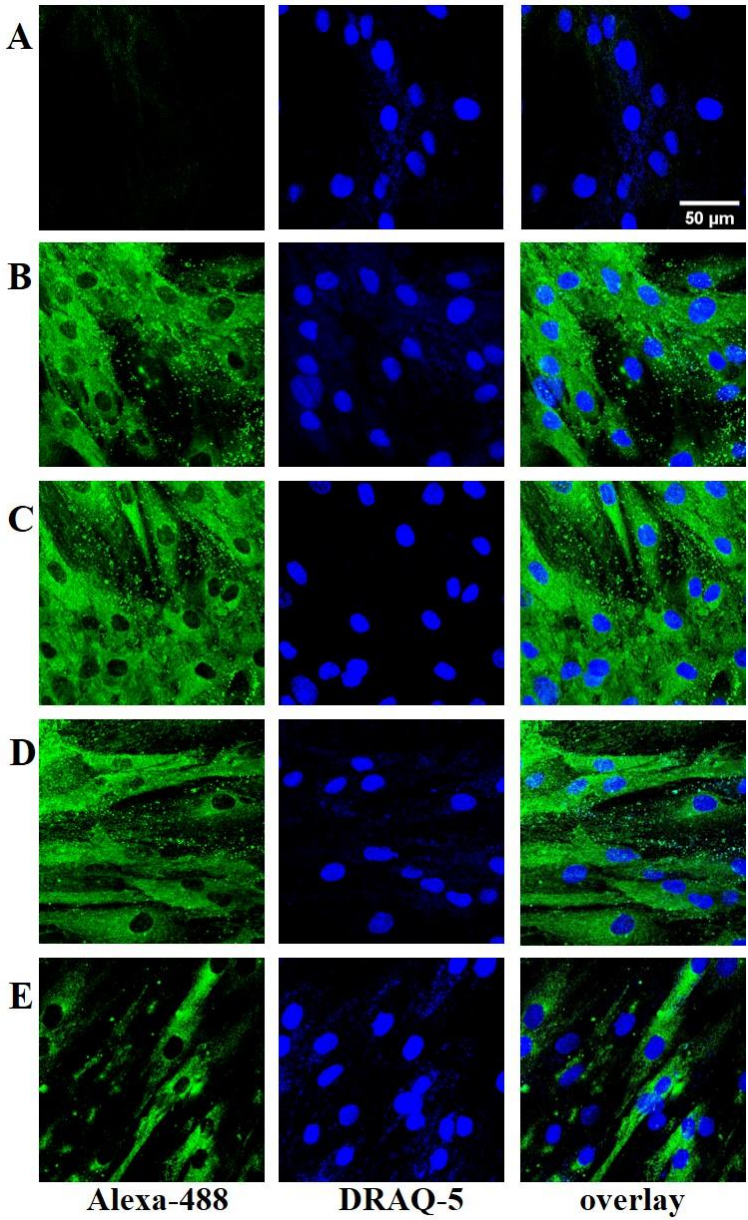
A
B
C
D
E
50 µm
Alexa-488
DRAQ-5
overlay

Figure 68. Downregulation odf FcRn Expression in FcRn^{-} ADSCs Generated Through Electroporation of si-RNA Against FcRn. Representative images from different treatments are showing negative control (incubated without secondary antibody, lacking transfection) (**A**), untreated ADSCs (lacking transfection) (**B**), vehicle (pulse without si-RNA duplexes) (**C**), ADSCs transfected with sc-RNA (100 nM) (**D**), ADSCs transfected with si-RNA (100 nM) (**E**). Samples were incubated with antibody against FcRn (1:200) for 1 h and with Alexa-Fluor-488 (1:400) for 1 h and subsequently with DRAQ 5 (1:2000) for 30 min. The stated scale bar (50 μm) is subjected for all images.

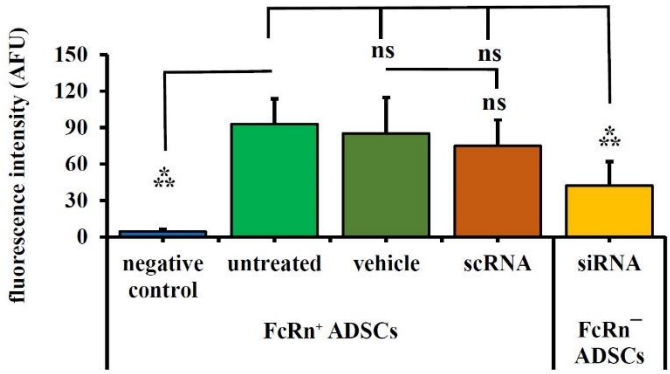

Figure 69. Semiquantitative Analysis of Intracellular FcRn Expression Upon Treatment With si-RNA Against FcRn. The bar chart presents fluorescence intensity of Alexa-Fluor-488 conjugated with antibody directed against FcRn in different treatment groups. Each data point represents mean (± SD) of 10 individual experiments. (⁂$p < 0.001$, ns >0.05)

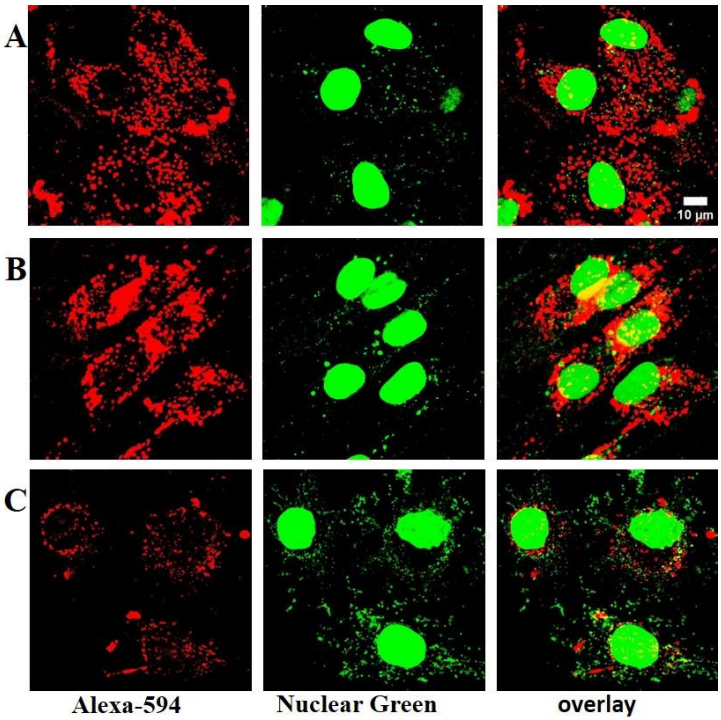

Figure 70. The Level of Endocytosed Albumin is Downregulated in the $FcRn^{-}$ ADSC Population Generated Through Electroporation. Representative images from different treatments showing untreated ADSCs ($FcRn^{+}$ ADSCs, cells lacking transfection) (**A**), sc-RNA, presenting $FcRn^{+}$ ADSCs, cells transfected with sc-RNA (100 nM) (**B**), si-RNA, $FcRn^{-}$ ADSCs, cells transfected with si-RNA (100 nM) (**C**). Test samples were incubated with Albumin-Alexa-594 (300 µM) for 2 h and with Nuclear Green (2 µM) for 1 h at 37º C and investigated in C-LSM at RT. The stated scale bar (10 µm) is subjected for all images.

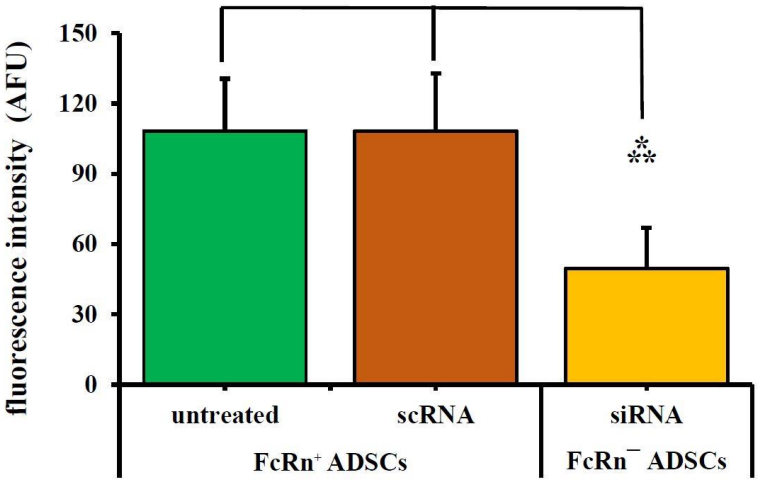

Figure 71. Semiquantitative Analysis of Intracellular Albumin Upon si-RNA Inactivation of FcRn. The bar chart presents fluorescence intensity of Alexa-594 indicating level of endocytosed albumin in each experimental group. Each data point represents mean (± SD) of 17 individual experiments. (⁂$p < 0.001$)

4.6.2.2 Chemical Transfection of si-RNA Against FcRn

We crosschecked our results from $FcRn^-$ cell population developed by electroporation technology by employing the chemical transfection, INTERFERin® transfection system, according to the protocol described in ***section 3.5.1.2***. About 50% confluent ADSCs were transfected with si-RNA against FcRn mediated by INTERFERin®. Accordingly,

INTERFERin® was added to the mix containing si-RNA duplexes and added to the ADSC culture containing fresh CCM which were validated after 48 h post-transfection by FcRn immunocytochemistry (**Fig. 72**). Transfection was validated by TYE563-labelled transfection control si-RNA shown in **Fig. 72-B**. Our data demonstrated that INTERFERin® transfection system resulted in FcRn knockout at about 49%, and albumin uptake was downregulated by 31.4% (**Fig. 73**). Furthermore, FcRn knockout was validated by western blot experiments using antibody directed against FcRn according to the protocol described in the ***section 4.6***. Densitometric analysis presented contrasting FcRn expression between $FcRn^{+}$ ADSCs and $FcRn^{-}$ ADSCs (**Fig. 74-A**), and relative FcRn expression showed significant downregulation of FcRn expression in the $FcRn^{-}$ ADSC population (**Fig. 74-B**), indicating successful transfection.

According to our working hypothesis, $FcRn^{-}$ ADSCs will present downregulated level of intracellular albumin content compared to the $FcRn^{+}$ ADSCs i.e. not transfected with si-RNA directed against FcRn. To test this hypothesis, we investigated albumin internalization level in $FcRn^{-}$ ADSCs according to the protocol described in ***section 3.4***. Our data

showed that significantly lower albumin was present in the cells transfected with si-RNA compared with ADSCs transfected with sc-RNA (scrambled si-RNA) and untreated ADSCs (ADSCs which were not transfected with si-RNA) (**Fig. 73-B**), indicating albumin internalization is modulated by FcRn or albumin is more rapidly degraded in the absence of FcRn.

Moreover, we investigated Ca^{2+} oscillations in $FcRn^{-}$ ADSCs and compared with $FcRn^{+}$ ADSCs (untreated and sc-RNA treated ADSCs) according to the protocol described in ***section 3.3***. We calculated the percentage of actively oscillating cells in $FcRn^{+}$ and $FcRn^{-}$ ADSCs and analyzed their typical to the Ca^{2+} oscillation characteristics. Representative time course of Ca^{2+} oscillations from each group are depicted in **Fig. 75**. $FcRn^{-}$ ADSCs (**Fig. 75-C**) presented significantly lower Ca^{2+} signaling in aspect of spike frequency and amplitude compared with untreated (**Fig. 75-A**) and sc-RNA treated (**Fig. 75-B**) ADSCs. $FcRn^{-}$ ADSCs population represented less Ca^{2+} oscillation-active cells compared to the untreated or sc-RNA treated cells (**Fig. 76-A**). Characteristic features of Ca^{2+} signaling were analysed for different groups which demonstrated significantly lower number of peaks and amplitude of

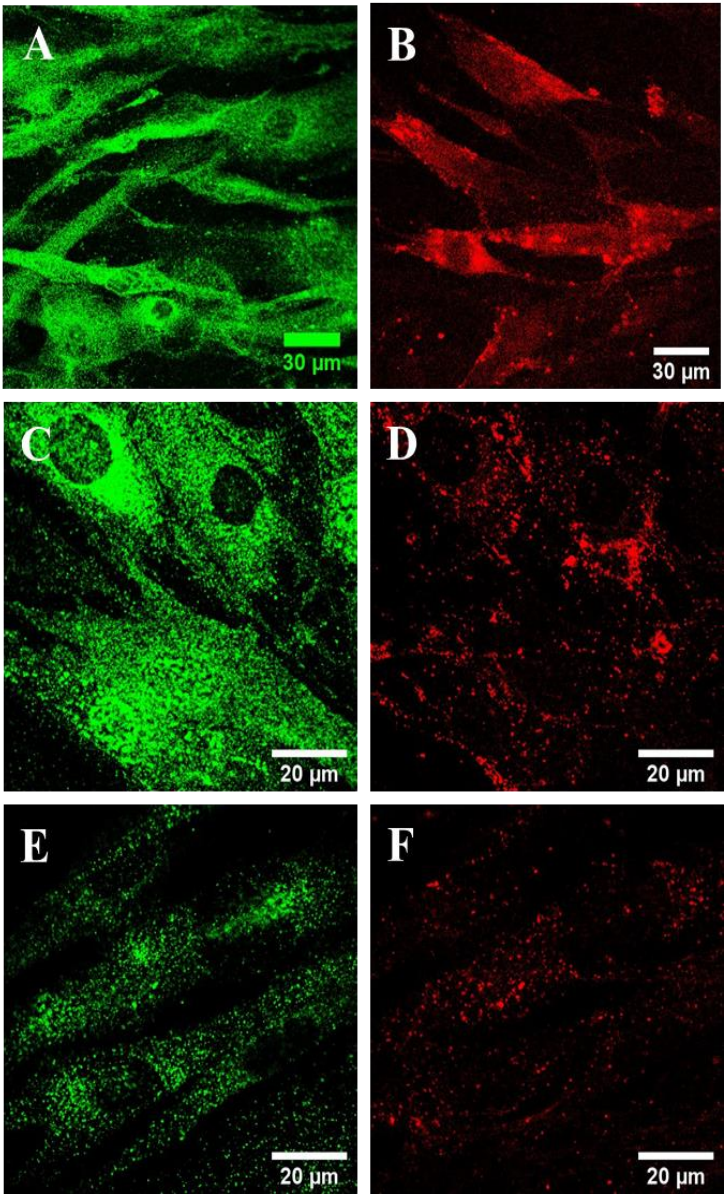
A
30 µm
B
30 µm
C
20 µm
D
20 µm
E
20 µm
F
20 µm

Figure 72. FcRn and Albumin Localization in Subcutaneous $FcRn^{-}$ ADSCs Generated Through Chemical Transfection. Representative image (**A**) shows $FcRn^{+}$ ADSCs, non-transfected experimental group, and image (**B)** shows transfection positive control, cells transfected with TYE563-labelled si-RNA. Image (**C** and **D**) present negative control, cells transfected with sc-RNA and image (**E)** and **F** present $FcRn^{-}$ ADSCs, cells transfected with si-RNA. Image (**A**, **C** and **E,** green) present **c**ells incubated with anti-FcRn antibody at 1:200 and Alexa-Fluor-488 donkey anti-rabbit secondary antibody at 1:400. Image (**D** and **F,** red**)** present cells incubated with Albumin-Alexa-594 (300 μM). 100 nM RNA duplexes were applied for all groups.

oscillations (**Fig. 76-B** and **C** respectively). These data led to the conclusion that ADSCs lacking active FcRn display reduced intracellular albumin content, become inactive for Ca^{2+} signaling and thus justifying the hypothesis that Ca^{2+} signal modulates albumin endocytosis and intracellular accumulation via FcRn.

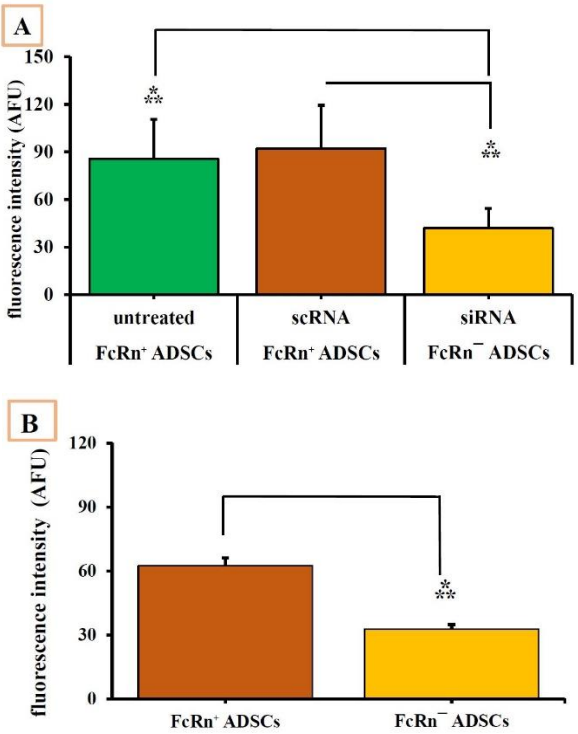

Figure 73. Semiquantitative analysis of intracellular FcRn and Albumin Upon Chemical Transfection With si-RNA Against FcRn. The bar chart (**A**) presents fluorescence intensity for alexa-fluor-488 with antibody directed against FcRn. Each data point represents mean (± SD) of 8 individual experiments. (⁂p= <0.001). The bar chart (**B**) presents fluorescence intensity for Albumin-Alexa-594 in $FcRn^+$ ADSCs and $FcRn^-$ ADSCs. Scaling of the images is as stated on each image. Each data point represents mean (± SD) of 8 individual experiments. (⁂p= <0.001)

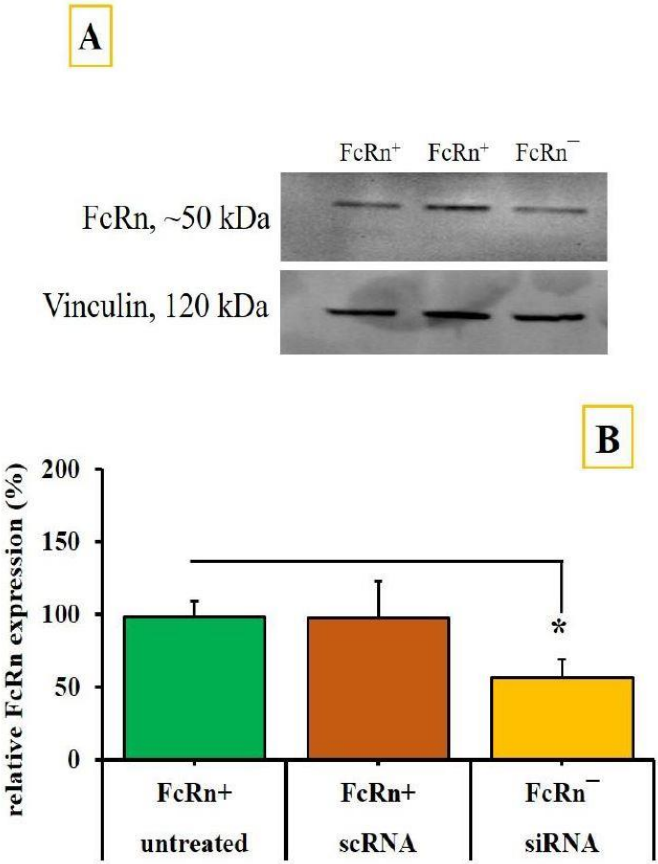

Figure 74. FcRn Protein Expression in FcRn^{-} ADSCs Generated Through Chemical Transfection. **A.** Densitometric analysis of a representative western blot for FcRn (1:2000). Vinculin (1:2000) was used as a reference housekeeping protein (cell ID: ADSC 05). **B.** The bar chart presents difference in FcRn expression in FcRn^{+} and FcRn^{-} ADSCs. Each data point represents mean (± SD) of 3 biological replicates (cell ID: ADSC 05, ADSC 23 and ADSC X), each consisting of 4 technical replicates, *p= <0.05.

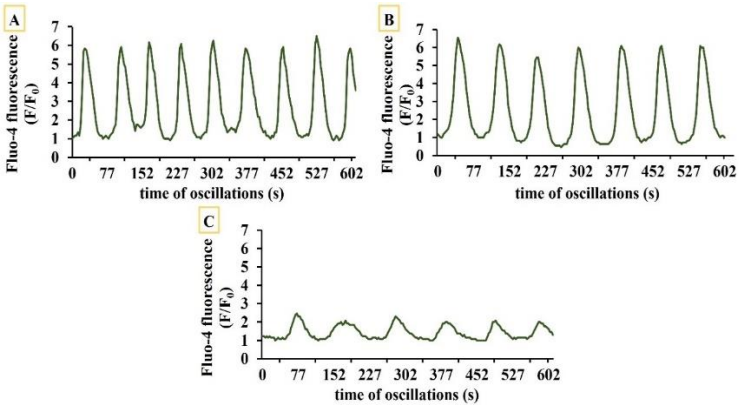

Figure 75. Representative Time Course and Amplitude of Ca^{2+} Oscillations in $FcRn^{+}$ and $FcRn^{-}$ ADSCs Generated through Chemical Transfection. Ca^{2+} oscillations were recoded 48 h post transfection. Representative time course of Ca^{2+} oscillations of $FcRn^{+}$ ADSCs (untreated cells) (**A**), $FcRn^{+}$ ADSCs (sc-RNA treated cells) (**B**), and $FcRn^{-}$ ADSCs (si-RNA treated cells) (**C**).

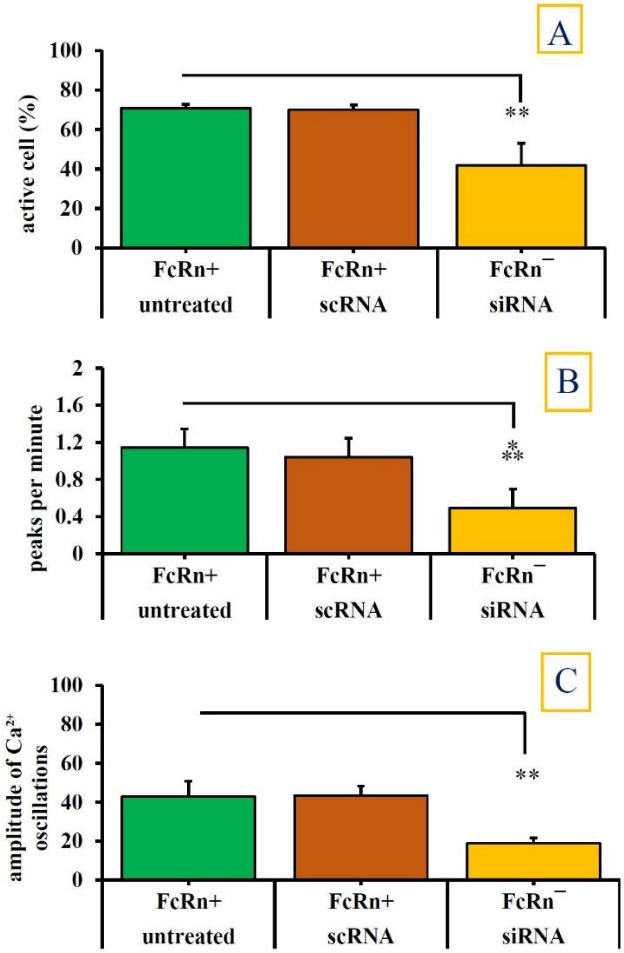

Figure 76. Characteristic Features of Ca^{2+} Oscillations in Chemically Transfected $FcRn^{-}$ ADSCs. Ca^{2+} oscillations in $FcRn^{-}$ ADSCs were compared with $FcRn^{+}$ ADSCs in respect of active cells (%) (**A**), peaks per minute (**B**), amplitude of Ca^{2+} oscillations (**C**). Each data point represents mean (± SD) of 5 individual experiments. (**p = <0.01, ⁂p = <0.001)

4.6.2.3 Antibody Against FcRn

Next generation FcRn blocker *M281* is a recombinant IgG1 monoclonal antibody. It competitively binds with IgG binding sites of FcRn imparting lesser effect on albumin binding (Choudhury et al., 2022). However, there is no specific data available for interaction with albumin binding sites. In this part of the experiment, we intended to investigate how *M281* influences endocytosed albumin content and Ca^{2+} oscillations in subcutaneous ADSCs.

4.6.2.3.1 Effect of *M281* on Albumin and hIgG Endocytosis

Choudhury et al. (2022) incubated with *M281* at 0.03 μg/ml for up to 2 h to block FcRn in human endothelial and villous trophoblast cells. In the present study, ADSCs were preincubated with *M281* for 1 h and then co-incubated with fluorescence-labelled albumin (300 μM) for another h. Subsequently fluorescence intensity was analysed using C-LSM. Our accumulated data presented no detectable downregulation of intracellular albumin for ADSCs incubated with three different concentrations (0.03, 0.06 and 0.09 μg/ml) of *M281* for 1 h (**Fig. 77**). However, preincubation at higher concentrations (5, 15 and 25 μg/ml) resulted in successful downregulation of the intracellular

albumin content presenting a dose-dependent effect on albumin endocytosis (**Fig. 78** and **79**).

Notably, downregulation of the intracellular albumin content was only achieved at 2 h incubation, whereas 1 h with 5 and 15 g/ml *M281* had no inhibitory effect on albumin content in ADSCs. This may indicate that time-dependent ligand receptor binding kinetics may play a crucial role in FcRn-mediated albumin internalization.

M281 blocking of FcRn also resulted in significant dose-dependent downregulation of IgG endocytosis in ADSCs (**Fig. 80** and **81**). In this experiment, ADSCs were preincubated with *M281* (5, 15 and 25 µg/ml) for 2 h. Subsequently they were incubated with hIgG at a dilution factor of 1:300 for 1 h at 37° C and a secondary Alexa Fluor 488-conjugated IgG antibody at a dilution factor of 1:1000 and analysed using C-LSM.

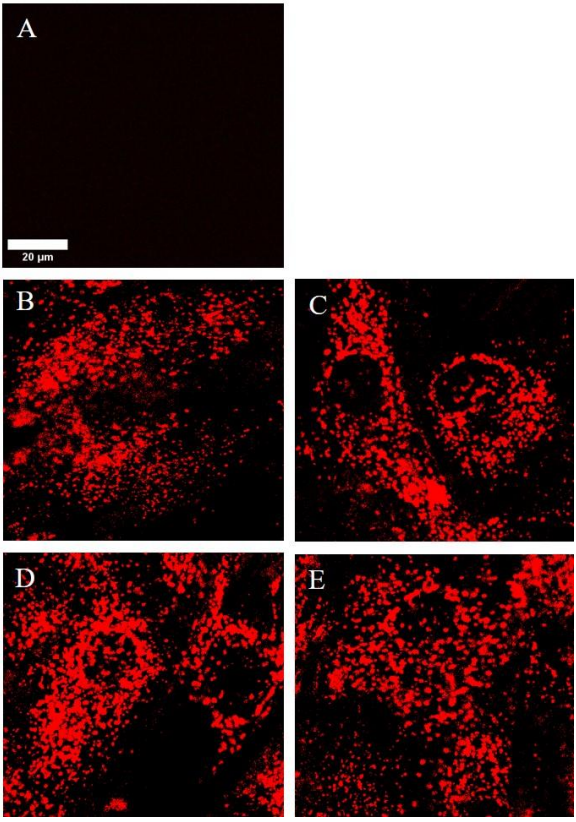

Figure 77. *M281* Effect on Albumin Endocytosis in ADSCs... (continues next page)

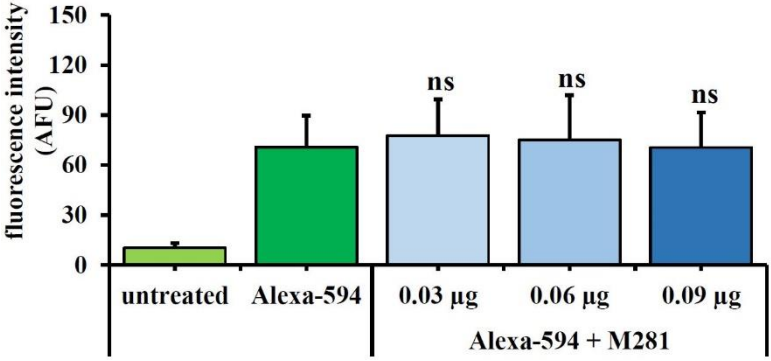

Figure 77. *M281* Effect on Albumin Endocytosis in ADSCs. Shown are representative images from each experimental group of negative control, untreated ADSCs (**A**), positive control, ADSCs incubated with Albumin-Alexa-594 (300 µM) for 1 h (without *M281*) (**B**), ADSCs incubated for 1 h in *M281* (0.03 µg/ml, 0.06 µg/ml and 0.09 µg/ml respectively)-conditioned medium and then co-incubated with Albumin-Alexa-594 (300 µM) in respective *M281*-conditioned medium for 1 h (**C, D** and **E**). The scale bar stated (20 µm) is subjected for all images. The bar chart presents fluorescence differences in treatments. Each data point represents mean (± SD) of 8 individual experiments. (ns = not significant ($p > 0.05$)).

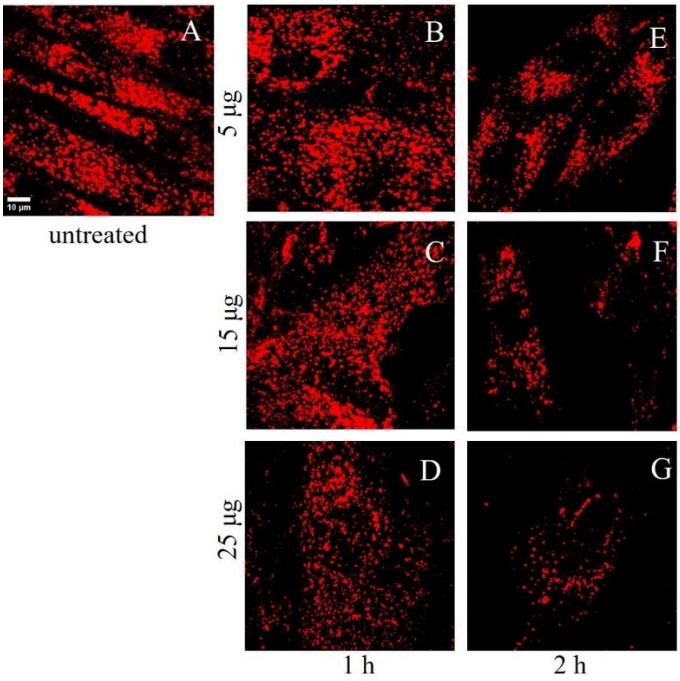

Figure 78. *M281*-mediated Dose Dependent Downregulation of Albumin Endocytosis in ADSCs. Shown are representative images from each experimental group of untreated ADSCs, cells incubated with Albumin-Alexa-594 (300 µM) containing medium for 1 h (without *M281*) (**A**), ADSCs incubated in *M281* (5 µg/ml)-conditioned medium for 1 h and subsequently in *M281* (5 µg/ml)-conditioned medium along with Albumin-Alexa 594 (300 µM) for 1 h (**B**), ADSCs incubated with *M281* (15 µg/ml)-conditioned medium for 1 h and subsequently in *M281* (15 µg/ml)-conditioned medium with Albumin-Alexa-594 (300 µM) for 1 h (**C**), ADSCs incubated in *M281* (25 µg/ml)-conditioned medium for 1 h and subsequently in *M281* (25 µg/ml)-conditioned medium with Albumin-Alexa-594 (300 µM) for 1 h (**D**), ADSCs incubated in *M281* (5 µg/ml)-conditioned

medium for 2 h and subsequently in *M281* (5 µg/ml)-conditioned medium with Albumin-Alexa-594 (300 µM) for 1 h (**E**), ADSCs incubated in *M281* (15 µg/ml)-conditioned medium for 2 h and then in *M281* (15 µg/ml)-conditioned medium with Albumin-Alexa-594 (300 µM) for 1 h (**F**), ADSCs incubated in *M281* (25 µg/ml)-conditioned medium for 2 h and then in *M281* (25 µg/ml)-conditioned medium with Albumin-Alexa-594 (300 µM) for 1 h (**G**). The scale bar stated (10 µm) is subjected for all images.

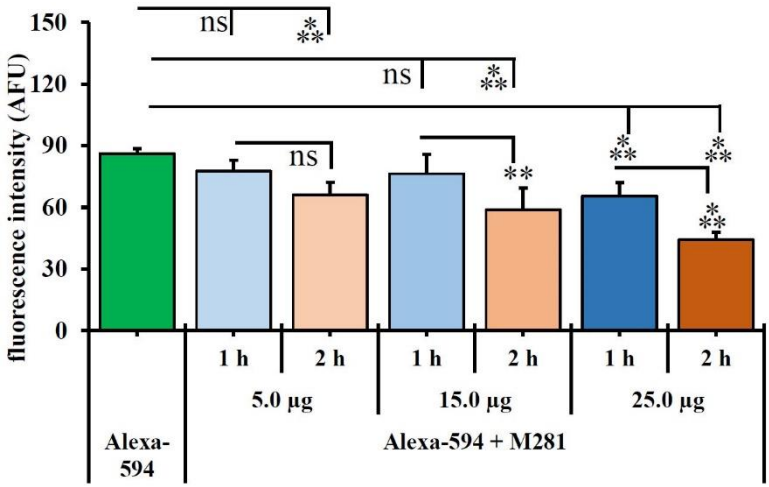

Figure 79. Semiquantitative Analysis of Intracellular Albumin Upon Treatment With *M281*. The Bar Chart Presents Alexa-594 Fluorescence Differences in Groups Presenting *M281*-mediated Dose-dependent Downregulation of Albumin Endocytosis in ADSCs. Each data point represents mean (± SD) of 6 individual experiments. (⁂p = <0.001, **p = <0.01 ns = not significant (p > 0.05)).

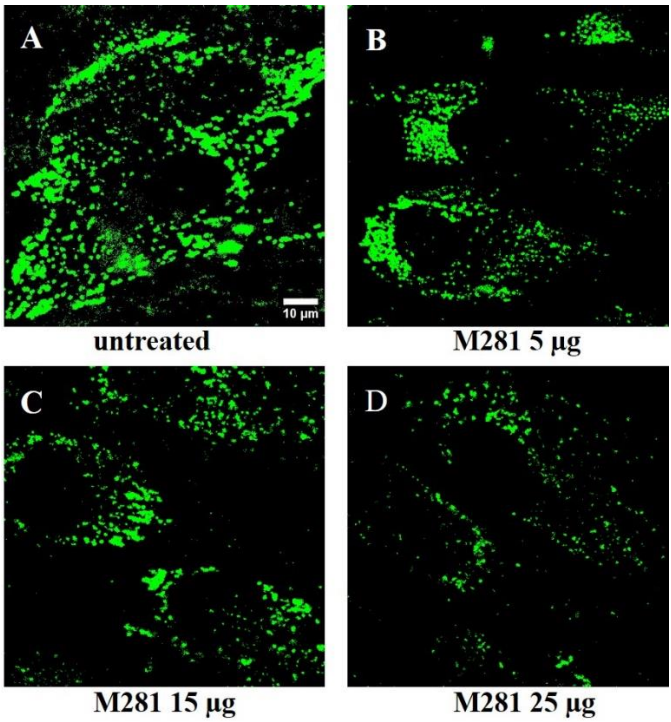

Figure 80. *M281*-mediated Downregulation of hIgG Endocytosis in ADSCs. Shown are representative images from the experimental group of untreated ADSCs (**A**), ADSCs incubated in *M281* (5 µg)-conditioned medium for 2 h in 37° C (**B**), cells incubated in *M281* (15 µg)-conditioned medium for 2 h in 37° C (**C**), cells incubated in *M281* (25 µg)-conditioned medium for 2 h in 37° C (**D**). Sample cells from groups **(A**, **B**, **C** and **D)** were incubated with hIgG (dilution: 1:300, Sigma, cat # I2511) for 1 h, with medium conditioned with *M281* (0.0 µg/ml, 5.0 µg/ml, 15.0 µg/ml and 25.0 µg/ml respectively) and subsequently with anti IgG conjugated with Alexa Fluor 488 (dilution: 1:1000, Invitrogen, cat # A-21208) for 1 h in 37° C. The scale bar stated (10 µm) is subjected for all images.

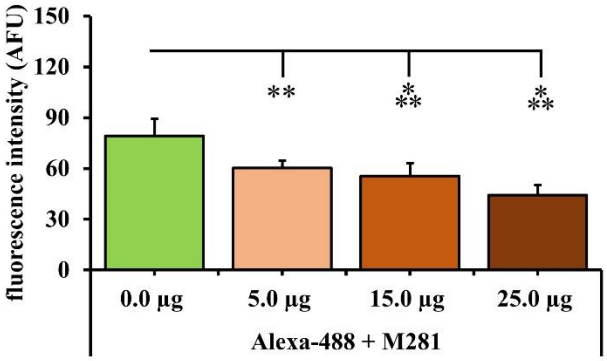

Figure 81. Semiquantitative Analysis of Intracellular hIgG Upon Treatment With Different Doses of *M281*. The bar chart presents Alexa Fluor 488 Fluorescence Differences in ADSCs incubated with *M281*-conditioned Medium. Each data point represents mean (± SD) of 6 individual experiments (**p = <0.01, **p = <0.001).

4.6.2.3.2 Effect of *M281* on Ca^{2+} Oscillations

To analyse *M281* effects on Ca^{2+} signaling, we adopted the protocol described in ***section 3.3***. After initiation of the experiment Ca^{2+} oscillations were observed for ± 5 min and subsequently *M281* was added at different concentrations. Ca^{2+} oscillations were recorded for subsequent ± 10 min and analysed. Our data presented no effect on Ca^{2+} oscillations at 0.03 µg/ml, 0.06 µg/ml, 0.09 µg/ml or 1 µg/ml concentrations of *M281*. With increased concentration (5 µg/ml)

downregulation of Ca^{2+} oscillations was observed in approximately 21% of active cells (**Fig. 82-C**).

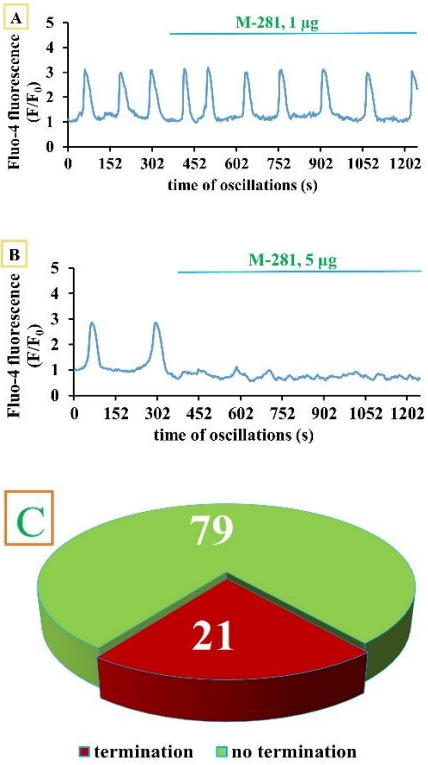

Figure 82. Downregulation of Ca^{2+} Oscillations in *M281*-treated Subcutaneous ADSCs. *M281* was added with the culture media after ± 5 min and investigated for effects on Ca^{2+} oscillations. Representative time course of Ca^{2+} oscillations in *M281* (1 µg/ml)-treated ADSCs (**A**), *M281* (5 µg/ml)-treated ADSCs (**B**). The pie chart (**C**) presents percentage of ADSCs in which Ca^{2+} oscillations were terminated by *M281* (5 µg/ml). (n= 7 individual experiments with 65 ± 14 cells from each experiment).

In the next phase of this experiment, we preincubated ADSCs with *M281* (25 µg/ml) for 1 and 2 h and analysed for Ca^{2+} oscillations following the previously described protocol and recorded for about 15 min. Both time-groups presented successful downregulation in Ca^{2+} oscillations compared to the untreated group (**Fig. 83-A-C**). Our data demonstrated time-dependent downregulation of oscillating cells. The bar chart in figure (**Fig. 83-D**) demonstrated significantly (⁂p = <0.001) higher termination of Ca^{2+} oscillations in cells with 2 h pre-incubation as compared with the 1 h incubation group.

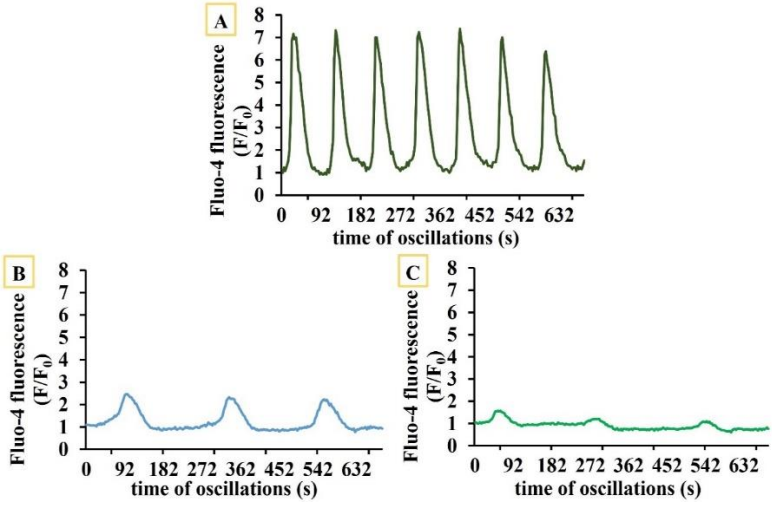

Figure 83. Time-dependent Downregulation of Ca^{2+} Oscillations in *M281*-treated Subcutaneous ADSCs… (continues next page)

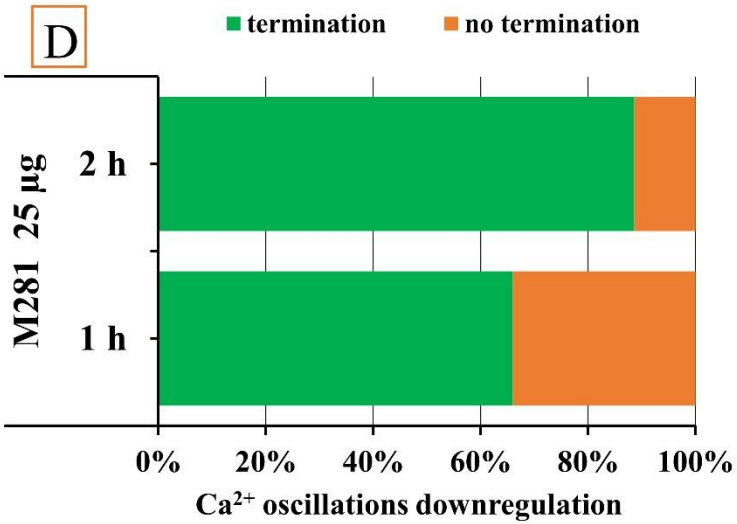

Figure 83. Time-dependent Downregulation of Ca^{2+} Oscillations in *M281*-treated Subcutaneous ADSCs. Ca^{2+} oscillations were investigated using Fluo-4, AM (10 µM). Treated group was incubated in *M281* (25 µg/ml)-conditioned medium throughout the Ca^{2+} oscillations experiment. Representative time course of Ca^{2+} oscillations in untreated ADSCs (*M281*, 0.0 µg) (**A**), cells incubated in *M281* (25 µg)-conditioned medium for 1 h at 37° C (**B**), and cells incubated in *M281* (25 µg)-conditioned medium for 2 h at 37° C (**C**). The bar chart presents downregulation (%) of Ca^{2+} oscillations by *M281* at different incubation periods. Ca^{2+} oscillations in ADSCs following 2 h preincubation with *M281* (25 µg/ml) were significantly more strongly terminated than in 1 h incubation group. (n = 12 individual experiments comprising 87 ± 7 cells from each experiment, significance level is ⁂p = <0.001)

5. Discussion

Comparatively low invasive isolation process (Zuk et al., 2001), promising immunomodulatory properties (Al-Ghadban & Bunnell, 2020), high differentiation capacity, and their cargo transportation potential (Litvinova et al., 2022) made ADSCs appreciated as an important player in regenerative medicine and stem cell therapeutics. Albumin, being one of the most abundant proteins in blood serum and nutrient carrier, poses immense potential for drug delivery (Karami et al., 2024). Albumin was described to be internalized by different mechanisms depending on cell types, however, very little is known about albumin endocytosis in ADSCs. H. Sun et al. (2022) described clathrin and caveolin-mediated albumin endocytosis in ADSCs, but their association to intracellular Ca^{2+} oscillations and relation to FcRn remain unexplored. The goal of this study was to illustrate albumin endocytosis via different pathways, interference of FcRn and role of Ca^{2+} as an intracellular messenger (Fig. 78). Our study revealed no differences in Ca^{2+} signaling or albumin endocytosis between ADSCs obtained from subcutaneous and visceral

tissues. Consequently, subsequent experiments were conducted using ADSCs derived from subcutaneous tissue.

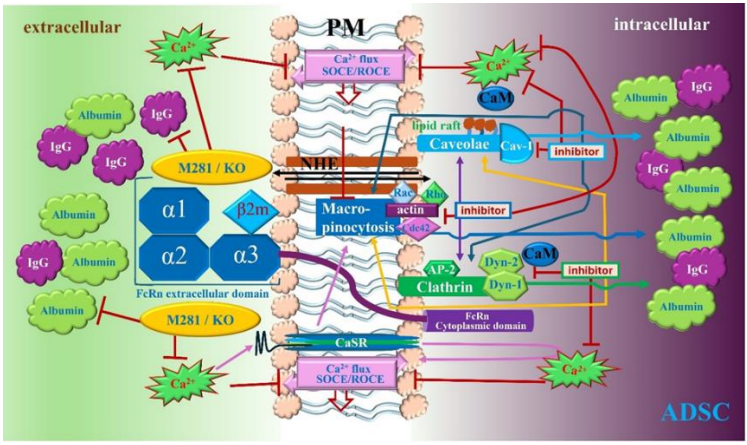

Figure 84. Graphical Abstract: A Comprehensive Schematic Representation of the Bidirectional Relationship Between Ca^{2+} Signaling and Albumin/IgG Endocytosis in ADSCs, Emphasizing the Role of Ca^{2+} Signaling in FcRn-mediated Albumin Homeostasis.

In the graphical presentation (**Fig. 84**) ligand trafficking through the PM employs three major pathways: macropinocytosis, CDE, and CME. The CDE endocytosis employs lipid raft-rich caveolae and Cav-1 protein. Macropinocytosis is mediated by Rac, Rho, Cdc42, actin, and NHE proteins. The CME pathway is maintained by clathrin-coated vesicles, which are aided by AP-2, Dyn-1,

and Dyn-2 proteins. On the extracellular side, albumin and IgG are the major ligands that approach the ADSC membrane. In a normal cellular environment, the binding of these ligands to FcRn stimulates Ca^{2+} flux through SOCE and ROCE. This Ca^{2+} signaling is regulated by CaM and CaSR expression. *M281* complexed with FcRn limits IgG binding to its β2m domain and albumin binding to its α2/α3 domain, which in turn downregulates Ca^{2+} flux through the PM. FcRn-deficient cells suppressed Ca^{2+} oscillations and albumin store. Inhibitors of endocytosis pathways not only block endocytosis but also block CaM, which downregulates Ca^{2+} signaling, and cells compensate by stimulating alternative endocytosis pathways. In contrast, inhibitors of Ca^{2+} channels and CaSR also block endocytosis.

5.1 Ca^{2+} Oscillations are Dependent on the Albumin, IgG and FcRn Levels

Albumin-mediated activation of the PI3/Akt/SGK1 signaling pathway leads to Na^+ transport in fetal distal lung epithelial (FDLE) cells without affecting Na^+/K^+-ATPase

activity and mRNA expression of Na^+ transporter proteins (Laube & Thome, 2022). Similar pathways may involve Ca^{2+} transport. Our data suggested that spontaneous Ca^{2+} oscillations in ADSCs are dependent on FBS in the cell culture medium and could be triggered by albumin (fraction V, bovine origin). Hooper et al. (2005) described albumin (pure and fraction V) as a potent inducer of Ca^{2+} oscillations in microglial cells but not in astrocytes or macrophages which was mediated by phospholipase C and Src tyrosine kinase. Our study demonstrated IgG-mediated induction of Ca^{2+} signaling in ADSCs which supports studies on IgG triggered FcγRIIIb-dependent increase of cytoplasmic Ca^{2+} concentration in human neutrophils (Marois et al., 2011) and increased Ca^{2+} influx in IgG-treated mouse primary hippocampal neuronal cells (Aysit-Altuncu et al., 2018). A recent study demonstrated increased Ca^{2+} influx by SOCE in IgG^+ mouse B cells and downregulated by Miz1 through anti-apoptotic protein Transmembrane BAX Inhibitor Motif Containing 4 (Tmbim4) (L. Zhang et al., 2024). Moreover, addition of stimulatory FcRn antibody to the incubation medium triggered Ca^{2+} oscillations in ADSCs. Since FcRn protects albumin and IgG from the proteolytic environment and lysosomal degradation (Peter et al., 2020), we

hypothesized that FcRn involves Ca^{2+} signals to increase albumin and/or IgG trafficking or in other pathways modulated by FcRn.

5.2 Albumin Uptake in ADSCs Involves Diverse Pathways

Albumin internalization was described by many studies in many cell types to occur via different pathways. However, it was not sufficiently described for ADSCs. We confirmed the observation of H. Sun et al. (2022) using established inhibitors of caveolae- and clathrin-mediated endocytosis for albumin and additionally found evidence for macropinocytosis in ADSCs. Studies from others demonstrated that a certain portion of overall endocytosed albumin was internalized by macropinocytosis in rodent pulmonary endothelial cells, while involving both clathrin-mediated and caveolae-dependent/cav-1-independent endocytosis (Li et al., 2013).

5.2.1 Macropinocytosis

In macrophages albumin internalization was described to occur by macropinocytosis in FcRn-independent manner, however, rapid degradation was observed. Upon colocalization with sorting nexins (SNX)- positive membrane domain in presence of FcRn albumin was rescued (Toh et al., 2019). The lysosomal glutamine and asparagine signaling is linked by Rag GTPase-independent transporter SNAT7 that activates mTORC1 by macropinocytosis-mediated albumin uptake to perpetuate K-RAS-driven cancer cell growth in pancreatic cancer (Meng et al., 2022). Additionally, it was shown that albumin activates cell surface receptors to initiate K-RAS-dependent macropinocytosis in lung and pancreatic cancer cells. This is of clinical importance since this pathway enables cancer cells with K-RAS mutations to transport extracellular protein into intracellular amino acid pathways to support their unique metabolic needs (Sutton et al., 2022). Our data demonstrated that interfering macropinocytosis by manipulating NHE protein family using *EIPA* (amiloride) inhibited albumin endocytosis in ADSCs. Macropinocytosis is also associated to cancer metastasis since actin-dependent cytoskeletal rearrangement occurs through receptor tyrosine

kinase AXL activated by GAS6 and leads to membrane ruffling and rapid macropinocytic internalization of AXL-GAS6 complex via PI3k/Akt signaling pathway (Poswiata et al., 2022; Zdzalik-Bielecka et al., 2021). Beauvericin, isolated from a soil-borne fungus, inhibited actin polymerization and blocked kinase activity of Src via STAT3, leading to apoptosis of various cancer cells (Kim et al., 2023). Combined cell therapy with ADSCs and platelet-rich plasma induced proliferation of endothelial cells via elevated expression of VEGF, p-STAT3, and SDF-1 in diabetic wound healing (Ni et al., 2021). ADSCs-derived EVs-conditioned medium expressed higher levels of Src, and ADSC-EV-supplemented blastocytes presented higher CDK1 activated by Akt (Bang et al., 2024). ADSCs-derived NVs and EVs increased interleukin-8 expression to promote angiogenesis by activating CREB, AP-1 proteins and NF-κB signaling pathways (Wu et al., 2021). ADSCs-derived exosomes mediated increased expression of miR21-5p via PI3k/p-Akt signaling activation and PTEN inhibition leading to in vivo angiogenesis that can be enhanced by co-culture with human iPSCs-derived cardiomyocytes on biodegradable polymer scaffold (D. Sun et al., 2022; J. Zhang et al., 2024). Our data demonstrated reduced albumin

endocytosis by blocking actin polymerization and depolymerization using *CD* and the PI3k antagonist *Won* in ADSCs, but no effect with Imipramine treatment that inhibits membrane ruffling during macropinocytosis was observed. ADSCs co-cultured with platelet-rich plasma induced wound healing through collagen deposition, granulation formation and re-epithelialization by increasing the expression of Rac, Rho, Cdc42 GTPases (Zhang et al., 2019). Potentially, Cdc42 could be a target for the treatment of type 1 diabetes mellitus since it can induce ADSCs-derived insulin producing cell proliferation and insulin secretion via the Wnt/β-catenin pathway (Xiao et al., 2019). Our accumulated data manifested pronounced downregulation of albumin endocytosis upon blocking the Rac/Rho/Cdc42 pathway using the potent inhibitor *MBQ-167*.

5.2.2 Caveolae-mediated Endocytosis

Human podocytes actively transport albumin through caveolae-mediated endocytosis across the glomerular basal membrane independent of clathrin (Dobrinskikh et al., 2014; Moriyama et al., 2021). Albumin-based therapeutic drug delivery depends on cav-1, the structural component of

caveolae-mediated endocytosis, in human breast, pancreatic and lung cancers (Chatterjee et al., 2017). Myogenic differentiation of ADSCs was enhanced by downregulation of cav-1 via miR-124-3p which can be applied in pelvic floor dysfunction treatment (Chen et al., 2021). ADSCs can differentiate into dopaminergic-like neuronal cells, degenerated in Parkinson's disease, by downregulating cav-1 and increased expression of Nurr1, Lmx1a and tyrosine hydroxylase (Han et al., 2021). In the experiments of the present study, we observed expression and colocalization of fluorophore-labelled albumin with cav-1, and endocytotic uptake of cav-1 dependent Lac-Cer-albumin conjugate in ADSCs. Lac-Cer-albumin endocytosis was arrested by *Gen* confirming the involvement of caveolae-mediated endocytosis.

5.2.3 Clathrin-mediated Endocytosis

In the present study *CPZ*, which has previously been shown to inhibit clathrin-mediated endocytosis failed to inhibit albumin uptake in ADSCs. *CPZ* is an antipsychotic drug, which was previously proposed to inhibit the adapter protein (AP-2) involved in formation of clathrin coated vesicles

(CCVs) via μ-2 subunit (Yao et al., 2002). It should be noted that *CPZ* significantly decreased cell viability of some cell lines even after short incubation (Vercauteren et al., 2010) which may explain the absence of albumin endocytosis observed in the present study. On the contrary, Daniel et al. (2015) found no interaction between *CPZ* with AP-2. Amyloid-β internalization into brain endothelial cells by clathrin-mediated endocytosis depends on dynamin-II, which does not involve dynamin-I or dynamin-III (Du et al., 2021). Hence, we deployed *Dyngo-4a*, which inhibits dynamin I- and II-dependent endocytosis (McCluskey et al., 2013) and found evidence for downregulation of clathrin-mediated endocytosis of albumin. Dynamin/GTP-binding proteins initiate vesicular curvature and facilitate final scission of the CCVs from the PM (Cheng et al., 2021). Clathrin-mediated albumin endocytosis depends on distinct binding affinity in the PT where cubilin/amnionless helps binding at high-affinity sites and megalin at low-affinity sites (Ren et al., 2020). Megalin-dependent albumin endocytosis via PI3K/mTORC2 activation in endothelial cells of PT is positively regulated by albumin-mediated Akt activation (Silva-Aguiar et al., 2022). Our experiment demonstrated expression of megalin and colocalization with fluorochrome-

labelled albumin suggesting megalin-dependent albumin trafficking in ADSCs. Upon binding with albumin, megalin and cubilin induce adaptor protein Dab2 to initiate clathrin-dependent albumin endocytosis in the kidney PT (Rbaibi et al., 2023). However, Bento-Abreu et al. (2009) demonstrated that albumin endocytosis is directed by megalin-mediated recruitment of adaptor protein Dab1 associated with cav-1/-2 in cultured astrocytes.

5.3 Interplay of Different Endocytotic Pathways

We observed that inhibitors of specific endocytotic pathways did not completely inhibit albumin endocytosis in ADSCs, indicating that albumin endocytosis occurs simultaneously through different endocytotic mechanisms. For instance, β-2 subunit of AP-2 can bind with two different sites (clathrin box and arrestin-2L binding site) on clathrin N-terminal domain (Muenzner et al., 2017) and cells lacking μ-2 subunit of AP-2 are unable to form CCVs and have a propensity to deploy alternative endocytic pathways (Tobys et al., 2021). Interestingly, dynamin is pertinent to both caveola- and clathrin-mediated endocytosis since GTP-dependent

caveolar scission from the PM is inhibited in anti-dynamin-IgG-treated endothelial cells (Henley et al., 1998; Oh et al., 1998). We therefore co-incubated ADSCs with inhibitors of different endocytotic pathways, in particular *Won* or *EIPA* targeting macropinocytosis concomitant with *Gen* or *Nyn* as inhibitors of caveolae-dependent endocytosis. All these treatment regimens resulted in around two-fold inhibitory effects on albumin endocytotsis and substantiated the notion that different endocytotic pathways are substituted when one maybe blocked or perform parallelly in ADSCs.

5.4 Ca^{2+} Signals Orchestrate Albumin Uptake in ADSCs

In the current study, we investigated the relationship between intracellular Ca^{2+} oscillations in ADSCs and albumin endocytosis. Albumin possesses at least thirty negatively charged Ca^{2+} binding sites (Patel et al., 2022) underscoring the role of albumin in Ca^{2+} signaling pathways which may affect albumin trafficking. To test this hypothesis, we investigated internalization of Ca^{2+} -treated albumin in ADSCs devoid of intracellular Ca^{2+} store. Our data suggested that Ca^{2+} (1 mM) participates in modulating

albumin endocytosis in ADSCs both extracellularly and intracellularly which is consistent with the Ni^{2+}/thapsigargin-mediated inhibition of endocytosis in primitive endodermal cells differentiated from mouse embryonic stem cells (Sauer et al., 1998) and *BAPTA*-mediated Ca^{2+} scavenging abolishment of endocytosis in nerve terminals (Wu et al., 2014). Intracellular Ca^{2+} buffering terminates oscillations in astrocytes, microglia, ADSCs, and HEK cells (Skupin et al., 2008) and the downregulation of Ca^{2+} diffusion restricts the propagation of spiking to unstimulated areas in astrocytes (Moshkforoush et al., 2021). The Ca^{2+} influx or calmodulin (CaM)-mediated trigger and regulation of endocytotic pathways is thoroughly documented in phagocytic cells, secretory cells and nerve terminals (Wu et al., 2014), but only a few reports exist which demonstrate Ca^{2+}-dependence of endocytosis in non-excitable cells which lack voltage-activated Ca^{2+} channels.

5.4.1 Ca^{2+} Governs Caveolae-dependent Albumin Endocytosis

Caveola-dependent endocytosis related proteins have been demonstrated to be modulated by Ca^{2+} signaling in many cell types in different studies with clinical consequences. Overexpression of cav-1 enhances SOCE via caveolar ORAI1 (calcium release-activated calcium channel protein 1) independent of SOCE regulatory protein, STIM1 (stromal interaction molecule 1) volume in airway smooth muscle cells (Prakash et al., 2007; Sathish et al., 2012). Intralipid upregulated cav-2 phosphorylation of STAT3 and GSK-3β in response to higher Ca^{2+} retention (Li et al., 2017). Increased CaMKII expression and intracellular Ca^{2+} signals accompanied by higher calpain activity were observed in cav-3-depleted mouse myoblasts, suggesting Ca^{2+} correlation with cav-3 (Matsunobe et al., 2022). Overexpressed cavin-4 interacts with STIM1 via HR1 domain to mediate SOCE-induced Ca^{2+} influx in cardiomyocytes (Malette et al., 2019). *Nyn* targets lipid-rich caveolae, and *Gen*, a tyrosine kinase inhibitor that blocks cav-1-phosphorylation, induce the overexpression of CaM-1 in rats (Synowiec et al., 2023; Vera et al., 2007). In another investigation, *Gen* was found to concert calcium/phosphate

homeostasis via Akt signaling in a rodent model (Zivanovic et al., 2022). The microtubule blocker *Noco* increases cytosolic Ca^{2+} transients by impeding glycine receptors in cerebral astrocytes (Morais et al., 2017). We demonstrated that *Noco* downregulated albumin internalization but failed to interfere with Ca^{2+} signaling in human ADSCs, whereas other caveolae-dependent endocytosis inhibitors such as *Nyn* and *Gen* exerted 44% and 69% downregulation of Ca^{2+} oscillations, respectively. *Noco* disrupts the assembly and disassembly of microtubules, leading to the loss of morphological caveolae and thereby inhibits caveolae-dependent endocytosis in endothelial cells (Head et al., 2006; Sun et al., 2010), Sun SW et al.; 2010).

5.4.2 Receptor-mediated Endocytosis is Distinctly Modulated by Ca^{2+}

The modulation of store-operated Ca^{2+} channels (SOCCs) is coordinated by AMN/STIM1/ORAI1-3 channels, which were illustrated to synchronize receptor-mediated (clathrin-dependent) endocytosis in kidney PT epithelial cells (Wang et al., 2017; Zeng et al., 2017). Clathrin light chains have conserved Ca^{2+} binding sites that show structural

resemblance with Ca^{2+} binding sites on CaM, suggesting that cytosolic Ca^{2+} may modulate clathrin CCV formation (Nathke et al., 1990). Dynamin-related protein 1 (Drp1) assembly and phosphorylation in mitochondria is regulated by Ca^{2+} flux across endoplasmic reticulum and mitochondria in breast carcinoma cells (Chen et al., 2023). A recent study presented Drp1-mediated cardiac contractility and Ca^{2+} flux regulation coupled with the level of ROS and mitochondrial Ca^{2+} retention capacity in cardiomyocytes, indicating Drp1 as a potent therapeutic target in ischemia/reperfusion (IR) injury (Piao et al., 2024). Increased Ca^{2+} deposition in the corticomedullary junction decreases the albumin receptor complex megalin/cubilin in the renal PT of morbus Dent-1 patients with CLCN5 mutated gene (Zhai et al., 2022). Syndapin1 helps dynamin 1 to be de/phosphorylated by the Ca^{2+}/CaM-dependent phosphatase calcineurin which is predicted to facilitate CCVs scission (Anggono et al., 2006). Dynamin 1 phosphorylation confers a 12-fold increase in GTPase activity, and fluctuations in GTPase activity depend on de/phosphorylation by protein kinase C (Hinshaw, 2000). This may result in increased expression of cortical Drp1 and NCX1 (Na^{+} /Ca^{2+} exchanger1) at 1 h post-mTBI (post-mild traumatic brain injury), the former decreased at 24 h,

interestingly, both restored to control levels at 5 days post-mTBI and increasing Drp1 attenuated oxidative stress (Omelchenko et al., 2019). In our study, blocking dynamin by *Dyngo-4a* confered non-significant downregulation of Ca^{2+} signaling in ADSCs; however, blocking CCVs formation by *CPZ* resulted in substantial Ca^{2+} signal suppression, suggesting that Ca^{2+} participates in clathrin recruitment prior to dynamin, which modulates CCVs fission from the PM.

5.4.3 Ca^{2+} Signaling Plays a Conclusive Role in Macropinocytosis

Macropinocytosis-mediated nutrient uptake occurs in diverse cell types by stimulation with growth factors or stress signal such as in mouse embryonic fibroblasts (Ard et al., 2015) and cancer cells (Redelman-Sidi et al., 2018), but in selected cell types, notably dendritic cells and macrophages, macropinocytosis occurs constitutively. However, a combined approach involving both stimulus-induced macropinocytosis and constitutive macropinocytosis has been suggested to internalize low-density lipoproteins in macrophages (Doodnauth et al., 2019). Previous studies have demonstrated that constitutive macropinocytosis is

stringently Ca^{2+}-dependent, where extracellular Ca^{2+} stimulates the macropinocytosis-related protein Rac/Cdc42 through CaSR (Canton et al., 2016). Expression and function of CaSR has been discussed in human adipocytes and adipocyte progenitor cells (Cifuentes et al., 2005), human aortic smooth muscle cells (Molostvov et al., 2007), rodent cardiac fibroblasts (Zhang et al., 2014), as well as in human ADSCs (Yanai et al., 2019). The data of the present study therefore suggests that Ca^{2+}-mediated albumin endocytotic pathways in ADSCs are constitutive and involve intracellular Ca^{2+}, SOCE and CaSR, since the intracellular Ca^{2+} chelator *BAPTA*, the SOCE inhibitor *SKF-96365* and the CaSR antagonist *NPS-2143* inhibited Ca^{2+} oscillations.

Of note, the suppression of Ca^{2+} oscillations in ADSCs likewise attenuated albumin internalization, highlighting that the endocytotic pathways rely on Ca^{2+} signaling. This conclusion was validated by the finding that intervention with contrasting pinocytotic processes in ADSCs resulted in downregulated Ca^{2+} oscillations. Interestingly, while the macropinocytosis inhibitor *MBQ-167* was effectively downregulated albumin endocytosis, it did not manage to inhibit Ca^{2+} oscillations. This observation suggests Ca^{2+} involvement in endocytosis upstream of Rac/Cdc42

signaling since *MBQ-167* is a well-described Rac/Cdc42 antagonist. Rho, Rac and Cdc42 are documented as the key players in actin polymerization to form MPS (Tapon & Hall, 1997). RAS protein activation by macropinocytic inducers initiates signaling cascades involving Rac1/PI3Ks and their downstream effectors, thus leading to actin cytoskeleton remodelling for PM ruffles and MPS formation (Y. Wu et al., 2024). Several studies demonstrated that Ca^{2+} signals independently trigger and regulate actin polymerization in forming the nucleoskeleton in fibroblasts (Safaralizade et al., 2021; Ulferts & Grosse, 2024), in forming myelin sheaths composed of actin filaments in oligodendrocytes (Iyer et al., 2024) and in damage-induced mitochondrial actin polymerization through Na^{+}/Ca^{2+} exchanger (Fung et al., 2022). In the present study, *CD*, an inhibitor of actin polymerization, interfered with both Ca^{2+} oscillations and albumin endocytosis, highlighting that macropinocytosis is dependent on an intact actin network and is modulated by Ca^{2+} signaling. A recent study in a macrophage cell line demonstrated that STIM1/ORAI1-dependent Ca^{2+} influx through SOCE initiates phagocytosis, modulates phagosome formation by activating Rac1/F-actin and its translocation via the CaM-dependent phosphorylation of the myosin-II

light chain (S. Yang et al., 2023). This corroborates with the myosin-driven microtubule networking with actin during phagosome maturation (G. Lee et al., 2021) and intracellular Ca^{2+} concentration-dependent phagosome fusion with lysosome during late phase of phagocytosis (Mukherjee et al., 2020).

5.5 Ca^{2+} Modulates FcRn Binding to Albumin and IgG

FcRn undergoes continuous endocytosis from the PM and is subsequently recycled back (D'Hooghe et al., 2017). Typically, following internalization into cells, endocytosed albumin and IgG are conserved from lysosomal degradation through FcRn-mediated exocytosis. Albumin binds more strongly to FcRn in the acidic environment of endosomes than in the neutral pH of extracellular fluids, and the interaction is hydrophobic (Sand et al., 2014). The involvement of FcRn in caveolae and caveolae-mediated endocytosis has not been thoroughly characterized, unlike receptor-mediated endocytosis and macropinocytosis. The activity of lipid-conjugated antisense oligonucleotides that

utilize albumin as a carrier is attenuated in Cav1-deficient and FcRn-deficient mice but not in albumin-deficient mice. Circulating albumin levels were reduced by 40% in FcRn-deficient mice, whereas concentrations of plasma proteins were upregulated in albumin-deficient mice (Chappell et al., 2020), suggesting FcRn mediated albumin internalization may involve caveolae.

Moreover, considerable studies have indicated FcRn participation in both clathrin-mediated endocytosis and macropinocytosis. A few studies have demonstrated the colocalization of megalin adaptor Dab2 with megalin and FcRn, excluding cubulin involvement, during albumin internalization in murine mesangial cells (Bryniarski et al., 2020) and in Opossum kidney PT cells as well as rat endothelial cells (Dahlke et al., 2022), suggesting that FcRn plays a role in clathrin-mediated endocytosis. Both albumin and IgG were internalized by macropinocytosis in primary mouse bone marrow-derived macrophages expressing hFcRn, which colocalized with sorting nexin 5 (SNX5) which generates tubular extension and subsequently encapsulated into tubules emerging from the early MPS to transport carriers to the PM (Toh et al., 2019). Recent research has further demonstrated parallel association

between macropinocytosis and FcRn in primary human endothelial cells, where HSA was found to colocalize with FcRn in tubules originating from maturing MPS, which are then transported towards the PM (Pannek et al., 2023).

Ca^{2+} facilitates CaM binding to FcRn in the IgG endocytosis pathway in human intestinal epithelial cells (Dickinson et al., 2008). FcRn-mediated IgG endocytosis increased Ca^{2+}/CaM-dependent protein kinase IV (CaMKIV) and CD86 expressions in human kidney podocytes (Ichinose et al., 2016). Similar pathways may be involved in albumin internalization by FcRn. FcRn was presented across all age groups of our ADSCs cell lines which was confirmed by western blot and colocalized with endocytosed fluorescence-labelled albumin. Considering these outcomes and our data that Ca^{2+} oscillations were elicited by albumin and IgG, we hypothesized that Ca^{2+} signals may mobilize FcRn-mediated albumin and IgG trafficking as well as recycling in ADSCs. To test this hypothesis, we generated si-RNA-mediated FcRn-deficient hADSC cell lines through both electroporation and chemical transfection, tested for albumin endocytosis, and characterized Ca^{2+} oscillation patterns compared with wild-type cells. FcRn downregulation was

confirmed using immunocytochemistry and western blotting.

The accumulated data from this study demonstrated that si-RNA-mediated FcRn downregulation, achieved through both electroporation and chemical transfection, significantly decreased albumin endocytosis in ADSCs. We observed that FcRn knockdown simultaneously led to a remarkable reduction in the proportion of cells exhibiting Ca^{2+} oscillations, as well as in the amplitude and frequency of Ca^{2+} signaling in the remaining active cells, suggesting that the intracellular Ca^{2+} signaling network is associated with FcRn presentation. Global Ca^{2+} oscillations result from a cycle of irregularly occurring global Ca^{2+} spikes, suggesting that IP_3-evoked oscillations are sequences of stochastic spikes in astrocytes, microglia, ADSCs, and HEK cells. A decrease in amplitude resulted from disproportionate Ca^{2+} release and reuptake during interspike interval (ISI) immediately after stimulation of a spike. Subsequently, during the stationary phase of oscillations, Ca^{2+} uptake by stores during the ISI matches the amount released during the successive spike and the two fluxes are balanced (Skupin et al., 2008). Purinergic receptor activation encodes the amplitude and duration of ATP-induced Ca^{2+} oscillations,

which are regulated by CD39-mediated rapid ATP hydrolysis that limits Ca^{2+} transients, leading to microglial migration, while large and sustained transients are needed for cytokine responses (Chun et al., 2022).

Spontaneous Ca^{2+} local transients (SCaLTs) are modulated by SOCE, NCX, Ca^{2+}-ATPases, and Ca^{2+}-induced Ca^{2+} release through IP_3-receptors (IP_3-R) and ryanodine receptors. Computational simulation of SCaLTs histograms obtained from multiple models suggested that relaxed baseline oscillations could be due to the declined IP_3-R aggregation and blocking each flux downregulates SCaLTs' frequency (Oprea et al., 2022). In the current study, reduced frequency of Ca^{2+} spike in FcRn-deficient ADSCs may result from impairing either of these Ca^{2+} fluxes or deceleration of IP3-R clustering. After the recovery from the inhibitory effect, which ceased the previous Ca^{2+} spike and completed the refractory phase of the previous spike, a new spike was initiated, leading to a spike cluster (Friedhoff et al., 2023). A model was proposed for fast numerical simulations to derive analytical expressions for the rate of Ca^{2+} spiking, coefficient of variation of the ISI, and ISI density approximation (Ramlow et al., 2023).

These findings suggest that FcRn is crucial for the endocytotic pathway and albumin binding to the FcRn is Ca^{2+}-dependent. To validate these data, we incubated ADSCs with the FcRn-inactivating antibody *M281* to examine the impact on Ca^{2+} oscillations, as well as on the endocytosis of albumin and IgG. As expected, the results demonstrated remarkable dose-dependent downregulation of Ca^{2+} signaling and internalization of both proteins authenticating our findings in FcRn-deficient ADSCs. It is noteworthy that various antibodies targeting the IgG binding site of FcRn have been studied to reduce circulating autoimmune antibodies, leading to diminish serum albumin levels. This effect may be attributed to enhanced FcRn degradation and/or steric hindrance of the albumin binding site on FcRn (Ma et al., 2024). Moreover, *M281* treatment reduced serum IgG and all subclasses of IgG in a dose-dependent manner without affecting IgA, IgM, or IgE in a clinical study on humans (Ling et al., 2019), indicating specific IgG binding sites on FcRn which corroborated our findings as well. Another clinical study reported that *M281* application led to mild dose-dependent downregulation of mean serum albumin levels, which was reversed to baseline by the end of post-treatment follow-up (Antozzi et al., 2024),

thus confirming the findings of the present study of reduced albumin endocytosis under conditions of *M281* treatment. Interestingly, our data suggested a time-dependent ligand-receptor binding kinetics for FcRn-mediated albumin endocytosis in ADSCs. Asialoglycoprotein receptor (ASGPR) and FcRn bind to their ligands with high affinity at neutral pH/high Ca^{2+}, whereas dissociation is acidic pH/low Ca^{2+}-dependent (Devanaboyina et al., 2024). These findings suggest that Ca^{2+} signals modulate FcRn binding affinity for albumin as well as IgG, which may involve contrasting pathways since FcRn possesses distinct binding sites that do not overlap.

The study of antibodies against FcRn is of great clinical importance. Targeting FcRn to treat gMG and its different subgroups has been complemented by notable investigations, and the FDA has recently approved *M281* as an antibody against this receptor (Kaminski et al., 2024). FcRn has great role beyond gMG since it was described as a pan-arterivirus receptor (Shaw et al., 2024), and blocking FcRn by efgartigimod treatment improved stiff-person syndrome, a neurological disorder (Di Stefano et al., 2024), *M281* administration reduced the risk of fetal anemia or

intrauterine transfusions in hemolytic disease of the fetus and newborn (Moise et al., 2024).

Increasing reports regarding ADSCs, their secretome, albumin, Ca^{2+} signaling, and FcRn have become potential therapeutic targets in diverse fields of cell therapy. In the current study, we demonstrated the association of albumin endocytosis with Ca^{2+} messengers and the transmembrane receptor molecule FcRn. Our data showed that both extracellular and intracellular Ca^{2+} dictate albumin endocytosis, which involves caveolae-dependent endocytosis, clathrin-mediated endocytosis, and macropinocytosis, in which FcRn is a key player. Future therapeutics may be discovered that involve ADSCs with programmable pathways related to albumin-mediated drug delivery by manipulating the Ca^{2+} flux and targeting FcRn with many novel synthetic antibodies or mutants. Accumulated data indicated that inhibition of certain endocytic pathways in ADSCs does not completely block albumin internalization. However, targeting multiple pathways resulted in a comparable decrease in uptake, suggesting that blocking one pathway is compensated by activating other pathways in parallel. Future studies may focus on how blocking one pathway initiates another to

control the pace of the endocytic rate because distinct cellular machinery is involved in different endocytic processes.

Notably, several antibodies targeting FcRn receptor sites have been approved for clinical use in the treatment of antibody-mediated autoimmune diseases such as gMG and immune thrombocytopenia (Wyckoff & Hudson, 2021). Our data indicated that M281 successfully manipulated Ca^{2+} oscillations and albumin uptake in ADSCs, suggesting that FcRn is a crucial player. These antibodies may significantly affect the immune status of the recipient by interfering with albumin and IgG recycling. Moreover, albumin, known for its exceptional binding capacity, is gaining attention as a dependable drug delivery molecule for the treatment of a range of life-threatening diseases, including cancer (Karami et al., 2024). Therefore, it is crucial to thoroughly investigate the impact of FcRn on various endocytic pathways to minimize the risk of adverse effects associated with FcRn-based immunotherapy.

6. Summary

Cellular albumin trafficking is very crucial to maintain the albumin homeostasis and is regulated by FcRn. Our experiments suggested albumin and IgG involvement in stimulating Ca^{2+} oscillations in subcutaneous ADSCs. The correlation of the albumin uptake process with Ca^{2+} oscillations in human ADSCs was investigated through intervention of different endocytosis pathways using respective blocking agents and modulators of Ca^{2+} channels and the impact of FcRn for the intracellular albumin and IgG content of ADSCs as well as Ca^{2+} oscillations was assessed.

We investigated uptake of fluorescence-labelled albumin and Ca^{2+} oscillations intervention with macropinocytosis inhibitors, i.e. *EIPA*, *Imp*, *CD*, *Won*, *MBQ-167*, inhibitors of caveolae-dependent endocytosis, i.e. *Gen*, *Nyn*, *Noco*, inhibitors of clathrin-mediated endocytosis, i.e. *CPZ*, *MDC*, *Dyngo-4a* as well as inhibitors of Ca^{2+} signaling, i.e. the Ca^{2+} release inhibitor *BAPTA-AM*, the SOCE inhibitor *SKF-96365*, and the CaSR antagonist *NPS-2143*. Our results demonstrated downregulation of albumin uptake and Ca^{2+} signaling in ADSCs preincubated with endocytosis blockers, *EIPA*, *CD*, *Won*, *MBQ-167*, *Gen*, *Nyn*, *Noco* and *Dyngo-4a*

and Ca^{2+} signal modulators, *BAPTA-AM*, *SKF-96365* and *NPS-2143*. Moreover, intervention of double pathways in combination, i.e. macropinocytosis and caveolae-mediated pathways with *EIPA*, *Won* and *Gen*, *Nyn*, respectively, downregulated albumin uptake about two-fold, suggesting that albumin uptake is regulated by Ca^{2+} signaling dominantly via caveolae-dependent endocytosis and macropinocytosis in ADSCs. We presented albumin colocalization with caveolin-1, megalin and FcRn in ADSCs.

We demonstrated FcRn expression in subdermal ADSCs and investigated $FcRn^{-}$ ADSCs generated by si-RNA-mediated knockdown of FcGRT gene and FcRn inhibitor *M281* for their role in albumin endocytosis and Ca^{2+} signaling and demonstrated termination of Ca^{2+} signaling, and decay in IgG and albumin internalization. Our data conclude that in ADSCs Ca^{2+} signaling regulates albumin uptake via FcRn-dependent mechanism through distinct endocytic pathways.

Key Words: ADSCs, Ca^{2+} Oscillation, Albumin, Endocytosis, FcRn, M281.

7. Zusammenfassung

Der zelluläre Transport von Albumin ist für die Aufrechterhaltung der Albumin-Homöostase von entscheidender Bedeutung und wird durch FcRn reguliert. Unsere Experimente zeigen, dass Albumin und IgG Ca^{2+}-Oszillationen in subkutanen ADSCs stimulieren. Die Korrelation zwischen der Albuminaufnahme und den Ca^{2+}-Oszillationen in humanen ADSCs wurde durch Eingriffe in verschiedene Endozytosewege mittels entsprechender Blocker und Modulatoren von Ca^{2+}-Kanälen untersucht und die Bedeutung des FcRn für intrazelluläres Albumin und IgG und intrazelluläre Ca^{2+} Oszillationen erforscht.

Wir untersuchten die Aufnahme von fluoreszenzmarkiertem Albumin sowie Ca^{2+}-Oszillationen, die durch Makropinozytose-Inhibitoren (*EIPA*, *Imp*, *CD*, *Won*, *MBQ-167*) und Inhibitoren der Caveolae-abhängigen Endozytose (*Gen*, *Nyn*, *Noco*) beeinflusst werden. Weiterhin wurden Inhibitoren der Clathrin-vermittelten Endozytose (d.h. *CPZ*, *MDC*) und *Dyngo-4a* sowie Inhibitoren der Ca^{2+}-Signale, d.h. der Ca^{2+}-Freisetzungsinhibitor *BAPTA-AM*, der speichergesteuerte Ca^{2+}-Eintrittsinhibitor (SOCE) *SKF-96365* und der CaSR-Antagonist *NPS-2143* untersucht.

Unsere Ergebnisse zeigten eine Herabregulierung der Albuminaufnahme und der Ca^{2+}-Signalübertragung in ADSCs durch die Endozytoseblocker *EIPA*, *CD*, *Won*, *MBQ-167*, *Gen*, *Nyn*, *Noco* und *Dyngo-4a* sowie die Ca^{2+}-Signalmodulatoren *BAPTA-AM*, *SKF-96365* und *NPS-2143*. Durch gleichzeitige Inhibition zweier Wege, d.h. Makropinozytose und Caveolae-vermittelter Wege, mit *EIPA*, *Won* und *Gen* bzw. *Nyn* wurde die Albuminaufnahme um etwa das Zweifache herabreguliert, was darauf hindeutet, dass die Albuminaufnahme in ADSCs hauptsächlich durch Ca^{2+}-Signale über Caveolae-abhängige Endozytose und Makropinozytose reguliert wird. Wir konnten eine Kolokalisierung von Albumin mit Caveolin-1 und Megalin in ADSCs darstellen.

Wir wiesen die FcRn-Expression in subdermalen ADSCs nach und untersuchten $FcRn^{-}$ ADSCs, die durch si-RNA-vermittelte Ausschaltung des FcGRT-Gens erzeugt wurden sowie den FcRn Inhibitor *M281* und konnten sowohl eine Beendigung der Ca^{2+}-Signalübertragung als auch eine signifikante Reduktion der IgG- und Albumin-Internalisierung nachweisen. Unsere Daten lassen den Schluss zu, dass Ca^{2+}-Signale in ADSCs die

Albuminaufnahme durch einen FcRn-abhängigen Mechanismus über spezifische Endozytosewege regulieren.

Schlüsselwörter: ADSCs, Ca^{2+}-Oszillation, Albumin, Endozytose, *FcRn*, *M281.*

8. References

Abdelbaset-Ismail, A., Tharwat, A., Ahmed, A. E., Khamis, T., Abd El-Rahim, I. H., Alhag, S. K., & Dowidar, M. F. (2022). Transplantation of adipose-derived mesenchymal stem cells ameliorates acute hepatic injury caused by nonsteroidal anti-inflammatory drug diclofenac sodium in female rats. *Biomed Pharmacother*, *155*, 113805. https://doi.org/10.1016/j.biopha.2022.113805

Ai, G., Meng, M., Guo, J., Li, C., Zhu, J., Liu, L., Liu, B., Yang, W., Shao, X., Cheng, Z., & Wang, L. (2023). Adipose-derived stem cells promote the repair of chemotherapy-induced premature ovarian failure by inhibiting granulosa cells apoptosis and senescence. *Stem Cell Res Ther*, *14*(1), 75. https://doi.org/10.1186/s13287-023-03297-5

Al-Ghadban, S., & Bunnell, B. A. (2020). Adipose Tissue-Derived Stem Cells: Immunomodulatory Effects and Therapeutic Potential. *Physiology (Bethesda)*, *35*(2), 125-133. https://doi.org/10.1152/physiol.00021.2019

Anggono, V., Smillie, K. J., Graham, M. E., Valova, V. A., Cousin, M. A., & Robinson, P. J. (2006). Syndapin I is the phosphorylation-regulated dynamin I partner in synaptic vesicle endocytosis. *Nat Neurosci*, *9*(6), 752-760. https://doi.org/10.1038/nn1695

Antozzi, C., Guptill, J., Bril, V., Gamez, J., Meuth, S. G., Nowak, R. J., Quan, D., Sevilla, T., Jouvin, M. H., Jin, J., Karcher, K., Ramchandren, S., Sun, H., Ling, L., Zhu, Y., Arroyo, S., & Vivacity, M. G. P. S. G. (2024). Safety and Efficacy of Nipocalimab in Patients With Generalized Myasthenia Gravis: Results From the Randomized Phase 2 Vivacity-

MG Study. *Neurology*, *102*(2), e207937. https://doi.org/10.1212/WNL.0000000000207937

Araki, N., Johnson, M. T., & Swanson, J. A. (1996). A role for phosphoinositide 3-kinase in the completion of macropinocytosis and phagocytosis by macrophages. *J Cell Biol*, *135*(5), 1249-1260. https://doi.org/10.1083/jcb.135.5.1249

Ard, R., Mulatz, K., Pomoransky, J. L., Parks, R. J., Trinkle-Mulcahy, L., Bell, J. C., & Gee, S. H. (2015). Regulation of Macropinocytosis by Diacylglycerol Kinase zeta. *PLoS One*, *10*(12), e0144942. https://doi.org/10.1371/journal.pone.0144942

Aysit-Altuncu, N., Ulusoy, C., Ozturk, G., & Tuzun, E. (2018). Effect of LGI1 antibody-positive IgG on hippocampal neuron survival: a preliminary study. *Neuroreport*, *29*(11), 932-938. https://doi.org/10.1097/WNR.0000000000001055

Bang, S., Qamar, A. Y., Yun, S. H., Gu, N. Y., Kim, H., Han, A., Kang, H., Park, H. S., Kim, S. I., Saadeldin, I. M., Lee, S., & Cho, J. (2024). Embryotrophic effect of exogenous protein contained adipose-derived stem cell extracellular vesicles. *J Anim Sci Biotechnol*, *15*(1), 145. https://doi.org/10.1186/s40104-024-01106-4

Bento-Abreu, A., Velasco, A., Polo-Hernandez, E., Lillo, C., Kozyraki, R., Tabernero, A., & Medina, J. M. (2009). Albumin endocytosis via megalin in astrocytes is caveola- and Dab-1 dependent and is required for the synthesis of the neurotrophic factor oleic acid. *J Neurochem*, *111*(1), 49-60. https://doi.org/10.1111/j.1471-4159.2009.06304.x

Bhattacharjee, M., Escobar Ivirico, J. L., Kan, H. M., Shah, S., Otsuka, T., Bordett, R., Barajaa, M., Nagiah, N., Pandey, R., Nair, L. S., & Laurencin, C. T. (2022). Injectable amnion hydrogel-mediated delivery of adipose-derived stem cells for osteoarthritis treatment. *Proc Natl Acad Sci U S A*, *119*(4). https://doi.org/10.1073/pnas.2120968119

Biazzo, A., D'Ambrosi, R., Masia, F., Izzo, V., & Verde, F. (2020). Autologous adipose stem cell therapy for knee osteoarthritis: where are we now? *Phys Sportsmed*, *48*(4), 392-399. https://doi.org/10.1080/00913847.2020.1758001

Borghi, S., Bournazos, S., Thulin, N. K., Li, C., Gajewski, A., Sherwood, R. W., Zhang, S., Harris, E., Jagannathan, P., Wang, L. X., Ravetch, J. V., & Wang, T. T. (2020). FcRn, but not FcgammaRs, drives maternal-fetal transplacental transport of human IgG antibodies. *Proc Natl Acad Sci U S A*, *117*(23), 12943-12951. https://doi.org/10.1073/pnas.2004325117

Bryniarski, M. A., Yee, B. M., Chaves, L. D., Stahura, C. M., Yacoub, R., & Morris, M. E. (2020). Megalin-mediated albumin endocytosis in cultured murine mesangial cells. *Biochem Biophys Res Commun*, *529*(3), 740-746. https://doi.org/10.1016/j.bbrc.2020.05.166

Canton, J., Schlam, D., Breuer, C., Gutschow, M., Glogauer, M., & Grinstein, S. (2016). Calcium-sensing receptors signal constitutive macropinocytosis and facilitate the uptake of NOD2 ligands in macrophages. *Nat Commun*, *7*, 11284. https://doi.org/10.1038/ncomms11284

Caruso-Neves, C., Pinheiro, A. A., Cai, H., Souza-Menezes, J., & Guggino, W. B. (2006). PKB and megalin determine the survival or death of renal proximal tubule cells. *Proc Natl Acad Sci U S A*, *103*(49), 18810-18815. https://doi.org/10.1073/pnas.0605029103

Casado-Losada, I., Acosta, M., Schadl, B., Priglinger, E., Wolbank, S., & Nurnberger, S. (2024). Unlocking Potential: Low Bovine Serum Albumin Enhances the Chondrogenicity of Human Adipose-Derived Stromal Cells in Pellet Cultures. *Biomolecules*, *14*(4). https://doi.org/10.3390/biom14040413

Chang, Y., Ping, A., Chang, C., Betz, V. M., Cai, L., & Ren, B. (2023). Lactoferrin Mediates Enhanced Osteogenesis of Adipose-

Derived Stem Cells: Innovative Molecular and Cellular Therapy for Bone Repair. *Int J Mol Sci*, *24*(2). https://doi.org/10.3390/ijms24021749

Chappell, A. E., Gaus, H. J., Berdeja, A., Gupta, R., Jo, M., Prakash, T. P., Oestergaard, M., Swayze, E. E., & Seth, P. P. (2020). Mechanisms of palmitic acid-conjugated antisense oligonucleotide distribution in mice. *Nucleic Acids Res*, *48*(8), 4382-4395. https://doi.org/10.1093/nar/gkaa164

Chatterjee, M., Ben-Josef, E., Robb, R., Vedaie, M., Seum, S., Thirumoorthy, K., Palanichamy, K., Harbrecht, M., Chakravarti, A., & Williams, T. M. (2017). Caveolae-Mediated Endocytosis Is Critical for Albumin Cellular Uptake and Response to Albumin-Bound Chemotherapy. *Cancer Res*, *77*(21), 5925-5937. https://doi.org/10.1158/0008-5472.CAN-17-0604

Chen, H., Li, Z., Lin, M., Lv, X., Wang, J., Wei, Q., Zhang, Z., & Li, L. (2021). MicroRNA-124-3p affects myogenic differentiation of adipose-derived stem cells by targeting Caveolin-1 during pelvic floor dysfunction in Sprague Dawley rats. *Ann Transl Med*, *9*(2), 161. https://doi.org/10.21037/atm-20-8212

Chen, Y., Li, P., Chen, X., Yan, R., Zhang, Y., Wang, M., Qin, X., Li, S., Zheng, C., You, F., Li, T., & Liu, Y. (2023). Endoplasmic reticulum-mitochondrial calcium transport contributes to soft extracellular matrix-triggered mitochondrial dynamics and mitophagy in breast carcinoma cells. *Acta Biomater*, *169*, 192-208. https://doi.org/10.1016/j.actbio.2023.07.060

Cheng, X., Chen, K., Dong, B., Yang, M., Filbrun, S. L., Myoung, Y., Huang, T. X., Gu, Y., Wang, G., & Fang, N. (2021). Dynamin-dependent vesicle twist at the final stage of clathrin-mediated endocytosis. *Nat Cell Biol*, *23*(8), 859-869. https://doi.org/10.1038/s41556-021-00713-x

Choudhury, A., Noël, W., Ebrahim, T., Shu, C., Ling, L. E., & Fattizzo, B. (2022). Mode of Nipocalimab Action and

Pharmacology in Cells and Preclinical Models. *Blood*, *140*(Supplement 1), 8161-8162. https://doi.org/10.1182/blood-2022-165381

Chun, B. J., Aryal, S. P., Varughese, P., Sun, B., Bruno, J. A., Richards, C. I., Bachstetter, A. D., & Kekenes-Huskey, P. M. (2022). Purinoreceptors and ectonucleotidases control ATP-induced calcium waveforms and calcium-dependent responses in microglia: Roles of P2 receptors and CD39 in ATP-stimulated microglia. *Front Physiol*, *13*, 1037417. https://doi.org/10.3389/fphys.2022.1037417

Cifuentes, M., Albala, C., & Rojas, C. (2005). Calcium-sensing receptor expression in human adipocytes. *Endocrinology*, *146*(5), 2176-2179. https://doi.org/10.1210/en.2004-1281

D'Hooghe, L., Chalmers, A. D., Heywood, S., & Whitley, P. (2017). Cell surface dynamics and cellular distribution of endogenous FcRn. *PLoS One*, *12*(8), e0182695. https://doi.org/10.1371/journal.pone.0182695

Dahlke, E., Anan, Y., Klie, L. M., Hartkopf, A. E., & Theilig, F. (2022). Megalin Orchestrates FcRn Endocytosis and Trafficking. *Cells*, *12*(1). https://doi.org/10.3390/cells12010053

Daniel, J. A., Chau, N., Abdel-Hamid, M. K., Hu, L., von Kleist, L., Whiting, A., Krishnan, S., Maamary, P., Joseph, S. R., Simpson, F., Haucke, V., McCluskey, A., & Robinson, P. J. (2015). Phenothiazine-derived antipsychotic drugs inhibit dynamin and clathrin-mediated endocytosis. *Traffic*, *16*(6), 635-654. https://doi.org/10.1111/tra.12272

Dannhauser, P. N., Platen, M., Boning, H., Ungewickell, H., Schaap, I. A., & Ungewickell, E. J. (2015). Effect of clathrin light chains on the stiffness of clathrin lattices and membrane budding. *Traffic*, *16*(5), 519-533. https://doi.org/10.1111/tra.12263

Davis, L. C., Morgan, A. J., & Galione, A. (2020). NAADP-regulated two-pore channels drive phagocytosis through endo-

lysosomal Ca(2+) nanodomains, calcineurin and dynamin. *EMBO J*, *39*(14), e104058. https://doi.org/10.15252/embj.2019104058

Devanaboyina, S. C., Li, P., LaGory, E. L., Poon-Andersen, C., Cook, K. D., Soto, M., Wang, Z., Dang, K., Uyeda, C., Case, R. B., Thomas, V. A., Primack, R., Ponce, M., Di, M., Ouyang, B., Kaner, J., Lam, S. K., & Mostafavi, M. (2024). Rapid depletion of "catch-and-release" anti-ASGR1 antibody in vivo. *MAbs*, *16*(1), 2383013. https://doi.org/10.1080/19420862.2024.2383013

Di Stefano, V., Alonge, P., Rini, N., Militello, M., Lupica, A., Torrente, A., & Brighina, F. (2024). Efgartigimod beyond myasthenia gravis: the role of FcRn-targeting therapies in stiff-person syndrome. *J Neurol*, *271*(1), 254-262. https://doi.org/10.1007/s00415-023-11970-1

Dickinson, B. L., Claypool, S. M., D'Angelo, J. A., Aiken, M. L., Venu, N., Yen, E. H., Wagner, J. S., Borawski, J. A., Pierce, A. T., Hershberg, R., Blumberg, R. S., & Lencer, W. I. (2008). Ca2+-dependent calmodulin binding to FcRn affects immunoglobulin G transport in the transcytotic pathway. *Mol Biol Cell*, *19*(1), 414-423. https://doi.org/10.1091/mbc.e07-07-0658

Dobrinskikh, E., Okamura, K., Kopp, J. B., Doctor, R. B., & Blaine, J. (2014). Human podocytes perform polarized, caveolae-dependent albumin endocytosis. *Am J Physiol Renal Physiol*, *306*(9), F941-951. https://doi.org/10.1152/ajprenal.00532.2013

Doodnauth, S. A., Grinstein, S., & Maxson, M. E. (2019). Constitutive and stimulated macropinocytosis in macrophages: roles in immunity and in the pathogenesis of atherosclerosis. *Philos Trans R Soc Lond B Biol Sci*, *374*(1765), 20180147. https://doi.org/10.1098/rstb.2018.0147

Du, S. S., Sun, X., Cen, J., Shi, J. X., An, M. X., & Zhao, W. D. (2021). Dynamin-2 mediates clathrin-dependent endocytosis for

amyloid-beta internalization in brain microvascular endothelial cells. *Microvasc Res*, *138*, 104219. https://doi.org/10.1016/j.mvr.2021.104219

Ferdowsi, P. V., Ahuja, K. D. K., Beckett, J. M., & Myers, S. (2022). Capsaicin and Zinc Promote Glucose Uptake in C2C12 Skeletal Muscle Cells through a Common Calcium Signalling Pathway. *Int J Mol Sci*, *23*(4). https://doi.org/10.3390/ijms23042207

Frangiamore, R., Rinaldi, E., Vanoli, F., Andreetta, F., Ciusani, E., Bonanno, S., Maggi, L., Gallone, A., Colasuonno, A., Tramacere, I., Cheli, M., Pinna, A., Mantegazza, R., & Antozzi, C. (2024). Efgartigimod in generalized myasthenia gravis: A real-life experience at a national reference center. *Eur J Neurol*, *31*(4), e16189. https://doi.org/10.1111/ene.16189

Friedhoff, V. N., Lindner, B., & Falcke, M. (2023). Modeling IP(3)-induced Ca(2+) signaling based on its interspike interval statistics. *Biophys J*, *122*(13), 2818-2831. https://doi.org/10.1016/j.bpj.2023.06.004

Fuchs, L., Shelly, S., Vigiser, I., Kolb, H., Regev, K., Schwartzmann, Y., Vaknin-Dembinsky, A., Dori, A., & Karni, A. (2024). Real-World experience with efgartigimod in patients with myasthenia gravis. *J Neurol*, *271*(6), 3462-3470. https://doi.org/10.1007/s00415-024-12293-5

Fung, T. S., Chakrabarti, R., Kollasser, J., Rottner, K., Stradal, T. E. B., Kage, F., & Higgs, H. N. (2022). Parallel kinase pathways stimulate actin polymerization at depolarized mitochondria. *Curr Biol*, *32*(7), 1577-1592 e1578. https://doi.org/10.1016/j.cub.2022.02.058

Garcia-Contreras, M., Vera-Donoso, C. D., Hernandez-Andreu, J. M., Garcia-Verdugo, J. M., & Oltra, E. (2014). Therapeutic potential of human adipose-derived stem cells (ADSCs) from cancer patients: a pilot study. *PLoS One*, *9*(11), e113288. https://doi.org/10.1371/journal.pone.0113288

Gerke, C., Zabala Gutierrez, I., Mendez-Gonzalez, D., Cruz, M. C. I., Mulero, F., Jaque, D., & Rubio-Retama, J. (2022). Clickable Albumin Nanoparticles for Pretargeted Drug Delivery toward PD-L1 Overexpressing Tumors in Combination Immunotherapy. *Bioconjug Chem*, *33*(5), 821-828. https://doi.org/10.1021/acs.bioconjchem.2c00087

Glebov, O. O., Bright, N. A., & Nichols, B. J. (2006). Flotillin-1 defines a clathrin-independent endocytic pathway in mammalian cells. *Nat Cell Biol*, *8*(1), 46-54. https://doi.org/10.1038/ncb1342

Gong, L., Li, G., Yi, X., Han, Q., Wu, Q., Ying, F., Shen, L., Cao, Y., Liu, X., Gao, L., Li, W., Wang, Z., & Cai, J. (2024). Tumor-derived small extracellular vesicles facilitate omental metastasis of ovarian cancer by triggering activation of mesenchymal stem cells. *Cell Commun Signal*, *22*(1), 47. https://doi.org/10.1186/s12964-023-01413-9

Greenberg, H. Z. E., Jahan, K. S., Shi, J., Vanessa Ho, W. S., & Albert, A. P. (2016). The calcilytics Calhex-231 and NPS 2143 and the calcimimetic Calindol reduce vascular reactivity via inhibition of voltage-gated Ca(2+) channels. *Eur J Pharmacol*, *791*, 659-668. https://doi.org/10.1016/j.ejphar.2016.10.008

Gregory, C. A., Gunn, W. G., Peister, A., & Prockop, D. J. (2004). An Alizarin red-based assay of mineralization by adherent cells in culture: comparison with cetylpyridinium chloride extraction. *Anal Biochem*, *329*(1), 77-84. https://doi.org/10.1016/j.ab.2004.02.002

Grixti, J. M., Ayers, D., & Day, P. J. R. (2021). An Analysis of Mechanisms for Cellular Uptake of miRNAs to Enhance Drug Delivery and Efficacy in Cancer Chemoresistance. *Noncoding RNA*, *7*(2). https://doi.org/10.3390/ncrna7020027

Guo, S. K., Sodt, A. J., & Johnson, M. E. (2022). Large self-assembled clathrin lattices spontaneously disassemble

without sufficient adaptor proteins. *PLoS Comput Biol*, *18*(3), e1009969. https://doi.org/10.1371/journal.pcbi.1009969

Guptill, J. T., Sleasman, J. W., Steeland, S., Sips, M., Gelinas, D., de Haard, H., Azar, A., & Winthrop, K. L. (2022). Effect of FcRn antagonism on protective antibodies and to vaccines in IgG-mediated autoimmune diseases pemphigus and generalised myasthenia gravis. *Autoimmunity*, *55*(8), 620-631. https://doi.org/10.1080/08916934.2022.2104261

Hameedat, F., Pinto, S., Marques, J., Dias, S., & Sarmento, B. (2023). Functionalized zein nanoparticles targeting neonatal Fc receptor to enhance lung absorption of peptides. *Drug Deliv Transl Res*, *13*(6), 1699-1715. https://doi.org/10.1007/s13346-022-01286-4

Han, C., Wang, Y. J., Wang, Y. C., Guan, X., Wang, L., Shen, L. M., Zou, W., & Liu, J. (2021). Caveolin-1 downregulation promotes the dopaminergic neuron-like differentiation of human adipose-derived mesenchymal stem cells. *Neural Regen Res*, *16*(4), 714-720. https://doi.org/10.4103/1673-5374.295342

Hartenstein, V., & Martinez, P. (2019). Structure, development and evolution of the digestive system. *Cell Tissue Res*, *377*(3), 289-292. https://doi.org/10.1007/s00441-019-03102-x

He, W., Xu, C., Huang, Y., Zhang, Q., Chen, W., Zhao, C., Chen, Y., Zheng, D., XinyueLin, Luo, Q., Chen, X., Zhang, Z., Wu, X., Huang, J., Lin, C., Huang, Y., & Zhang, S. (2024). Therapeutic potential of ADSC-EV-derived lncRNA DLEU2: A novel molecular pathway in alleviating sepsis-induced lung injury via the miR-106a-5p/LXN axis. *Int Immunopharmacol*, *130*, 111519. https://doi.org/10.1016/j.intimp.2024.111519

Head, B. P., Patel, H. H., Roth, D. M., Murray, F., Swaney, J. S., Niesman, I. R., Farquhar, M. G., & Insel, P. A. (2006).

Microtubules and actin microfilaments regulate lipid raft/caveolae localization of adenylyl cyclase signaling components. *J Biol Chem*, *281*(36), 26391-26399. https://doi.org/10.1074/jbc.M602577200

Henley, J. R., Krueger, E. W., Oswald, B. J., & McNiven, M. A. (1998). Dynamin-mediated internalization of caveolae. *J Cell Biol*, *141*(1), 85-99. https://doi.org/10.1083/jcb.141.1.85

Herzog, H., Glockler, S., Flamm, J., Ladel, S., Maigler, F., Pitzer, C., & Schindowski, K. (2024). Intranasal Nose-to-Brain Drug Delivery via the Olfactory Region in Mice: Two In-Depth Protocols for Region-Specific Intranasal Application of Antibodies and for Expression Analysis of Fc Receptors via In Situ Hybridization in the Nasal Mucosa. *Methods Mol Biol*, *2754*, 387-410. https://doi.org/10.1007/978-1-0716-3629-9_21

Hinshaw, J. (2000). Dynamin and its role in membrane fission. *Annual review of cell and developmental biology*, *16*(1), 483-519.

Hisanaga, M., Tsuchiya, T., Watanabe, H., Shimoyama, K., Iwatake, M., Tanoue, Y., Maruyama, K., Yukawa, H., Sato, K., Kato, Y., Matsumoto, K., Miyazaki, T., Doi, R., Tomoshige, K., & Nagayasu, T. (2023). Adipose-Derived Mesenchymal Stem Cells Attenuate Immune Reactions Against Pig Decellularized Bronchi Engrafted into Rat Tracheal Defects. *Organogenesis*, *19*(1), 2212582. https://doi.org/10.1080/15476278.2023.2212582

Hooper, C., Taylor, D. L., & Pocock, J. M. (2005). Pure albumin is a potent trigger of calcium signalling and proliferation in microglia but not macrophages or astrocytes. *J Neurochem*, *92*(6), 1363-1376. https://doi.org/10.1111/j.1471-4159.2005.02982.x

Huang, Y., Ng, T. K., Chen, C. B., Huang, B., Liang, J., Pang, C. P., & Zhang, M. (2018). Notch Signaling Activation Enhances Human Adipose-Derived Stem Cell Retinal

Differentiation. *Stem Cells Int*, *2018*, 9201374. https://doi.org/10.1155/2018/9201374

Hubert, M., Larsson, E., Vegesna, N. V. G., Ahnlund, M., Johansson, A. I., Moodie, L. W., & Lundmark, R. (2020). Lipid accumulation controls the balance between surface connection and scission of caveolae. *Elife*, *9*. https://doi.org/10.7554/eLife.55038

Ichinose, K., Ushigusa, T., Nishino, A., Nakashima, Y., Suzuki, T., Horai, Y., Koga, T., Kawashiri, S. Y., Iwamoto, N., Tamai, M., Arima, K., Nakamura, H., Obata, Y., Yamamoto, K., Origuchi, T., Nishino, T., Kawakami, A., & Tsokos, G. C. (2016). Lupus Nephritis IgG Induction of Calcium/Calmodulin-Dependent Protein Kinase IV Expression in Podocytes and Alteration of Their Function. *Arthritis Rheumatol*, *68*(4), 944-952. https://doi.org/10.1002/art.39499

Iyer, M., Kantarci, H., Cooper, M. H., Ambiel, N., Novak, S. W., Andrade, L. R., Lam, M., Jones, G., Munch, A. E., Yu, X., Khakh, B. S., Manor, U., & Zuchero, J. B. (2024). Oligodendrocyte calcium signaling promotes actin-dependent myelin sheath extension. *Nat Commun*, *15*(1), 265. https://doi.org/10.1038/s41467-023-44238-3

Junka, R., Zhou, X., Wang, W., & Yu, X. (2022). Albumin-Coated Polycaprolactone (PCL)-Decellularized Extracellular Matrix (dECM) Scaffold for Bone Regeneration. *ACS Appl Bio Mater*, *5*(12), 5634-5644. https://doi.org/10.1021/acsabm.2c00686

Kaminski, H. J., Sikorski, P., Coronel, S. I., & Kusner, L. L. (2024). Myasthenia gravis: the future is here. *J Clin Invest*, *134*(12). https://doi.org/10.1172/JCI179742

Karami, E., Mesbahi Moghaddam, M., & Kazemi-Lomedasht, F. (2024). Use of Albumin for Drug Delivery as a Diagnostic and Therapeutic Tool. *Curr Pharm Biotechnol*, *25*(6), 676-693. https://doi.org/10.2174/1389201024666230807161200

Kim, H. G., Sung, N. Y., Kim, J. H., & Cho, J. Y. (2023). In vitro anti-cancer effects of beauvericin through inhibition of actin polymerization and Src phosphorylation. *Phytomedicine*, *109*, 154573. https://doi.org/10.1016/j.phymed.2022.154573

Kroeze, R. J., Knippenberg, M., & Helder, M. N. (2011). Osteogenic differentiation strategies for adipose-derived mesenchymal stem cells. *Methods Mol Biol*, *702*, 233-248. https://doi.org/10.1007/978-1-61737-960-4_17

Lambert, C., Schmidt, K., Karger, M., Stadler, M., Stradal, T. E. B., & Rottner, K. (2023). Cytochalasans and Their Impact on Actin Filament Remodeling. *Biomolecules*, *13*(8). https://doi.org/10.3390/biom13081247

Lau, C. S., Park, S. Y., Ethiraj, L. P., Singh, P., Raj, G., Quek, J., Prasadh, S., Choo, Y., & Goh, B. T. (2024). Role of Adipose-Derived Mesenchymal Stem Cells in Bone Regeneration. *Int J Mol Sci*, *25*(12). https://doi.org/10.3390/ijms25126805

Laube, M., & Thome, U. H. (2022). Albumin Stimulates Epithelial Na(+) Transport and Barrier Integrity by Activating the PI3K/AKT/SGK1 Pathway. *Int J Mol Sci*, *23*(15). https://doi.org/10.3390/ijms23158823

Lee, G., Leech, G., Rust, M. J., Das, M., McGorty, R. J., Ross, J. L., & Robertson-Anderson, R. M. (2021). Myosin-driven actin-microtubule networks exhibit self-organized contractile dynamics. *Sci Adv*, *7*(6). https://doi.org/10.1126/sciadv.abe4334

Lee, T. L., Lai, T. C., Lin, S. R., Lin, S. W., Chen, Y. C., Pu, C. M., Lee, I. T., Tsai, J. S., Lee, C. W., & Chen, Y. L. (2021). Conditioned medium from adipose-derived stem cells attenuates ischemia/reperfusion-induced cardiac injury through the microRNA-221/222/PUMA/ETS-1 pathway. *Theranostics*, *11*(7), 3131-3149. https://doi.org/10.7150/thno.52677

Lee, T. L., Shen, W. C., Chen, Y. C., Lai, T. C., Lin, S. R., Lin, S. W., Yu, I. S., Yeh, Y. H., Li, T. K., Lee, I. T., Lee, C. W., & Chen, Y. L. (2025). Mir221- and Mir222-enriched adsc-exosomes mitigate PM exposure-exacerbated cardiac ischemia-reperfusion injury through the modulation of the BNIP3-MAP1LC3B-BBC3/PUMA pathway. *Autophagy*, *21*(2), 374-393. https://doi.org/10.1080/15548627.2024.2395799

Li, H. H., Li, J., Wasserloos, K. J., Wallace, C., Sullivan, M. G., Bauer, P. M., Stolz, D. B., Lee, J. S., Watkins, S. C., St Croix, C. M., Pitt, B. R., & Zhang, L. M. (2013). Caveolae-dependent and -independent uptake of albumin in cultured rodent pulmonary endothelial cells. *PLoS One*, *8*(11), e81903. https://doi.org/10.1371/journal.pone.0081903

Li, J., Ruffenach, G., Kararigas, G., Cunningham, C. M., Motayagheni, N., Barakai, N., Umar, S., Regitz-Zagrosek, V., & Eghbali, M. (2017). Intralipid protects the heart in late pregnancy against ischemia/reperfusion injury via Caveolin2/STAT3/GSK-3beta pathway. *J Mol Cell Cardiol*, *102*, 108-116. https://doi.org/10.1016/j.yjmcc.2016.11.006

Li, X., Fang, S., Wang, S., Xie, Y., Xia, Y., Wang, P., Hao, Z., Xu, S., & Zhang, Y. (2024). Hypoxia preconditioning of adipose stem cell-derived exosomes loaded in gelatin methacryloyl (GelMA) promote type H angiogenesis and osteoporotic fracture repair. *J Nanobiotechnology*, *22*(1), 112. https://doi.org/10.1186/s12951-024-02342-6

Liang, H. B., Chen, X., Zhao, R., Li, S. J., Huang, P. S., Tang, Y. H., Cui, G. H., & Liu, J. R. (2024). Simultaneous ischemic regions targeting and BBB crossing strategy to harness extracellular vesicles for therapeutic delivery in ischemic stroke. *J Control Release*, *365*, 1037-1057. https://doi.org/10.1016/j.jconrel.2023.12.021

Lin, H. P., Singla, B., Ghoshal, P., Faulkner, J. L., Cherian-Shaw, M., O'Connor, P. M., She, J. X., Belin de Chantemele, E. J., &

Csanyi, G. (2018). Identification of novel macropinocytosis inhibitors using a rational screen of Food and Drug Administration-approved drugs. *Br J Pharmacol*, *175*(18), 3640-3655. https://doi.org/10.1111/bph.14429

Ling, L. E., Hillson, J. L., Tiessen, R. G., Bosje, T., van Iersel, M. P., Nix, D. J., Markowitz, L., Cilfone, N. A., Duffner, J., Streisand, J. B., Manning, A. M., & Arroyo, S. (2019). M281, an Anti-FcRn Antibody: Pharmacodynamics, Pharmacokinetics, and Safety Across the Full Range of IgG Reduction in a First-in-Human Study. *Clin Pharmacol Ther*, *105*(4), 1031-1039. https://doi.org/10.1002/cpt.1276

Litvinova, L. S., Shupletsova, V. V., Khaziakhmatova, O. G., Daminova, A. G., Kudryavtseva, V. L., Yurova, K. A., Malashchenko, V. V., Todosenko, N. M., Popova, V., Litvinov, R. I., Korotkova, E. I., Sukhorukov, G. B., Gow, A. J., Weissman, D., Atochina-Vasserman, E. N., & Khlusov, I. A. (2022). Human Mesenchymal Stem Cells as a Carrier for a Cell-Mediated Drug Delivery. *Front Bioeng Biotechnol*, *10*, 796111. https://doi.org/10.3389/fbioe.2022.796111

Liu, X., Gao, R., Wu, Q., Li, G., Xu, X., Li, W., Liu, P., Wang, X., Cai, J., Li, M., & Wang, Z. (2024). ITGA7 loss drives the differentiation of adipose-derived mesenchymal stem cells to cancer-associated fibroblasts. *Mol Carcinog*, *63*(3), 479-493. https://doi.org/10.1002/mc.23665

Liu, Y., Wang, Y., Yang, Y., Weng, L., Wu, Q., Zhang, J., Zhao, P., Fang, L., Shi, Y., & Wang, P. (2023). Emerging phagocytosis checkpoints in cancer immunotherapy. *Signal Transduct Target Ther*, *8*(1), 104. https://doi.org/10.1038/s41392-023-01365-z

Lolo, F. N., Walani, N., Seemann, E., Zalvidea, D., Pavon, D. M., Cojoc, G., Zamai, M., Viaris de Lesegno, C., Martinez de Benito, F., Sanchez-Alvarez, M., Uriarte, J. J., Echarri, A.,

Jimenez-Carretero, D., Escolano, J. C., Sanchez, S. A., Caiolfa, V. R., Navajas, D., Trepat, X., Guck, J., . . . Del Pozo, M. A. (2023). Caveolin-1 dolines form a distinct and rapid caveolae-independent mechanoadaptation system. *Nat Cell Biol*, *25*(1), 120-133. https://doi.org/10.1038/s41556-022-01034-3

Lowry, O. H., Rosebrough, N. J., Farr, A. L., & Randall, R. J. (1951). Protein measurement with the Folin phenol reagent. *J Biol Chem*, *193*(1), 265-275. https://www.ncbi.nlm.nih.gov/pubmed/14907713

Lu, W., Yang, Z., Wang, M., Li, S., Bi, H., & Yang, X. (2024). Identification and verification of AK4 as a protective immune-related biomarker in adipose-derived stem cells and breast cancer. *Heliyon*, *10*(7), e27357. https://doi.org/10.1016/j.heliyon.2024.e27357

Ma, G., Crowley, A. R., Heyndrickx, L., Rogiers, I., Parthoens, E., Van Santbergen, J., Ober, R. J., Bobkov, V., de Haard, H., Ulrichts, P., Hofman, E., Louagie, E., Balbino, B., & Ward, E. S. (2024). Differential effects of FcRn antagonists on the subcellular trafficking of FcRn and albumin. *JCI Insight*, *9*(10). https://doi.org/10.1172/jci.insight.176166

Maeda, H., Ichimizu, S., Watanabe, H., Hamasaki, K., Chikamatsu, M., Murata, R., Yumoto, N., Seki, T., Katsuki, H., Otagiri, M., & Maruyama, T. (2022). Cell-penetrating albumin enhances the sublingual delivery of antigens through macropinocytosis. *Int J Biol Macromol*, *221*, 1439-1452. https://doi.org/10.1016/j.ijbiomac.2022.09.132

Malette, J., Degrandmaison, J., Giguere, H., Berthiaume, J., Frappier, M., Parent, J. L., Auger-Messier, M., & Boulay, G. (2019). MURC/CAVIN-4 facilitates store-operated calcium entry in neonatal cardiomyocytes. *Biochim Biophys Acta Mol Cell Res*, *1866*(8), 1249-1259. https://doi.org/10.1016/j.bbamcr.2019.03.017

Marois, L., Pare, G., Vaillancourt, M., Rollet-Labelle, E., & Naccache, P. H. (2011). Fc gammaRIIIb triggers raft-

dependent calcium influx in IgG-mediated responses in human neutrophils. *J Biol Chem*, *286*(5), 3509-3519. https://doi.org/10.1074/jbc.M110.169516

Masoumi, N., Ghollasi, M., Raheleh, H., Eftekhari, E., & Ghiasi, M. (2023). Carbachol, along with calcium, indicates new strategy in neural differentiation of human adipose tissue-derived mesenchymal stem cells in vitro. *Regen Ther*, *23*, 60-66. https://doi.org/10.1016/j.reth.2023.04.001

Matsunobe, M., Motohashi, N., Aoki, E., Tominari, T., Inada, M., & Aoki, Y. (2022). Caveolin-3 regulates the activity of Ca(2+)/calmodulin-dependent protein kinase II in C2C12 cells. *Am J Physiol Cell Physiol*, *323*(4), C1137-C1148. https://doi.org/10.1152/ajpcell.00077.2022

McCluskey, A., Daniel, J. A., Hadzic, G., Chau, N., Clayton, E. L., Mariana, A., Whiting, A., Gorgani, N. N., Lloyd, J., Quan, A., Moshkanbaryans, L., Krishnan, S., Perera, S., Chircop, M., von Kleist, L., McGeachie, A. B., Howes, M. T., Parton, R. G., Campbell, M., . . . Robinson, P. J. (2013). Building a better dynasore: the dyngo compounds potently inhibit dynamin and endocytosis. *Traffic*, *14*(12), 1272-1289. https://doi.org/10.1111/tra.12119

Meng, D., Yang, Q., Jeong, M. H., Curukovic, A., Tiwary, S., Melick, C. H., Lama-Sherpa, T. D., Wang, H., Huerta-Rosario, M., Urquhart, G., Zacharias, L. G., Lewis, C., DeBerardinis, R. J., & Jewell, J. L. (2022). SNAT7 regulates mTORC1 via macropinocytosis. *Proc Natl Acad Sci U S A*, *119*(20), e2123261119. https://doi.org/10.1073/pnas.2123261119

Merritt, J. E., Armstrong, W. P., Benham, C. D., Hallam, T. J., Jacob, R., Jaxa-Chamiec, A., Leigh, B. K., McCarthy, S. A., Moores, K. E., & Rink, T. J. (1990). SK&F 96365, a novel inhibitor of receptor-mediated calcium entry. *Biochem J*, *271*(2), 515-522. https://doi.org/10.1042/bj2710515

Miao, L., Lin, J., Huang, Y., Li, L., Delcassian, D., Ge, Y., Shi, Y., & Anderson, D. G. (2020). Synergistic lipid compositions for albumin receptor mediated delivery of mRNA to the liver. *Nat Commun*, *11*(1), 2424. https://doi.org/10.1038/s41467-020-16248-y

Moise, K. J., Jr., Ling, L. E., Oepkes, D., Tiblad, E., Verweij, E., Lopriore, E., Smoleniec, J., Sachs, U. J., Bein, G., Kilby, M. D., Miller, R. S., Devlieger, R., Audibert, F., Emery, S. P., Markham, K., Norton, M. E., Ocon-Hernandez, O., Pandya, P., Pereira, L., . . . Group, U. S. (2024). Nipocalimab in Early-Onset Severe Hemolytic Disease of the Fetus and Newborn. *N Engl J Med*, *391*(6), 526-537. https://doi.org/10.1056/NEJMoa2314466

Molostvov, G., James, S., Fletcher, S., Bennett, J., Lehnert, H., Bland, R., & Zehnder, D. (2007). Extracellular calcium-sensing receptor is functionally expressed in human artery. *Am J Physiol Renal Physiol*, *293*(3), F946-955. https://doi.org/10.1152/ajprenal.00474.2006

Morais, T. P., Coelho, D., Vaz, S. H., Sebastiao, A. M., & Valente, C. A. (2017). Glycine Receptor Activation Impairs ATP-Induced Calcium Transients in Cultured Cortical Astrocytes. *Front Mol Neurosci*, *10*, 444. https://doi.org/10.3389/fnmol.2017.00444

Moriyama, T., Hasegawa, F., Miyabe, Y., Akiyama, K., Karasawa, K., Uchida, K., & Nitta, K. (2021). Intracellular trafficking pathway of albumin in glomerular epithelial cells. *Biochem Biophys Res Commun*, *574*, 97-103. https://doi.org/10.1016/j.bbrc.2021.08.043

Moshkforoush, A., Balachandar, L., Moncion, C., Montejo, K. A., & Riera, J. (2021). Unraveling ChR2-driven stochastic Ca2+ dynamics in astrocytes: A call for new interventional paradigms. *PLoS Comput Biol*, *17*(2), e1008648. https://doi.org/10.1371/journal.pcbi.1008648

Muenzner, J., Traub, L. M., Kelly, B. T., & Graham, S. C. (2017). Cellular and viral peptides bind multiple sites on the N-

terminal domain of clathrin. *Traffic*, *18*(1), 44-57. https://doi.org/10.1111/tra.12457

Mukherjee, K., Khatua, B., & Mandal, C. (2020). Sialic Acid-Siglec-E Interactions During Pseudomonas aeruginosa Infection of Macrophages Interferes With Phagosome Maturation by Altering Intracellular Calcium Concentrations. *Front Immunol*, *11*, 332. https://doi.org/10.3389/fimmu.2020.00332

Mund, M., Tschanz, A., Wu, Y. L., Frey, F., Mehl, J. L., Kaksonen, M., Avinoam, O., Schwarz, U. S., & Ries, J. (2023). Clathrin coats partially preassemble and subsequently bend during endocytosis. *J Cell Biol*, *222*(3). https://doi.org/10.1083/jcb.202206038

Nathke, I., Hill, B. L., Parham, P., & Brodsky, F. M. (1990). The calcium-binding site of clathrin light chains. *J Biol Chem*, *265*(30), 18621-18627. https://www.ncbi.nlm.nih.gov/pubmed/2211724

Ni, X., Shan, X., Xu, L., Yu, W., Zhang, M., Lei, C., Xu, N., Lin, J., & Wang, B. (2021). Adipose-derived stem cells combined with platelet-rich plasma enhance wound healing in a rat model of full-thickness skin defects. *Stem Cell Res Ther*, *12*(1), 226. https://doi.org/10.1186/s13287-021-02257-1

Nilsen, J., Bern, M., Sand, K. M. K., Grevys, A., Dalhus, B., Sandlie, I., & Andersen, J. T. (2018). Human and mouse albumin bind their respective neonatal Fc receptors differently. *Sci Rep*, *8*(1), 14648. https://doi.org/10.1038/s41598-018-32817-0

Nomura, M., George, J., Hashizume, C., Saito, T., Ueda, Y., Ishigaki, Y., Tsuchishima, M., & Tsutsumi, M. (2022). Surgical implantation of human adipose derived stem cells attenuates experimentally induced hepatic fibrosis in rats. *Mol Med*, *28*(1), 143. https://doi.org/10.1186/s10020-022-00566-6

Ock, S. A., Kim, S. Y., Ju, W. S., Kim, Y. I., Wi, H. Y., & Lee, P. (2023). Adipose Tissue-Derived Mesenchymal Stem Cells Extend

the Lifespan and Enhance Liver Function in Hepatocyte Organoids. *Int J Mol Sci*, *24*(20). https://doi.org/10.3390/ijms242015429

Oh, P., McIntosh, D. P., & Schnitzer, J. E. (1998). Dynamin at the neck of caveolae mediates their budding to form transport vesicles by GTP-driven fission from the plasma membrane of endothelium. *J Cell Biol*, *141*(1), 101-114. https://doi.org/10.1083/jcb.141.1.101

Omelchenko, A., Shrirao, A. B., Bhattiprolu, A. K., Zahn, J. D., Schloss, R. S., Dickson, S., Meaney, D. F., Boustany, N. N., Yarmush, M. L., & Firestein, B. L. (2019). Dynamin and reverse-mode sodium calcium exchanger blockade confers neuroprotection from diffuse axonal injury. *Cell Death Dis*, *10*(10), 727. https://doi.org/10.1038/s41419-019-1908-3

Oprea, L., Desjardins, N., Jiang, X., Sareen, K., Zheng, J. Q., & Khadra, A. (2022). Characterizing spontaneous Ca(2+) local transients in OPCs using computational modeling. *Biophys J*, *121*(23), 4419-4432. https://doi.org/10.1016/j.bpj.2022.11.007

Palam, L. R., Ramdas, B., Pickerell, K., Pasupuleti, S. K., Kanumuri, R., Cesarano, A., Szymanski, M., Selman, B., Dave, U. P., Sandusky, G., Perna, F., Paczesny, S., & Kapur, R. (2023). Loss of Dnmt3a impairs hematopoietic homeostasis and myeloid cell skewing via the PI3Kinase pathway. *JCI Insight*, *8*(9). https://doi.org/10.1172/jci.insight.163864

Pannek, A., Becker-Gotot, J., Dower, S. K., Verhagen, A. M., & Gleeson, P. A. (2023). The endosomal system of primary human vascular endothelial cells and albumin-FcRn trafficking. *J Cell Sci*, *136*(15). https://doi.org/10.1242/jcs.260912

Park, N., Kim, K. S., & Na, K. (2023). Stem cell-derived paracrine factors by modulated reactive oxygen species to enhance cancer immunotherapy. *J Control Release*, *363*, 670-681. https://doi.org/10.1016/j.jconrel.2023.10.011

Patel, D., Haag, S. L., Patel, J. S., Ytreberg, F. M., & Bernards, M. T. (2022). Paired Simulations and Experimental Investigations into the Calcium-Dependent Conformation of Albumin. *J Chem Inf Model*, *62*(5), 1282-1293. https://doi.org/10.1021/acs.jcim.1c01104

Pestel, J., Robert, M., Corbin, S., Vidal, H., & Eljaafari, A. (2020). Involvement of glycated albumin in adipose-derived-stem cell-mediated interleukin 17 secreting T helper cell activation. *World J Stem Cells*, *12*(7), 621-632. https://doi.org/10.4252/wjsc.v12.i7.621

Peter, H. H., Ochs, H. D., Cunningham-Rundles, C., Vinh, D. C., Kiessling, P., Greve, B., & Jolles, S. (2020). Targeting FcRn for immunomodulation: Benefits, risks, and practical considerations. *J Allergy Clin Immunol*, *146*(3), 479-491 e475. https://doi.org/10.1016/j.jaci.2020.07.016

Petitpas, I., Bhattacharya, A. A., Twine, S., East, M., & Curry, S. (2001). Crystal structure analysis of warfarin binding to human serum albumin: anatomy of drug site I. *J Biol Chem*, *276*(25), 22804-22809. https://doi.org/10.1074/jbc.M100575200

Piao, L., Fang, Y. H., Fisher, M., Hamanaka, R. B., Ousta, A., Wu, R., Mutlu, G. M., Garcia, A. J., 3rd, Archer, S. L., & Sharp, W. W. (2024). Dynamin-related protein 1 is a critical regulator of mitochondrial calcium homeostasis during myocardial ischemia/reperfusion injury. *FASEB J*, *38*(1), e23379. https://doi.org/10.1096/fj.202301040RR

Plangger, A., Haslik, W., Rath, B., Neumayer, C., & Hamilton, G. (2021). Interactions of BRCA1-mutated Breast Cancer Cell Lines with Adipose-derived Stromal Cells (ADSCs). *J Mammary Gland Biol Neoplasia*, *26*(3), 235-245. https://doi.org/10.1007/s10911-021-09493-4

Poswiata, A., Kozik, K., Miaczynska, M., & Zdzalik-Bielecka, D. (2022). Endocytic trafficking of GAS6-AXL complexes is associated with sustained AKT activation. *Cell Mol Life*

Sci, *79*(6), 316. https://doi.org/10.1007/s00018-022-04312-3

Prakash, Y. S., Thompson, M. A., Vaa, B., Matabdin, I., Peterson, T. E., He, T., & Pabelick, C. M. (2007). Caveolins and intracellular calcium regulation in human airway smooth muscle. *Am J Physiol Lung Cell Mol Physiol*, *293*(5), L1118-1126. https://doi.org/10.1152/ajplung.00136.2007

Pyzik, M., Kozicky, L. K., Gandhi, A. K., & Blumberg, R. S. (2023). The therapeutic age of the neonatal Fc receptor. *Nat Rev Immunol*, *23*(7), 415-432. https://doi.org/10.1038/s41577-022-00821-1

Pyzik, M., Rath, T., Kuo, T. T., Win, S., Baker, K., Hubbard, J. J., Grenha, R., Gandhi, A., Kramer, T. D., Mezo, A. R., Taylor, Z. S., McDonnell, K., Nienaber, V., Andersen, J. T., Mizoguchi, A., Blumberg, L., Purohit, S., Jones, S. D., Christianson, G., . . . Blumberg, R. S. (2017). Hepatic FcRn regulates albumin homeostasis and susceptibility to liver injury. *Proc Natl Acad Sci U S A*, *114*(14), E2862-E2871. https://doi.org/10.1073/pnas.1618291114

Qin, Y., Ge, G., Yang, P., Wang, L., Qiao, Y., Pan, G., Yang, H., Bai, J., Cui, W., & Geng, D. (2023). An Update on Adipose-Derived Stem Cells for Regenerative Medicine: Where Challenge Meets Opportunity. *Adv Sci (Weinh)*, *10*(20), e2207334. https://doi.org/10.1002/advs.202207334

Ramlow, L., Falcke, M., & Lindner, B. (2023). An integrate-and-fire approach to Ca(2+) signaling. Part I: Renewal model. *Biophys J*, *122*(4), 713-736. https://doi.org/10.1016/j.bpj.2023.01.007

Razzak, M. (2014). Glomerular disease: Albumin endocytosis is caveolin-mediated. *Nat Rev Nephrol*, *10*(5), 242. https://doi.org/10.1038/nrneph.2014.47

Rbaibi, Y., Long, K. R., Shipman, K. E., Ren, Q., Baty, C. J., Kashlan, O. B., & Weisz, O. A. (2023). Megalin, cubilin, and Dab2 drive endocytic flux in kidney proximal tubule cells. *Mol*

Biol Cell, *34*(7), ar74. https://doi.org/10.1091/mbc.E22-11-0510

Redelman-Sidi, G., Binyamin, A., Gaeta, I., Palm, W., Thompson, C. B., Romesser, P. B., Lowe, S. W., Bagul, M., Doench, J. G., Root, D. E., & Glickman, M. S. (2018). The Canonical Wnt Pathway Drives Macropinocytosis in Cancer. *Cancer Res*, *78*(16), 4658-4670. https://doi.org/10.1158/0008-5472.CAN-17-3199

Ren, H., Su, P., Zhao, F., Zhang, Q., Huang, X., He, C., Wu, Q., Wang, Z., Ma, J., & Wang, Z. (2024). Adipose mesenchymal stem cell-derived exosomes promote skin wound healing in diabetic mice by regulating epidermal autophagy. *Burns Trauma*, *12*, tkae001. https://doi.org/10.1093/burnst/tkae001

Ren, Q., Weyer, K., Rbaibi, Y., Long, K. R., Tan, R. J., Nielsen, R., Christensen, E. I., Baty, C. J., Kashlan, O. B., & Weisz, O. A. (2020). Distinct functions of megalin and cubilin receptors in recovery of normal and nephrotic levels of filtered albumin. *Am J Physiol Renal Physiol*, *318*(5), F1284-F1294. https://doi.org/10.1152/ajprenal.00030.2020

Rennick, J. J., Johnston, A. P. R., & Parton, R. G. (2021). Key principles and methods for studying the endocytosis of biological and nanoparticle therapeutics. *Nat Nanotechnol*, *16*(3), 266-276. https://doi.org/10.1038/s41565-021-00858-8

Rosado, J. A. (2016). Calcium Entry Pathways in Non-excitable Cells. Preface. *Adv Exp Med Biol*, *898*, vii-viii. https://www.ncbi.nlm.nih.gov/pubmed/27540620

Safaralizade, M., Fuderer, R., Grosse, R., & Zhao, B. (2021). Measuring nuclear calcium and actin assembly in living cells. *J Biochem*, *169*(3), 287-294. https://doi.org/10.1093/jb/mvab002

Sakai, Y., Fukunishi, S., Takamura, M., Kawaguchi, K., Inoue, O., Usui, S., Takashima, S., Seki, A., Asai, A., Tsuchimoto, Y.,

Nasti, A., Bich Ho, T. T., Imai, Y., Yoshimura, K., Murayama, T., Yamashita, T., Arai, K., Yamashita, T., Mizukoshi, E., . . . Kaneko, S. (2021). Clinical trial of autologous adipose tissue-derived regenerative (stem) cells therapy for exploration of its safety and efficacy. *Regen Ther*, *18*, 97-101. https://doi.org/10.1016/j.reth.2021.04.003

Sand, K. M., Bern, M., Nilsen, J., Noordzij, H. T., Sandlie, I., & Andersen, J. T. (2014). Unraveling the Interaction between FcRn and Albumin: Opportunities for Design of Albumin-Based Therapeutics. *Front Immunol*, *5*, 682. https://doi.org/10.3389/fimmu.2014.00682

Sataric, M. V., Nemes, T., & Zdravkovic, S. (2023). Calcium messages in flagella are faster than messenger particles. *Biosystems*, *232*, 105003. https://doi.org/10.1016/j.biosystems.2023.105003

Sathish, V., Abcejo, A. J., Thompson, M. A., Sieck, G. C., Prakash, Y. S., & Pabelick, C. M. (2012). Caveolin-1 regulation of store-operated Ca(2+) influx in human airway smooth muscle. *Eur Respir J*, *40*(2), 470-478. https://doi.org/10.1183/09031936.00090511

Sauer, H., Hofmann, C., Wartenberg, M., Wobus, A. M., & Hescheler, J. (1998). Spontaneous calcium oscillations in embryonic stem cell-derived primitive endodermal cells. *Exp Cell Res*, *238*(1), 13-22. https://doi.org/10.1006/excr.1997.3809

Shao, X., Hu, Z., Zhan, Y., Ma, W., Quan, L., & Lin, Y. (2022). MiR-26a-tetrahedral framework nucleic acids mediated osteogenesis of adipose-derived mesenchymal stem cells. *Cell Prolif*, *55*(7), e13272. https://doi.org/10.1111/cpr.13272

Shaw, T. M., Huey, D., Mousa-Makky, M., Compaleo, J., Nennig, K., Shah, A. P., Jiang, F., Qiu, X., Klipsic, D., Rowland, R. R. R., Slukvin, II, Sullender, M. E., Baldridge, M. T., Li, H., Warren, C. J., & Bailey, A. L. (2024). The neonatal Fc

receptor (FcRn) is a pan-arterivirus receptor. *Nat Commun*, *15*(1), 6726. https://doi.org/10.1038/s41467-024-51142-x

Shen, K., Wang, X., Wang, Y., Jia, Y., Zhang, Y., Wang, K., Luo, L., Cai, W., Li, J., Li, S., Du, Y., Zhang, L., Zhang, H., Chen, Y., Xu, C., Zhang, J., Wang, R., Yang, X., Wang, Y., & Hu, D. (2023). miR-125b-5p in adipose derived stem cells exosome alleviates pulmonary microvascular endothelial cells ferroptosis via Keap1/Nrf2/GPX4 in sepsis lung injury. *Redox Biol*, *62*, 102655. https://doi.org/10.1016/j.redox.2023.102655

Silva-Aguiar, R. P., Peruchetti, D. B., Florentino, L. S., Takiya, C. M., Marzolo, M. P., Dias, W. B., Pinheiro, A. A. S., & Caruso-Neves, C. (2022). Albumin Expands Albumin Reabsorption Capacity in Proximal Tubule Epithelial Cells through a Positive Feedback Loop between AKT and Megalin. *Int J Mol Sci*, *23*(2). https://doi.org/10.3390/ijms23020848

Singh, A., Hildebrand, M. E., Garcia, E., & Snutch, T. P. (2010). The transient receptor potential channel antagonist SKF96365 is a potent blocker of low-voltage-activated T-type calcium channels. *Br J Pharmacol*, *160*(6), 1464-1475. https://doi.org/10.1111/j.1476-5381.2010.00786.x

Skupin, A., Kettenmann, H., Winkler, U., Wartenberg, M., Sauer, H., Tovey, S. C., Taylor, C. W., & Falcke, M. (2008). How does intracellular Ca2+ oscillate: by chance or by the clock? *Biophys J*, *94*(6), 2404-2411. https://doi.org/10.1529/biophysj.107.119495

Sochacki, K. A., Heine, B. L., Haber, G. J., Jimah, J. R., Prasai, B., Alfonzo-Mendez, M. A., Roberts, A. D., Somasundaram, A., Hinshaw, J. E., & Taraska, J. W. (2021). The structure and spontaneous curvature of clathrin lattices at the plasma membrane. *Dev Cell*, *56*(8), 1131-1146 e1133. https://doi.org/10.1016/j.devcel.2021.03.017

Song, S., Zhang, Y., Ding, T., Ji, N., & Zhao, H. (2020). The Dual Role of Macropinocytosis in Cancers: Promoting Growth and Inducing Methuosis to Participate in Anticancer Therapies as Targets. *Front Oncol*, *10*, 570108. https://doi.org/10.3389/fonc.2020.570108

Sotodosos-Alonso, L., Pulgarin-Alfaro, M., & Del Pozo, M. A. (2023). Caveolae Mechanotransduction at the Interface between Cytoskeleton and Extracellular Matrix. *Cells*, *12*(6). https://doi.org/10.3390/cells12060942

Sun, D., Mou, S., Chen, L., Yang, J., Wang, R., Zhong, A., Wang, W., Tong, J., Wang, Z., & Sun, J. (2022). High yield engineered nanovesicles from ADSC with enriched miR-21-5p promote angiogenesis in adipose tissue regeneration. *Biomater Res*, *26*(1), 83. https://doi.org/10.1186/s40824-022-00325-y

Sun, H., Takebayashi, Y. U., Motohashi, H., & Nagai, J. (2022). Internalization of FITC-albumin in Human Adipose-derived Stem Cells: Involvement of Clathrin and Caveolin. *Pharmazie*, *77*(5), 141-146. https://doi.org/10.1691/ph.2022.2340

Sun, S. W., Zu, X. Y., Tuo, Q. H., Chen, L. X., Lei, X. Y., Li, K., Tang, C. K., & Liao, D. F. (2010). Caveolae and caveolin-1 mediate endocytosis and transcytosis of oxidized low density lipoprotein in endothelial cells. *Acta Pharmacol Sin*, *31*(10), 1336-1342. https://doi.org/10.1038/aps.2010.87

Sutton, M. N., Gammon, S. T., Muzzioli, R., Pisaneschi, F., Radaram, B., Yang, P., & Piwnica-Worms, D. (2022). RAS-Driven Macropinocytosis of Albumin or Dextran Reveals Mutation-Specific Target Engagement of RAS p.G12C Inhibitor ARS-1620 by NIR-Fluorescence Imaging. *Mol Imaging Biol*, *24*(3), 498-509. https://doi.org/10.1007/s11307-021-01689-8

Suzuki, H., Yokoi, A., Uno, K., Yoshida, K., Kitagawa, M., Asano-Inami, E., Matsuo, S., Nagao, Y., Suzuki, K., Nakamura, K.,

Yoshihara, M., Tamauchi, S., Shimizu, Y., Ikeda, Y., Yoshikawa, N., Kajiyama, H., & Yamamoto, Y. (2023). Small Extracellular Vesicles from adipose-derived stem cells suppress cell proliferation by delivering the let-7 family of microRNAs in ovarian cancer. *Biochem Biophys Res Commun*, *680*, 211-219. https://doi.org/10.1016/j.bbrc.2023.09.022

Synowiec, A., Dabrowska, A., Pachota, M., Baouche, M., Owczarek, K., Nizanski, W., & Pyrc, K. (2023). Feline herpesvirus 1 (FHV-1) enters the cell by receptor-mediated endocytosis. *J Virol*, *97*(8), e0068123. https://doi.org/10.1128/jvi.00681-23

Tagiltsev, G., Haselwandter, C. A., & Scheuring, S. (2021). Nanodissected elastically loaded clathrin lattices relax to increased curvature. *Sci Adv*, *7*(33). https://doi.org/10.1126/sciadv.abg9934

Tapon, N., & Hall, A. (1997). Rho, Rac and Cdc42 GTPases regulate the organization of the actin cytoskeleton. *Curr Opin Cell Biol*, *9*(1), 86-92. https://doi.org/10.1016/s0955-0674(97)80156-1

Tincu Iurciuc, C. E., Andritoiu, C. V., Popa, M., & Ochiuz, L. (2023). Recent Advancements and Strategies for Overcoming the Blood-Brain Barrier Using Albumin-Based Drug Delivery Systems to Treat Brain Cancer, with a Focus on Glioblastoma. *Polymers (Basel)*, *15*(19). https://doi.org/10.3390/polym15193969

Tobys, D., Kowalski, L. M., Cziudaj, E., Muller, S., Zentis, P., Pach, E., Zigrino, P., Blaeske, T., & Honing, S. (2021). Inhibition of clathrin-mediated endocytosis by knockdown of AP-2 leads to alterations in the plasma membrane proteome. *Traffic*, *22*(1-2), 6-22. https://doi.org/10.1111/tra.12770

Toh, W. H., Louber, J., Mahmoud, I. S., Chia, J., Bass, G. T., Dower, S. K., Verhagen, A. M., & Gleeson, P. A. (2019). FcRn mediates fast recycling of endocytosed albumin and IgG

from early macropinosomes in primary macrophages. *J Cell Sci*, *133*(5). https://doi.org/10.1242/jcs.235416

Torre, E. C., Bicer, M., Cottrell, G. S., Widera, D., & Tamagnini, F. (2021). Time-Dependent Reduction of Calcium Oscillations in Adipose-Derived Stem Cells Differentiating towards Adipogenic and Osteogenic Lineage. *Biomolecules*, *11*(10). https://doi.org/10.3390/biom11101400

Trzyna, A., & Banas-Zabczyk, A. (2021). Adipose-Derived Stem Cells Secretome and Its Potential Application in "Stem Cell-Free Therapy". *Biomolecules*, *11*(6). https://doi.org/10.3390/biom11060878

Ulferts, S., & Grosse, R. (2024). SUN2 mediates calcium-triggered nuclear actin polymerization to cluster active RNA polymerase II. *EMBO Rep*, *25*(11), 4728-4748. https://doi.org/10.1038/s44319-024-00274-8

Venianakis, T., Primikyri, A., Opatz, T., Petry, S., Papamokos, G., & Gerothanassis, I. P. (2023). NMR and Docking Calculations Reveal Novel Atomistic Selectivity of a Synthetic High-Affinity Free Fatty Acid vs. Free Fatty Acids in Sudlow's Drug Binding Sites in Human Serum Albumin. *Molecules*, *28*(24). https://doi.org/10.3390/molecules28247991

Vera, R., Sanchez, M., Galisteo, M., Villar, I. C., Jimenez, R., Zarzuelo, A., Perez-Vizcaino, F., & Duarte, J. (2007). Chronic administration of genistein improves endothelial dysfunction in spontaneously hypertensive rats: involvement of eNOS, caveolin and calmodulin expression and NADPH oxidase activity. *Clin Sci (Lond)*, *112*(3), 183-191. https://doi.org/10.1042/CS20060185

Vercauteren, D., Vandenbroucke, R. E., Jones, A. T., Rejman, J., Demeester, J., De Smedt, S. C., Sanders, N. N., & Braeckmans, K. (2010). The use of inhibitors to study endocytic pathways of gene carriers: optimization and

pitfalls. *Mol Ther*, *18*(3), 561-569. https://doi.org/10.1038/mt.2009.281

Wang, B., Yao, X., Dong, Q., Wang, X. F., Yin, H., Li, Q., Wang, X. Q., Liu, Y., Pan, Y. W., & Yuan, G. Q. (2023). Quantitation of macropinocytosis in glioblastoma based on high-content analysis. *J Neurosci Methods*, *397*, 109947. https://doi.org/10.1016/j.jneumeth.2023.109947

Wang, J., Xu, C., Zheng, Q., Yang, K., Lai, N., Wang, T., Tang, H., & Lu, W. (2017). Orai1, 2, 3 and STIM1 promote store-operated calcium entry in pulmonary arterial smooth muscle cells. *Cell Death Discov*, *3*, 17074. https://doi.org/10.1038/cddiscovery.2017.74

Wang, Y. Y., Hung, A. C., Wu, Y. C., Lo, S., Chen, H. D., Chen, Y. K., Hsieh, Y. C., Hu, S. C., Hou, M. F., & Yuan, S. F. (2022). ADSCs stimulated by resistin promote breast cancer cell malignancy via CXCL5 in a breast cancer coculture model. *Sci Rep*, *12*(1), 15437. https://doi.org/10.1038/s41598-022-19290-6

Wen, C., Hu, H., Yang, W., Zhao, Y., Zheng, L., Jiang, X., & Wang, L. (2022). Targeted inhibition of FcRn reduces NET formation to ameliorate experimental ulcerative colitis by accelerating ANCA clearance. *Int Immunopharmacol*, *113*(Pt B), 109474. https://doi.org/10.1016/j.intimp.2022.109474

Wu, L., Zhang, X., Yi, C., & Ren, H. (2023). CD146-positive adipose-derived stem cells subpopulation enriched by albumin magnetic sphere ameliorates knee osteoarthritis pain and promotes cartilage repair. *J Orthop Surg Res*, *18*(1), 969. https://doi.org/10.1186/s13018-023-04434-9

Wu, L. G., Hamid, E., Shin, W., & Chiang, H. C. (2014). Exocytosis and endocytosis: modes, functions, and coupling mechanisms. *Annu Rev Physiol*, *76*, 301-331. https://doi.org/10.1146/annurev-physiol-021113-170305

Wu, S., Chen, Z., Wu, Y., Shi, Q., Yang, E., Zhang, B., Qian, Y., Lian, X., & Xu, J. (2024). ADSC-Exos enhance functional recovery after spinal cord injury by inhibiting ferroptosis and promoting the survival and function of endothelial cells through the NRF2/SLC7A11/GPX4 pathway. *Biomed Pharmacother*, *172*, 116225. https://doi.org/10.1016/j.biopha.2024.116225

Wu, S. C., Kuo, P. J., Rau, C. S., Huang, L. H., Lin, C. W., Wu, Y. C., Wu, C. J., Tsai, C. W., Hsieh, T. M., Liu, H. T., Huang, C. Y., & Hsieh, C. H. (2021). Increased Angiogenesis by Exosomes Secreted by Adipose-Derived Stem Cells upon Lipopolysaccharide Stimulation. *Int J Mol Sci*, *22*(16). https://doi.org/10.3390/ijms22168877

Wu, Y., Hu, X., Wei, Z., & Lin, Q. (2024). Cellular Regulation of Macropinocytosis. *Int J Mol Sci*, *25*(13). https://doi.org/10.3390/ijms25136963

Wyckoff, S. L., & Hudson, K. E. (2021). Targeting the neonatal Fc receptor (FcRn) to treat autoimmune diseases and maternal-fetal immune cytopenias. *Transfusion*, *61*(5), 1350-1354. https://doi.org/10.1111/trf.16341

Xiao, X. H., Huang, Q. Y., Qian, X. L., Duan, J., Jiao, X. Q., Wu, L. Y., Huang, Q. Y., Li, J., Lai, X. N., Shi, Y. B., & Xiong, L. X. (2019). Cdc42 Promotes ADSC-Derived IPC Induction, Proliferation, And Insulin Secretion Via Wnt/beta-Catenin Signaling. *Diabetes Metab Syndr Obes*, *12*, 2325-2339. https://doi.org/10.2147/DMSO.S226055

Xu, J., Chen, X., Wang, J., Zhang, B., Ge, W., Wang, J., Yang, P., & Liu, Y. (2024). An ADSC-loaded dermal regeneration template promotes full-thickness wound healing. *Regen Ther*, *26*, 800-810. https://doi.org/10.1016/j.reth.2024.08.010

Xue, C., Li, X., Ba, L., Shen, Y., Sun, Z., Gu, J., Yang, Y., Han, Q., & Zhao, R. C. (2022). Irisin mediates beiging of adipose-derived mesenchymal stem cells through binding to

TRPC3. *BMC Biol*, *20*(1), 95. https://doi.org/10.1186/s12915-022-01287-2

Yamana, H., Inagaki, A., Imura, T., Nakamura, Y., Nishimaki, H., Katano, T., Ohashi, K., Miyagi, S., Kamei, T., Unno, M., & Goto, M. (2022). Cotransplantation With Adipose Tissue-derived Stem Cells Improves Engraftment of Transplanted Hepatocytes. *Transplantation*, *106*(10), 1963-1973. https://doi.org/10.1097/TP.0000000000004130

Yanai, R., Tetsuo, F., Ito, S., Itsumi, M., Yoshizumi, J., Maki, T., Mori, Y., Kubota, Y., & Kajioka, S. (2019). Extracellular calcium stimulates osteogenic differentiation of human adipose-derived stem cells by enhancing bone morphogenetic protein-2 expression. *Cell Calcium*, *83*, 102058. https://doi.org/10.1016/j.ceca.2019.102058

Yang, C., Colosi, P., Hugelier, S., Zabezhinsky, D., Lakadamyali, M., & Svitkina, T. (2022). Actin polymerization promotes invagination of flat clathrin-coated lattices in mammalian cells by pushing at lattice edges. *Nat Commun*, *13*(1), 6127. https://doi.org/10.1038/s41467-022-33852-2

Yang, C., Rybchyn, M. S., De Silva, W. G. M., Matthews, J., Dixon, K. M., Holland, A. J. A., Conigrave, A. D., & Mason, R. S. (2023). The CaSR Modulator NPS-2143 Reduced UV-Induced DNA Damage in Skh:hr1 Hairless Mice but Minimally Inhibited Skin Tumours. *Int J Mol Sci*, *24*(5). https://doi.org/10.3390/ijms24054921

Yang, C., Zhang, H., Zeng, C., Tian, C., Liu, W., Chen, Y., Jia, M., Wang, R., Wang, K., & Li, Y. (2024). Exosomes from adipose-derived stem cells restore fibroblast function and accelerate diabetic wound healing. *Heliyon*, *10*(1), e22802. https://doi.org/10.1016/j.heliyon.2023.e22802

Yang, M., Zhao, Q., Zhao, H., Yang, A., Wang, F., Wang, X., Tang, Y., & Huang, C. (2019). Adipose-derived stem cells overexpressing SK4 calcium-activated potassium channel

generate biological pacemakers. *Int J Mol Med*, *44*(6), 2103-2112. https://doi.org/10.3892/ijmm.2019.4374

Yang, S., Min, C., Moon, H., Moon, B., Lee, J., Jeon, J., Kwon, H., Jang, D., & Park, D. (2023). Internalization of apoptotic cells during efferocytosis requires Mertk-mediated calcium influx. *Cell Death Dis*, *14*(6), 391. https://doi.org/10.1038/s41419-023-05925-7

Yang, Y., Li, X., Song, J., Li, L., Ye, Q., Zuo, S., Liu, T., Dong, F., Liu, X., He, Z., Sun, B., & Sun, J. (2023). Structure-Activity Relationship of pH-Sensitive Doxorubicin-Fatty Acid Prodrug Albumin Nanoparticles. *Nano Lett*, *23*(4), 1530-1538. https://doi.org/10.1021/acs.nanolett.2c04976

Yano, F., Takeda, T., Kurokawa, T., Tsubaki, T., Chijimatsu, R., Inoue, K., Tsuji, S., Tanaka, S., & Saito, T. (2022). Effects of conditioned medium obtained from human adipose-derived stem cells on skin inflammation. *Regen Ther*, *20*, 72-77. https://doi.org/10.1016/j.reth.2022.03.009

Yao, D., Ehrlich, M., Henis, Y. I., & Leof, E. B. (2002). Transforming growth factor-beta receptors interact with AP2 by direct binding to beta2 subunit. *Mol Biol Cell*, *13*(11), 4001-4012. https://doi.org/10.1091/mbc.02-07-0104

Yogi, A., Rukhlova, M., Charlebois, C., Tian, G., Stanimirovic, D. B., & Moreno, M. J. (2021). Differentiation of Adipose-Derived Stem Cells into Vascular Smooth Muscle Cells for Tissue Engineering Applications. *Biomedicines*, *9*(7). https://doi.org/10.3390/biomedicines9070797

Yu, L., Xue, J., Wu, Y., & Zhou, H. (2023). Therapeutic effect of exosomes derived from hepatocyte-growth-factor-overexpressing adipose mesenchymal stem cells on liver injury. *Folia Histochem Cytobiol*, *61*(3), 160-171. https://doi.org/10.5603/fhc.95291

Zdzalik-Bielecka, D., Poswiata, A., Kozik, K., Jastrzebski, K., Schink, K. O., Brewinska-Olchowik, M., Piwocka, K., Stenmark, H., & Miaczynska, M. (2021). The GAS6-AXL signaling pathway triggers actin remodeling that drives membrane

ruffling, macropinocytosis, and cancer-cell invasion. *Proc Natl Acad Sci U S A*, *118*(28). https://doi.org/10.1073/pnas.2024596118

Zeng, B., Chen, G. L., Garcia-Vaz, E., Bhandari, S., Daskoulidou, N., Berglund, L. M., Jiang, H., Hallett, T., Zhou, L. P., Huang, L., Xu, Z. H., Nair, V., Nelson, R. G., Ju, W., Kretzler, M., Atkin, S. L., Gomez, M. F., & Xu, S. Z. (2017). ORAI channels are critical for receptor-mediated endocytosis of albumin. *Nat Commun*, *8*(1), 1920. https://doi.org/10.1038/s41467-017-02094-y

Zhai, P., Lv, W., Yang, X., Huang, Y., Zhai, W., Ren, X., Zhang, X., Yang, M., Zhang, J., Guo, T., Bai, M., Yang, Y., Ding, Y., & Huang, Y. (2022). Renal Expression of CLC-5 and Megalin/Cubilin in Dent-1 Disease With Nonsense Mutations of CLCN5 Gene. *Pediatr Dev Pathol*, *25*(4), 397-403. https://doi.org/10.1177/10935266211065554

Zhan, Y., Zhang, L., Sun, J., Yao, H., Chen, J., & Tian, M. (2024). ADSC-derived exosomes provide neuroprotection in sepsis-associated encephalopathy by regulating hippocampal pyroptosis. *Exp Neurol*, *380*, 114900. https://doi.org/10.1016/j.expneurol.2024.114900

Zhang, J., Li, J., Qu, X., Liu, Y., Sun, L., Harada, A., Hua, Y., Sougawa, N., Tabata, A., Liu, L., & Miyagawa, S. (2024). Development of composite functional tissue sheets using hiPSC-CMs and hADSCs to improve the cardiac function after myocardial infarction. *Bioact Mater*, *37*, 533-548. https://doi.org/10.1016/j.bioactmat.2024.03.028

Zhang, L., Toboso-Navasa, A., Gunawan, A., Camara, A., Nakagawa, R., Finsterbusch, K., Chakravarty, P., Newman, R., Zhang, Y., Eilers, M., Wack, A., Tolar, P., Toellner, K. M., & Calado, D. P. (2024). Regulation of BCR-mediated Ca(2+) mobilization by MIZ1-TMBIM4 safeguards IgG1(+) GC B cell-positive selection. *Sci Immunol*, *9*(94), eadk0092. https://doi.org/10.1126/sciimmunol.adk0092

Zhang, L., Zhang, B., Liao, B., Yuan, S., Liu, Y., Liao, Z., & Cheng, B. (2019). Platelet-rich plasma in combination with adipose-derived stem cells promotes skin wound healing through activating Rho GTPase-mediated signaling pathway. *Am J Transl Res*, *11*(7), 4100-4112. https://www.ncbi.nlm.nih.gov/pubmed/31396321

Zhang, X., Zhang, T., Wu, J., Yu, X., Zheng, D., Yang, F., Li, T., Wang, L., Zhao, Y., Dong, S., Zhong, X., Fu, S., Xu, C. Q., Lu, F., & Zhang, W. H. (2014). Calcium sensing receptor promotes cardiac fibroblast proliferation and extracellular matrix secretion. *Cell Physiol Biochem*, *33*(3), 557-568. https://doi.org/10.1159/000358634

Zheng, Z. K., Kong, L., Dai, M., Chen, Y. D., & Chen, Y. H. (2023). ADSC-Exos outperform BMSC-Exos in alleviating hydrostatic pressure-induced injury to retinal ganglion cells by upregulating nerve growth factors. *World J Stem Cells*, *15*(12), 1077-1092. https://doi.org/10.4252/wjsc.v15.i12.1077

Zhou, C., Zhang, B., Yang, Y., Jiang, Q., Li, T., Gong, J., Tang, H., & Zhang, Q. (2023). Stem cell-derived exosomes: emerging therapeutic opportunities for wound healing. *Stem Cell Res Ther*, *14*(1), 107. https://doi.org/10.1186/s13287-023-03345-0

Zhou, Y., Zhang, X. L., Lu, S. T., Zhang, N. Y., Zhang, H. J., Zhang, J., & Zhang, J. (2022). Human adipose-derived mesenchymal stem cells-derived exosomes encapsulated in pluronic F127 hydrogel promote wound healing and regeneration. *Stem Cell Res Ther*, *13*(1), 407. https://doi.org/10.1186/s13287-022-02980-3

Zhu, C., Teng, L., Lai, Y., Yao, X., Fang, Y., Wang, Z., Lin, S., Zhang, H., Li, Q., Li, Y., Cai, J., Zhang, Y., Wu, C., Huang, B., Li, A., Liu, S., & Lai, Q. (2024). Adipose-derived stem cells promote glycolysis and peritoneal metastasis via TGF-beta1/SMAD3/ANGPTL4 axis in colorectal cancer. *Cell*

Mol Life Sci, *81*(1), 189. https://doi.org/10.1007/s00018-024-05215-1

Zhu, D., Johnson, T. K., Wang, Y., Thomas, M., Huynh, K., Yang, Q., Bond, V. C., Chen, Y. E., & Liu, D. (2020). Macrophage M2 polarization induced by exosomes from adipose-derived stem cells contributes to the exosomal proangiogenic effect on mouse ischemic hindlimb. *Stem Cell Res Ther*, *11*(1), 162. https://doi.org/10.1186/s13287-020-01669-9

Zivanovic, J., Jaric, I., Ajdzanovic, V., Miler, M., Stankovic, S., Milosevic, V., & Filipovic, B. (2022). Genistein regulates calcium and phosphate homeostasis without activation of MEK 1/2 signalling pathway in an animal model of the andropause. *Ann Anat*, *239*, 151836. https://doi.org/10.1016/j.aanat.2021.151836

Zuk, P. A., Zhu, M., Mizuno, H., Huang, J., Futrell, J. W., Katz, A. J., Benhaim, P., Lorenz, H. P., & Hedrick, M. H. (2001). Multilineage cells from human adipose tissue: implications for cell-based therapies. *Tissue Eng*, *7*(2), 211-228. https://doi.org/10.1089/107632701300062859

9. Appendix

9.1 List of Tables

9.2 List of Figures

9.3 List of Symbols

Symbol	Intended Meaning
° C	Degree Celsius
%	percentage
<	Greater than
>	Lower than
*p	Statistical significance level with p value <0.05
**p	Statistical significance level with p value <0.01
⁂p	Statistical significance level with p value <0.001
Σ	Summation

9.4 List of Abbreviations

Abbreviation	Elaboration
ADSCs	Adipose tissue derived stem cells
Akt	Serine-threonine protein kinase
a.k.a.	Also Known As
AMN	Amnionless
Ang-2	Angiopoietin 2
AP	Adaptor protein
ARS	Alizarin Red S
ASGPR	Asialoglycoprotein receptor
AXL	Anexelekto (meaning uncontrolled)
β-GP	Glycerol-2-phosphate disodium salt hydrate
β2m	β2-microglobulin
BRCA1	Breast cancer type 1 susceptibility protein

Abbreviation	Elaboration
BSA	Bovine Serum Albumin
BMP-2	Bone Morphogenetic Protein-2
Ca^{2+}	Calcium ion
CAF	Cancer-associated Fibroblast
CaM	Calmodulin
CaMKII	Ca^{2+} /calmodulin-dependent protein kinase II
CaMKIV	Ca^{2+} /calmodulin-dependent protein kinase IV
Cat	Catalog number
Cav	Caveolin
Cavin	Caveola-associated protein
CaSR	Ca^{2+} sensing receptor
CCVs	Clathrin coated vesicles
CCM	Complete culture medium
CD	Cytochalasin D
Cdc 42	Cell division control protein 42 homolog
CDE	Caveolae-dependent endocytosis
CDM	Complete differentiation medium
CDK1	Cyclin-dependent kinase 1
CME	Clathrin-mediated endocytosis
CLCN5	Chloride voltage-gated channel 5
C-LSM	Confocal laser scanning microscopy
CPZ	Chlorpromazine
CREB	cAMP-response element binding protein
CXCL5	C-X-C motif chemokine 5
dH_2O	Distilled water
ddH_2O	Double distilled water
Dab1, -2	Disabled homolog 1, -2
DMSO	Dimethyl sulfoxide
Drp1	Dynamin-related protein 1
Dyn	Dynamin

Abbreviation	Elaboration
Dyn-I, -II, -III	Dynamin-I, -II, -III
ECL	Electrochemiluminocence
ECM	Extracellular Matrix
EIPA	5-N-ethyl-N-isopropyl-amiloride
ERK	Extracellular signal-regulated kinases
EtOH	Ethyl alcohol
EVs	Extracellular Vesicles
FA	Fatty acid binding site
Fab	Antigen-binding fragment
FBS	Fetal bovine serum
Fc	Constant fragment
f.c.	final concentration
FcRn	neonatal Fc receptor
FcGRT	Fc gamma receptor and transporter (gene that code for FcRn)
FGF-2	Fibroblast growth factor-2
Fig	Figure
FITC	Fluorescein isothiocyanate
GAS6	Growth arrest-specific protein 6
Gen	Genistein
gMG	Generalised myasthenia gravis
GSK-3β	Glycogen synthase kinase-3 beta
GTP	Guanosine-5'-triphosphate
h	Hour(s)
hADSCs	Human ADSCs
hFcRn	Human FcRn
HEK	Human embryonic kidney
HGF	Hepatocyte growth factor
HR1	Homologous region 1
HSA	Human Serum Albumin
ICC	Immunocytochemistry

Abbreviation	Elaboration
ID	Identification number
IgA	Immunoglobulin A
IgE	Immunoglobulin E
IgG	Immunoglobulin G
IgM	Immunoglobulin M
IHC	Immunohistochemistry
IL-8	Interleukin-8
IL-10	Interleukin-10
IL-17	Interleukin-17
Imp	Imipramine
IR	Ischemia/reperfusion
ISI	Interspike interval
K-RAS	Protein coded by KRAS (Kirsten rat sarcoma virus) gene
LacCer	BODIPY™ FL C5-LactosylCeramide-BSA
LDL	Low-density lipoproteins
Lmx1a	LIM homeobox transcription factor 1 α
M281	Nipocalimab
µl	Microliter
µg	Microgram
µM	Micro molar
µm	Micrometre
mA	Milliampere
MetOH	Methyl alcohol, methanol
mg	Milligram
Mg^{2+}	Magnesium ion
min	Minute(s)
ml	Millilitre
mm	Millimetre
MM	Maintenance medium
MPS	Macropinosomes

Abbreviation	Elaboration
ms	Millisecond(s)
MSC	Mesenchymal stem cell
mTORC1	Mammalian target of rapamycin complex 1
n	Number of individual experiments
NAADP	Nicotinic acid adenine dinucleotide phosphate
NCX	Na^+ /Ca^{2+} exchanger
NEA	Non-essential amino acids
NF-κB	Nuclear factor 'kappa-light-chain-enhancer' of activated B-cells
NHE	Na^+/H^+ exchanger protein
nm	Nanometer
nM	Nano molar
NO	Nitric oxide
Noco	Nocodzole
NPs	Nanoparticles
NPS-2143	NPS-2143-hydrochloride
NRF2	Nuclear factor erythroid 2-related factor 2
ns	Statistically not significant with p value >0.05
Nurr1	Nuclear Receptor 4A2 (NR4A2)
NVs	Nanovesicles
Nyn	Nystatin
ORAI1	Calcium release-activated calcium channel protein 1
PAMPs	Pathogen-associated molecular patterns
PBS	Phosphate buffer saline
PFA	Paraformaldehyde
PI3k	Phosphatidylinositol 3-kinase
PM	Plasma membrane

Abbreviation	Elaboration
post-mTBI	Post-mild traumatic brain injury
PRRs	Pattern recognition receptors
p-STAT3	Phosphorylated STAT3
PT	Proximal tubule
PTEN	Phosphatase and TENsin homolog deleted on chromosome 10
Rac	Ras-related C3 botulinum toxin substrate
RBCs	Red blood cells
Rho	Rhodopsin protein
RIPA	Radioimmunoprecipitation assay
ROCE	Receptor-operated Ca^{2+} entry
ROS	Reactive oxygen species
RT	Room temperature
s	Second(s)
SCaLTs	Spontaneous Ca^{2+} local transients
Sc-RNA	scrambled si-RNA
SD	Standard deviation
SDF-1	Stromal cell-derived factor-1
Si-RNA	Small interfering RNA
SK4	Ca^{2+} activated potassium channel KCNN4
SKF-96365	SKF-96365 hydrochloride
SNAT7	Sodium-coupled amino acid transporter 7
SNX	Sorting nexins
SNX5	Sorting nexin 5
SOCE	Store operated Ca^{2+} entry
Src (c-Src)	Sarcoma (cellular sarcoma)
STAT3	Signal transducer and activator of transcription-3
STIM1	Stromal interaction molecule 1
s.c.	stock concentration

Abbreviation	Elaboration
TIMP-1	Tissue inhibitors of metalloproteinases-1
TIMP-2	Tissue inhibitors of metalloproteinases-2
Tmbim4	Transmembrane BAX Inhibitor Motif Containing 4
TPCs	Two-pore channels
V	Volt
VEGF	Vascular endothelial growth factor
WB	Western blot
Wnt	Wingless-related integration site
Won	Wortmannin

9.5 List of Publications

Part of this study have been published in peer reviewed journals and presented as posters in scientific conference.

Articles Published:

Morshed, M. T., Bernhardt, A., Wartenberg, M., & Sauer, H. (2025). Endocytotic Albumin Uptake Pathways in Human Adipose Stem Cells and Connection to Intracellular Calcium Oscillations and the Neonatal Fc receptor (FcRn). *Cells, tissues, organs*, 1–29. Advance online publication. https://doi.org/10.1159/000545773

Bernhardt, A., Jamil, A., **Morshed, M. T.**, Ponnath, P., Gille, V., Stephan, N., Sauer, H., & Wartenberg, M. (2024). Oxidative stress and regulation of adipogenic differentiation capacity by sirtuins in adipose stem cells derived from female patients of advancing age. *Scientific reports*, *14*(1), 19885. https://doi.org/10.1038/s41598-024-70382-x

Poster Presentations:

Anne Bernhardt, Alan Jamil, **Md Tanvir Morshed**, Maria Wartenberg and Heinrich Sauer. Patient age-related changes of redox parameters in subdermal adipose-derived stem cells (hASCs). 102nd Annual Meeting of German Physiological Society, 21 – 23 Sept. 2023, Freie Univrsity Berlin, Germany.

Md Tanvir Morshed, Anne Bernhardt, Maria Wartenberg and Heinrich Sauer. Calcium oscillations regulate endocytotic albumin uptake in subdermal adipose stem cells derived from human patients of different age. 102nd Annual Meeting of German Physiological Society, 21 – 23 Sept. 2023, Freie Univrsity Berlin, Germany.

9.6 Declaration

I hereby affirm that I have independently completed this dissertation without any unauthorized assistance from third parties. Any assistance received is acknowledged within the text. I have properly cited and referenced all text passages that are either directly quoted or derived from the published or unpublished works of others, as well as all information based on verbal communication. In conducting the research and investigations described in this dissertation, I adhered to the ethical principles of scientific conduct outlined in the charter of Justus Liebig University of Giessen.

Md Tanvir Morshed

9.7 Ehrenwörtliche Erklärung:

„Hiermit erkläre ich, dass ich die vorliegende Arbeit selbständig und ohne unzulässige Hilfe oder Benutzung anderer als der angegebenen Hilfsmittel angefertigt habe. Alle Textstellen, die wörtlich oder sinngemäß aus veröffentlichten oder nichtveröffentlichten Schriften entnommen sind, und alle Angaben, die auf mündlichen Auskünften beruhen, sind als solche kenntlich gemacht. Bei den von mir durchgeführten und in der Dissertation erwähnten Untersuchungen habe ich die Grundsätze guter wissenschaftlicher Praxis, wie sie in der „Satzung der Justus-Liebig-Universität Gießen zur Sicherung guter wissenschaftlicher Praxis“ niedergelegt sind, eingehalten sowie ethische, datenschutzrechtliche und tierschutzrechtliche Grundsätze befolgt. Ich versichere, dass Dritte von mir weder unmittelbar noch mittelbar geldwerte Leistungen für Arbeiten erhalten haben, die im Zusammenhang mit dem Inhalt der vorgelegten Dissertation stehen, und dass die vorgelegte Arbeit weder im Inland noch im Ausland in gleicher oder ähnlicher Form einer anderen Prüfungsbehörde zum Zweck einer Promotion oder eines anderen Prüfungsverfahrens vorgelegt wurde. Alles aus anderen Quellen und von anderen Personen übernommene

Material, das in der Arbeit verwendet wurde oder auf das direkt Bezug genommen wird, wurde als solches kenntlich gemacht. Insbesondere wurden alle Personen genannt, die direkt und indirekt an der Entstehung der vorliegenden Arbeit beteiligt waren. Mit der Überprüfung meiner Arbeit durch eine Plagiatserkennungssoftware bzw. ein internetbasiertes Softwareprogramm erkläre ich mich einverstanden.“

----------	----------
Ort/Datum	Unterscrift

Acknowledgements:

I wish to express my profound gratitude to Almighty **God** for granting me the strength, patience, and guidance necessary for the successful completion of this dissertation. Furthermore, I wish to commemorate the late **Prof. Dr. Mohammed Rahmatullah**, Vice Chancellor of the University of Development Alternative, who inspired me to undertake this journey.

I am sincerely thankful to the **Postgraduate Scholarship Funding Selection Committee** at the **University of Giessen** for awarding me the scholarship that facilitated the pursuit and completion of my doctoral studies. I also acknowledge the **German Research Foundation** (**DFG**) for providing the research grant funding, which was crucial for the successful completion of this study.

My heartfelt appreciation is directed towards my supervisor, **Prof. Dr. Heinrich Sauer**, for selecting me to undertake my research within his esteemed team and for his invaluable guidance in research planning, experimental design and technical suggestions. His mentorship was instrumental at every stage of this study. I also extend my gratitude to my co-supervisor, **Prof. Dr. Maria Wartenberg**, for her

constructive comments and insightful feedback on manuscript preparation. I wish to express my sincere thanks to **Prof. Dr. Rainer Schulz**, Director of the Institute of Physiology, for his support and leadership, which greatly facilitated this research.

Special thanks are due to the technical staff, **Mrs. Barbara Arnold** and **Mrs. Nadine Woitasky**, for their expert assistance in laboratory work and unwavering technical support. I am also grateful to my colleagues — **Ms. Anne Bernherdt**, **Mr. Alan Jamil**, **Mr. Leopold Stabauer**, **Ms. Jenny Scharmacher**, **Dr. Amer Taha**, and **Dr. Farhad Khosravi** — for their helpful suggestions, collegial cooperation, and stimulating discussions.

My heartfelt thanks are extended to my dear friends — **Sumi Akter Suma**, **Shahnaz Rahman**, **Zahidul Islam Khan**, **Saeed Arif Hosain**, **Mohammad Rashedul Alam**, **Mir Kamrul Alam**, **Abdullah Al Mamun**, **Hasan Dewan**, **Md. Ridowanul Hoque**, **Abrar Mozahid Siddique**, **Md Shajedur Hossain**, **Dr. Mohammad Shahadat Hossain**, and **Dr. Muhammad Shahedul Alam** — whose encouragement, motivation, and emotional support have greatly inspired me throughout this journey.

I am profoundly indebted to my parents and siblings for their unwavering love and constant moral support, which have been a source of strength during challenging times.

Finally, my deepest appreciation and love are reserved for my wife, **Nasrin Akter**, for her patience, sacrifice throughout the duration of this academic endeavor.